Direct numerical simulations of flow around non-spherical particles

Pacha Sanjeevi, Sathish Krishnan

Important note
To cite this publication, please use the final published version (if applicable).
Please check the document version above.

DIRECT NUMERICAL SIMULATIONS OF FLOW AROUND NON-SPHERICAL PARTICLES

DIRECT NUMERICAL SIMULATIONS OF FLOW AROUND NON-SPHERICAL PARTICLES

Dissertation

for the purpose of obtaining the degree of doctor
at Delft University of Technology
by the authority of the Rector Magnificus prof.dr.ir. T.H.J.J. van der Hagen
chair of the Board for Doctorates
to be defended publicly on
Tuesday 2 July 2019 at 15:00 hour

by

Sathish Krishnan PACHA SANJEEVI

Master of Science in Simulation Sciences, RWTH Aachen University, Germany,
born in Arakkonam, India.

To my father

CONTENTS

SUMMARY

Gas-solid flows are widely preferred in industries due to high gas-solids contact, resulting in excellent heat and mass transfer properties. For this reason, fluidization remains as one of the key industrial processes in chemical, energy, metallurgy, and pharmaceutical industries. Computer simulations are widely used to understand and improve such fluidization processes. However, due to current limitations in computational power, a multiscale modelling approach is used to simulate such fluidization processes. At the most fundamental level, direct numerical simulations (DNS) are used to develop hydrodynamic force correlations for larger scale simulations. Conventionally, DNS are performed for flows around assemblies of spheres. However, there exists no clear approach among the scientific community to quantify the results for real particles, which are often non-spherical. This is due to the difficulty in identifying the dependent parameters, which adequately represent the non-spherical multiparticle system.

This work, funded by the European Research Council, focuses on creating a recipe for parametrizing flow around assemblies of non-spherical particles. A multi-relaxation time lattice Boltzmann method (MRT-LBM) is used to simulate the flow. This work focuses on 3 different developments. First, different boundary conditions available in the literature for LBM are tested to identify the best for the flow problem. With the use of interpolated bounce back schemes to accurately represent the particle geometry, there is a mass leak/gain issue which is a concern for flows with periodic boundaries. To address this issue, new types of mass correction schemes are explored and suggestions are made for different flow conditions.

The second part of the thesis focuses on developing more widely applicable scaling laws for drag and lift of various isolated non-spherical particles. This is important because there are several shapes and sizes of non-spherical particles. Therefore, having simple scaling laws can save simulation time and cost. In the process, we observe that the *sine-squared* scaling of drag predicted for creeping flows is valid even in the inertial regime (high *Re*), especially for elongated particles. Likewise, the *sine-cosine* scaling of lift predicted for creeping flows is found to be a good approximation in the inertial regime, for elongated particles. The reason for such scaling in the inertial regime is found not due to the flow linearity, as is the case for creeping flow, but due to an interesting pattern of pressure distribution on particles at high *Re*. The pressure distribution contributing to the

drag and lift shows a dependency on the particle surface normal orientation with the incoming flow. Subsequently, drag, lift and torque correlations are proposed for various isolated non-spherical particles from creeping to high Reynolds number flows with $Re \leq 2000$.

In the third part, a recipe to describe hydrodynamic forces on assemblies of axisymmetric, non-spherical particles is proposed. With the described parameters, drag, lift and torque correlations are proposed accordingly. At the moment, there exists no systematic study to identify the dependent parameters for flow around assemblies of non-spherical particles. Apart from the Reynolds number Re and solids volume fraction ϵ_s, we propose four additional parameters to characterize the flow through non-spherical particle assemblies. Two parameters consider the mutual orientations of particles and two parameters represent the flow direction. Interestingly, we observe that the average results are independent of the above described four additional parameters. For a given Re and ϵ_s, we observe that the only dependent parameter representing the particle configuration itself is the incident angle ϕ of the individual particles with respect to the incoming flow. More importantly, we observe that our earlier finding of sine-squared scaling of drag for isolated particles holds even for a multiparticle system in both the viscous and inertial regimes. Similarly, we observe that the lift in a multiparticle system follows sine-cosine scaling, as was observed for isolated particles. Such findings are very helpful since the pressure drop of a packed bed or porous media can be computed with just the knowledge of orientation distribution of particles and their drag at $\phi = 0°$ and $\phi = 90°$ for a given Re and ϵ_s. With the identified dependent parameters, correlations for average drag, lift and torque are proposed for a multiparticle system.

SAMENVATTING

Gas-vast stromingen genieten de voorkeur in de industrie vanwege hun hoge mate van gas-vast contact, wat resulteert in uitstekende warmte- en stofoverdrachtseigenschappen. Om deze reden is fluïdisatie nog steeds één van de voornaamste industriële processen in de chemische, energie, metallurgische en farmaceutische industrie. Computersimulaties worden breed toegepast om dergelijke fluïdisatieprocessen te begrijpen en te verbeteren. Echter, door de huidige grenzen aan de rekenkracht, is een meerschaalsaanpak vereist. Op het meest fundamentele niveau worden Direct Numerical Simulations (DNS) uitgevoerd om hydrodynamische krachtcorrelaties te ontwikkelen voor simulaties op grotere schaal. Conventioneel, wordt DNS uitgevoerd voor stroming rond een verzameling bollen. Er bestaat echter geen duidelijke consensus in de wetenschappelijke gemeenschap over hoe de resultaten samen te vatten voor echte deeltjes, welke vaak niet rond zijn. Dit komt door de moeilijkheid om de afhankelijke variabelen te vinden, welke een systeem van meerdere niet-ronde deeltjes adequaat beschrijven.

Dit werk, gefinancierd door de European Research Council, richt zich op het maken van een recept voor het parametriseren van de stroming rond verzamelingen niet-ronde deeltjes. Een multi-relaxatie tijd rooster Boltzmann methode (MRT-LBM) wordt gebruikt om de stroming te simuleren. Dit werk richt zich op 3 verschillende ontwikkelingen. Ten eerste worden verschillende randvoorwaarden, welke in de literatuur beschikbaar zijn, getest om de beste voor het stromingsprobleem te vinden. Met het gebruik van geïnterpoleerde terugstuiter schema's om de geometrie nauwkeurig te beschrijven, is er een probleem met massa lekkage/toename, wat een probleem kan zijn voor stromingen met periodieke randvoorwaarden. Om dit probleem aan te pakken, worden verschillende nieuwe types massacorrectieschema's onderzocht, en worden voorstellen gemaakt voor verschillende stromingscondities.

Het tweede deel van dit proefschrift legt zich toe op de ontwikkeling van meer breed toepasbare schalingswetten voor wrijving en hefkrachten voor verschillende geïsoleerde niet-ronde deeltjes. Dit is belangrijk omdat er verschillende vormen en groottes niet-ronde deeltjes bestaan. Daarom kunnen simpele schalingswetten veel simulatietijd en kosten besparen. Tijdens dit proces, hebben we geobserveerd dat de *sinus-kwadraat* schaling voor wrijving, voorspeld voor viskeuze stroming, ook geldig is in het inertiale regime (hoge *Re*),

vooral voor langgerekte deeltjes. Op eenzelfde manier, is de *sinus-cosinus* schaling voor hefkracht, voorspeld voor viskeuze stroming, ook een goede benadering in het inertiale regime voor langgerekte deeltjes. De reden voor een dergelijke schaling in het inertiale regime is niet vanwege stromingslineariteit, zoals voor viskeuze stroming, maar vanwege een interessant patroon van drukverdeling op de deeltjes bij hoge Re. De drukverdeling welke bijdraagt aan de wrijving en hefkracht laat een afhankelijkheid zien van de hoek tussen de plaatselijke oppervlaktenormaal en de inkomende stroming. Hierna zijn correlaties voorgesteld voor wrijving, hefkracht, en draaimoment op verschillende geïsoleerde niet-ronde deeltjes van de viskeuze limiet tot hoge Reynolds nummer stromingen met $Re \leq 2000$.

In het derde deel wordt een recept voor het beschrijven van hydrodynamische krachten op verzamelingen axisymmetrische niet-ronde deeltjes voorgesteld. Met de beschreven parameters, worden correlaties voor de wrijving, hefkracht en draaimoment voorgesteld. Op dit moment bestaat er nog geen systematische studie om de afhankelijke parameters te identificeren voor stroming rond verzamelingen niet-ronde deeltjes. Naast het Reynolds nummer Re en de vaste volumefractie ϵ_s, stellen we vier additionele parameters voor om de stroming door niet-ronde deeltjesverzamelingen te karakteriseren. Twee parameters nemen de relatieve oriëntaties van de deeltjes voor hun rekening, en twee parameters representeren de richting van de stroming. We vinden een belangwekkend resultaat dat de gemiddelde resultaten onafhankelijk zijn van de hierboven beschreven vier additionele parameters. Voor een gegeven Re en ϵ_s, observeren we dat de enige parameter die de deeltjesconfiguratie beschrijft de invalshoek ϕ van de individuele deeltjes met betrekking tot de inkomende stroming is. Belangrijker nog, vinden we dat onze eerder gevonden sinus-kwadraat schaling voor wrijving op een geïsoleerd deeltje ook voor een meer-deeltjes systeem standhoudt in zowel de viskeuze als het inertiale regime. Eveneens observeren we dat de hefkracht in een meer-deeltjes systeem de sinus-cosinus schaling volgt, zoals voor geïsoleerde deeltjes. Dergelijke bevindingen zijn nuttig omdat de drukval over een gepakt bed of poreuze media berekend kan worden met slechts de kennis van de oriëntatie-distributie van de deeltjes en hun wrijving bij $\phi = 0°$ en $\phi = 90°$ voor een gegeven Re en ϵ_s. Met de geïdentificeerde parameters, zijn correlaties voorgesteld voor gemiddelde wrijving, hefkrant en draaimoment op deeltjes in meer-deeltjes systemen.

1

INTRODUCTION

Figure 1.1: Pellets of different sizes made from various plant and agricultural residues. Source: `volvit.eu`

1.1. BACKGROUND AND MOTIVATION

Particulate flows occur in many natural and man-made processes. Common examples of particulate flows in nature are sediment transport in water bodies, transport of volcanic ash, and red blood cells in plasma, etc. Examples of man-made industrial processes are fluidization of powdered coal, fluidization of milled biomass, and fibrous pulp in paper making, etc. Among the industrial processes, fluidization is highly preferred due to several advantages compared to their alternative such as packed bed systems. The prime advantages are high heat and mass transfer, uniform and controllable temperatures mainly due to good gas-solid contact (Kunii & Levenspiel, 2013). Therefore, there is a growing need to understand the physical nature of such phenomena, which can improve the design of fluidized systems.

Traditionally, the design of fluidized systems is done using empirical knowledge, often scaled up based on lab-scale experiments. The main disadvantage of such a procedure is that the scaling laws do not apply straight-forward in gas-solid flows, often resulting in sub-optimal system performance. Computer simulations can be of great help in understanding and improving fluidization processes. Simulation strategies have successfully been developed over the past decades for gas-solid flows in which particles are approximated as spheres. However, particles in practical systems are often non-spherical in nature. Unfortunately there is no clear methodology available at the moment to simulate gas-solid flows of non-spherical particles. The work described in this thesis is part of a larger project funded by the European Research Council (ERC) aimed at understanding and improving the fluidization of non-spherical particles. The end application is to successfully simulate a system of biomass-like non-spherical particles.

The organic wastes from plants and agricultural wastes are commonly re-
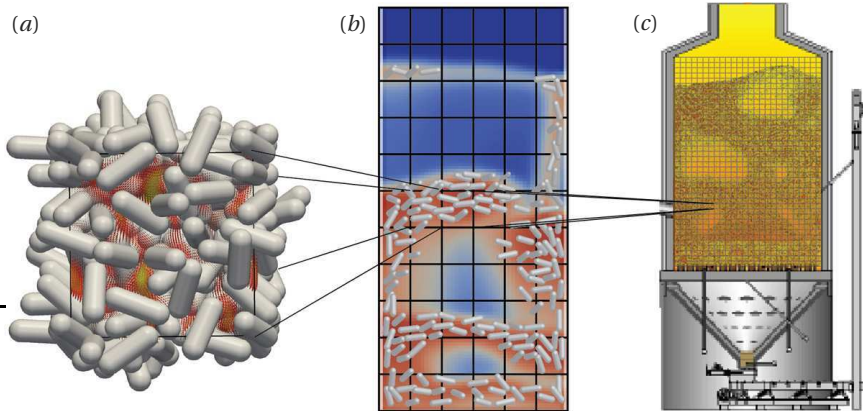
Figure 1.2: Multiscale modelling of non-spherical particles: (*a*) Direct numerical simulations, (*b*) Euler-Lagrangian simulations (also called CFD-DEM), and (*c*) coarse grained simulations.

ferred to as biomass. Biomass is a promising feedstock for the production of renewable energy, materials and chemicals. The preparation of biomass is done in several steps: harvesting, transportation, drying, and (often) subsequent compaction to pellets as shown in figure 1.1. Such biomass particles can be fed to fluidized bed gasifiers to be converted to syngas, a mixture of hydrogen, carbon monoxide and carbon dioxide. In the next section, the strategy for simulating the fluidization of such non-spherical particles is explained.

1.2. MULTISCALE MODELLING OF NON-SPHERICAL PARTICLE FLOWS

Though there is increasing attention towards simulations, a fully resolved simulation of a fluidized bed is not possible at the moment. This is due to limitations in current computational power, which mandates the need for a multi-scale modelling approach. Multiscale modelling, as the name suggests, involves connecting flow physics at different scales. An illustration is given in figure 1.2. Three scales are involved in the multiscale modelling of particulate flows namely:

- Direct numerical simulations,
- Euler-Lagrangian simulations, and
- Coarse grained simulations.

At the most fundamental level, fully resolved simulations are performed with

a fluid mesh much smaller than the particle size. Such resolved flow simulations are known as direct numerical simulations (DNS), since the Navier-Stokes equations describing flow physics are directly solved without the use of closures. Due to their high computational cost, DNS are used to simulate systems of up to a few thousand particles. The results from DNS such as the drag, lift and torque closures are consecutively utilized in larger scale simulations.

On the intermediate scale, Euler-Lagrangian simulations (ELS) utilize the results of DNS to simulate larger scale systems. ELS are also known as CFD-DEM simulations. Here, computational fluid dynamics (CFD) for the (averaged) fluid field is coupled with discrete element method (DEM) for particles to describe particulate-flow phenomena. Prime difference between a conventional CFD and DNS is that CFD usually does not resolve all turbulent length scales. Rather, only the averaged flow properties are solved and the local flow fluctuations are modelled using various turbulence models. This simplification enables CFD-DEM to have a fluid mesh size larger than the particles. Often, the CFD mesh size is of the order of two or more particle lengths. Due to the relatively cheaper computational expenses, CFD-DEM simulations are often used to replicate lab-scale fluidization problems and are capable of handling a few million particles. The main bottleneck for CFD-DEM arises from the DEM part to detect and resolve the particle collisions. With GPUs, the simulation speeds of DEM can be significantly increased and can lead to significant improvement of the simulation capacities of CFD-DEM (Gan *et al.*, 2016).

On the coarsest scale, there are different approaches available. Popular methods are the multiphase particle-in-cell (MP-PIC) method and the two fluid model (TFM). MP-PIC also involves tracking of particles, but does not treat detailed collisions as in CFD-DEM, but models the effect of collisions of collections of particles (or parcels). This coarse-graining approach saves significant compute power and makes MP-PIC favourable for industrial scale flows. TFM, as the name suggests, considers the fluid and particles as inter-penetrating continua. Here, kinetic theory of granular flow (KTGF) is used to describe the particle-particle interactions. The continuum representation of the particle phase, accounting for particle-particle collision, vastly reduces the computational costs and is also preferred for industrial flow simulations. Unfortunately, a large amount of assumptions/simplifications in the particle-particle interactions often leads to poor accuracy of MP-PIC and TFM solutions.

1.3. SCOPE AND OUTLINE OF THE THESIS

The scope of this work is to use DNS to create closures for drag, lift and torque on non-spherical particle assemblies, to be later used in CFD-DEM simulations.

We employ the lattice Boltzmann method (LBM) to perform DNS of flow around different non-spherical particles.

Chapter 2 explains the details of the LBM scheme used. Different interpolated bounceback conditions are also tested in this section. Further, the mass leakage issue occurring with interpolated bounceback schemes is addressed through a series of mass correction schemes. Finally, recommendations for choosing a proper boundary condition scheme are given for stable and accurate simulations.

Chapter 3 discusses the results of flow around various non-spherical particles. Interestingly, phenomena such as sine-squared scaling of drag and sine-cosine scaling of lift are observed for various non-spherical particles, even at high Reynolds numbers. The reason behind such scaling behaviour are explained in detail.

Chapter 4 utilizes the scaling laws explained in chapter 3, which are then used to create drag, lift and torque correlations for different non-spherical particles. Physical limits are considered while performing the correlations, which means the correlations can be used satisfactorily beyond the simulated regimes.

Chapter 5 introduces a recipe for parametrizing results of flow around assemblies of non-spherical particles. With the identified dependent parameters, drag, lift and torque closures for multiparticle systems are proposed accordingly.

Chapter 6 provides a summary of the present study and outlook for future studies.

2

NUMERICAL METHOD

The lattice Boltzmann method (LBM) is used to simulate flow around different non-spherical particles. The details of the single and multi-relaxation time LBM schemes are presented in this chapter. Various curved no-slip boundary conditions available in literature improve the accuracy of lattice Boltzmann simulations compared to the traditional stair-case approximation of curved geometries. A performance evaluation of such boundary conditions for different flow problems is presented. Usually, the required unknown distribution functions emerging from the solid nodes are computed based on the known distribution functions using interpolation or extrapolation schemes. On using such curved boundary schemes, there will be mass loss or gain at each time step during the simulations, especially apparent at high Reynolds numbers, which is called mass-leakage. Such an issue becomes severe in periodic flows, where the mass leakage accumulation would affect the forces exerted on the solid objects over time. In this chapter, we examine mass-leakage for the most well-known curved boundary treatments for high Reynolds number flows. Apart from the existing schemes, we also test different forced mass conservation schemes and a constant density scheme. The capability of each scheme is evaluated and finally, recommendations for choosing a proper boundary condition scheme are given for stable and accurate simulations.
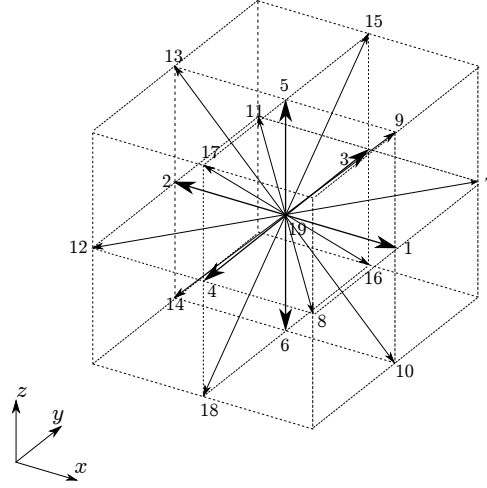
Figure 2.1: D3Q19 lattice configuration with directions α.

2.1. INTRODUCTION

In the last two decades, there has been growing interest in using the lattice Boltzmann method (LBM) as a promising alternative technique for simulating various fluid flow problems (Aidun & Clausen, 2010; Sukop & Thorne, 2006; Zarghami *et al.*, 2015, 2014). Unlike the conventional computational fluid dynamics (CFD) methods, the LBM does not solve the incompressible Navier-Stokes equations directly, but instead the fluid flow is described in terms of a discrete kinetic equation based on the particle distribution functions (Succi, 2001). The standard LBM consists of two steps, namely collision and streaming. The collision step describes the local changes of particle density due to collisions at each grid node. In the streaming step, distribution functions are streamed from lattice nodes to their neighbours. Macroscopic quantities, such as density or velocity, are recovered as statistical moments of the particle distribution functions.

The rest of this chapter is organized as follows. We briefly introduce the LBM scheme in section 2.2. The mass leakage phenomenon is explained in section 2.3 and the investigated no-slip curved boundary conditions are described in section 2.4. Results and discussion are presented in section 2.5 followed by our recommendations and conclusions in sections 2.6 and 2.7 respectively.

2.2. Lattice Boltzmann Method

2.2.1. Single Relaxation Time LBM

The single relaxation time lattice Boltzmann method (SRT-LBM) is given as (Succi, 2001)

$$f_\alpha(\boldsymbol{r} + \boldsymbol{e}_\alpha \Delta t, t + \Delta t) - f_\alpha(\boldsymbol{r}, t) = -\frac{1}{\tau}[f_\alpha(\boldsymbol{r}, t) - f_\alpha^{eq}(\boldsymbol{r}, t)] + S_\alpha, \qquad (2.1)$$

where f_α is the particle distribution function signifying the probability to find a particle at location $\boldsymbol{r}$ with discrete velocity $\boldsymbol{e}_\alpha$. $\boldsymbol{e}_\alpha$ is along different specified directions $\alpha = 1, 2..., 19$ as shown in figure 2.1. f_α^{eq} is the equilibrium distribution, Δt is the time interval, $\tau = 1/\omega$ is the relaxation time, ω is the relaxation factor and S_α represents a general body force, if available, in the direction α. The equilibrium density distribution function is given as

$$f_\alpha^{eq} = w_\alpha \rho \left(1 + \frac{(\boldsymbol{e}_\alpha \cdot \boldsymbol{u})}{c_s^2} + \frac{(\boldsymbol{e}_\alpha \cdot \boldsymbol{u})^2}{2c_s^4} - \frac{(\boldsymbol{u} \cdot \boldsymbol{u})}{2c_s^2} \right), \qquad (2.2)$$

where $\rho = \sum_\alpha f_\alpha$ and $\rho \boldsymbol{u}_\alpha = \sum_\alpha f_\alpha \boldsymbol{e}_\alpha$ are the local density and momentum, respectively. The LBM simulations are performed in lattice units and the lattice speed is $c = \Delta x / \Delta t$ with $\Delta x = 1$ and $\Delta t = 1$. The lattice speed of sound is $c_s = c/\sqrt{3}$. The viscosity and the pressure are calculated respectively as: $\nu = c_s^2(\tau - 0.5)$ and $p = \rho c_s^2$, respectively. It is clear that positivity of viscosity requires that $\tau > 0.5$. The standard LBM timestep is performed in two steps, the collision and the streaming steps respectively, as:

$$\tilde{f}_\alpha(\boldsymbol{r}, t) \qquad = f_\alpha(\boldsymbol{r}, t) - \frac{1}{\tau}[f_\alpha(\boldsymbol{r}, t) - f_\alpha^{eq}(\boldsymbol{r}, t)] + S_\alpha, \qquad (2.3)$$

$$f_\alpha(\boldsymbol{r} + \boldsymbol{e}_\alpha \Delta t, t + \Delta t) \quad = \tilde{f}_\alpha(\boldsymbol{r}, t), \qquad (2.4)$$

where $\tilde{f}_\alpha$ is the post-collision state of the distribution function but before the streaming. The effect of gravity as a body force (Luo, 1993) is applied as : $S_\alpha = -3w_\alpha \rho(\boldsymbol{g} \cdot \boldsymbol{e}_\alpha)$, where $\boldsymbol{g}$ is the gravitational vector.

At high Re, the SRT-LBM scheme suffers instability issues. Therefore, we use multi-relaxation time LBM scheme in all our 3D simulations for better stability.

2.2.2. Multi-Relaxation Time LBM

The multi-relaxation time lattice Boltzmann method (MRT-LBM) proposed by d'Humières *et al.* (2002) separates the relaxation times for different kinetic modes

and thereby improves stability. Here, we use $|f\rangle$ to denote a column vector containing f_α. The MRT-LBM scheme for a D3Q19 scheme (see figure 2.1) with the corresponding evolution of particle distribution function $|f\rangle$ is computed as

$$\left|f(\boldsymbol{r}+\boldsymbol{e}_\alpha\Delta t, t+\Delta t)\right\rangle = \left|f(\boldsymbol{r},t)\right\rangle - M^{-1}\hat{S}(|m(\boldsymbol{r},t)\rangle - |m^{(eq)}(\boldsymbol{r},t)\rangle) \tag{2.5}$$

where

$$M = \begin{pmatrix}
1 & 1 & 1 & 1 & 1 & 1 & 1 & 1 & 1 & 1 & 1 & 1 & 1 & 1 & 1 & 1 & 1 & 1 & 1 \\
-11 & -11 & -11 & -11 & -11 & -11 & 8 & 8 & 8 & 8 & 8 & 8 & 8 & 8 & 8 & 8 & 8 & 8 & -30 \\
-4 & -4 & -4 & -4 & -4 & -4 & 1 & 1 & 1 & 1 & 1 & 1 & 1 & 1 & 1 & 1 & 1 & 1 & 12 \\
1 & -1 & 0 & 0 & 0 & 0 & 1 & 1 & 1 & 1 & -1 & -1 & -1 & -1 & 0 & 0 & 0 & 0 & 0 \\
-4 & 4 & 0 & 0 & 0 & 0 & 1 & 1 & 1 & 1 & -1 & -1 & -1 & -1 & 0 & 0 & 0 & 0 & 0 \\
0 & 0 & 1 & -1 & 0 & 0 & 1 & -1 & 0 & 0 & 1 & -1 & 0 & 0 & 1 & 1 & -1 & -1 & 0 \\
0 & 0 & -4 & 4 & 0 & 0 & 1 & -1 & 0 & 0 & 1 & -1 & 0 & 0 & 1 & 1 & -1 & -1 & 0 \\
0 & 0 & 0 & 0 & 1 & -1 & 0 & 0 & 1 & -1 & 0 & 0 & 1 & -1 & 1 & -1 & 1 & -1 & 0 \\
0 & 0 & 0 & 0 & -4 & 4 & 0 & 0 & 1 & -1 & 0 & 0 & 1 & -1 & 1 & -1 & 1 & -1 & 0 \\
2 & 2 & -1 & -1 & -1 & -1 & 1 & 1 & 1 & 1 & 1 & 1 & 1 & 1 & -2 & -2 & -2 & -2 & 0 \\
-4 & -4 & 2 & 2 & 2 & 2 & 1 & 1 & 1 & 1 & 1 & 1 & 1 & 1 & -2 & -2 & -2 & -2 & 0 \\
0 & 0 & 1 & 1 & -1 & -1 & 1 & 1 & -1 & -1 & 1 & 1 & -1 & -1 & 0 & 0 & 0 & 0 & 0 \\
0 & 0 & -2 & -2 & 2 & 2 & 1 & 1 & -1 & -1 & 1 & 1 & -1 & -1 & 0 & 0 & 0 & 0 & 0 \\
0 & 0 & 0 & 0 & 0 & 0 & 1 & -1 & 0 & 0 & -1 & 1 & 0 & 0 & 0 & 0 & 0 & 0 & 0 \\
0 & 0 & 0 & 0 & 0 & 0 & 0 & 0 & 0 & 0 & 0 & 0 & 0 & 0 & 1 & -1 & -1 & 1 & 0 \\
0 & 0 & 0 & 0 & 0 & 0 & 0 & 0 & 1 & -1 & 0 & 0 & -1 & 1 & 0 & 0 & 0 & 0 & 0 \\
0 & 0 & 0 & 0 & 0 & 0 & 1 & 1 & -1 & -1 & -1 & -1 & 1 & 1 & 0 & 0 & 0 & 0 & 0 \\
0 & 0 & 0 & 0 & 0 & 0 & -1 & 1 & 0 & 0 & -1 & 1 & 0 & 0 & 1 & 1 & -1 & -1 & 0 \\
0 & 0 & 0 & 0 & 0 & 0 & 0 & 0 & 1 & -1 & 0 & 0 & 1 & -1 & -1 & 1 & 1 & -1 & 0
\end{pmatrix}$$

$$\tag{2.6}$$

is a 19×19 transformation matrix used to transform $|f\rangle$ from velocity space to moment space $|m\rangle$ with $|m\rangle = M \cdot |f\rangle$. The relaxation matrix $\hat{S} = M \cdot S \cdot M^{-1}$ is a 19×19 diagonal matrix. For the D3Q19 model, the 19 moments are

$$|m\rangle = (\rho, e, \epsilon, j_x, q_x, j_y, q_y, j_z, q_z, 3p_{xx}, 3\pi_{xx}, p_{ww}, \pi_{ww}, p_{xy}, p_{yz}, p_{zx}, m_x, m_y, m_z)^T, \tag{2.7}$$

where density $\rho = \sum_\alpha f_\alpha$ and momentum $\boldsymbol{j} = (j_x, j_y, j_z) = \rho\boldsymbol{u} = \sum_\alpha f_\alpha e_\alpha$ are the conserved moments. The non-conserved moments are as follows: e is the part of kinetic energy independent of density, ϵ is the part of kinetic energy squared independent of both the density and kinetic energy ($\epsilon = e^2$), and q_i is the energy flux independent of mass flux (d'Humières *et al.*, 2002). Here, subscript i denotes x, y, or z-coordinates. $p_{xx}, p_{xy}, p_{yz}, p_{xz}$ and p_{ww} are the symmetric traceless viscous stress tensor with $p_{ww} = p_{yy} - p_{zz}$ and $p_{xx} + p_{yy} + p_{zz} = 0$. m_x, m_y and m_z are the third order moments. π_{xx} and π_{ww} are fourth order moments. The equilibria of non-conserved moments are given as functions of ρ and $\boldsymbol{j}$ (d'Humières

et al., 2002) as

$$e^{(eq)} = -11\rho + \frac{19}{\rho_0}\boldsymbol{j}\cdot\boldsymbol{j} = -11\rho + \frac{19}{\rho_0}(j_x^2 + j_y^2 + j_z^2), \tag{2.8}$$

$$\epsilon^{(eq)} = w_\epsilon\rho + \frac{w_{\epsilon j}}{\rho_0}\boldsymbol{j}\cdot\boldsymbol{j}, \tag{2.9}$$

$$q_x^{(eq)} = -\frac{2}{3}j_x, \qquad q_y^{(eq)} = -\frac{2}{3}j_y, \qquad q_z^{(eq)} = -\frac{2}{3}j_z, \tag{2.10}$$

$$p_{xx}^{(eq)} = \frac{1}{3\rho_0}(2j_x^2 - (j_y^2 + j_z^2)), \qquad p_{ww}^{(eq)} = \frac{1}{\rho_0}(j_y^2 - j_z^2), \tag{2.11}$$

$$p_{xy}^{(eq)} = \frac{1}{\rho_0}j_x j_y, \qquad p_{yz}^{(eq)} = \frac{1}{\rho_0}j_y j_z, \qquad p_{xz}^{(eq)} = \frac{1}{\rho_0}j_x j_z, \tag{2.12}$$

$$\pi_{xx}^{(eq)} = w_{xx}p_{xx}^{(eq)}, \qquad \pi_{ww}^{(eq)} = w_{xx}p_{ww}^{(eq)}, \tag{2.13}$$

$$m_x^{(eq)} = m_y^{(eq)} = m_z^{(eq)} = 0, \tag{2.14}$$

where ρ_0 is the average density in the system. In our simulations, $\rho_0 = 1$, $w_\epsilon = 3, w_{\epsilon j} = -11/2$, and $w_{xx} = -1/2$. The factor $1/\rho_0$ used in the above equilibrium expressions is to reduce compressibility effects (He & Luo, 1997; d'Humières *et al.*, 2002). The diagonal collision matrix $\hat{S}$ (d'Humières *et al.*, 2002; Huang *et al.*, 2012) is

$$\hat{S} = \mathrm{diag}(0, s_1, s_2, 0, s_4, 0, s_4, 0, s_4, s_9, s_{10}, s_9, s_{10}, s_{13}, s_{13}, s_{13}, s_{16}, s_{16}, s_{16}), \tag{2.15}$$

with $s_1 = 1.19$, $s_2 = s_{10} = 1.4$, $s_4 = 1.2$, $s_9 = s_{13} = 1/\tau$ and $s_{16} = 1.98$. The kinematic viscosity of the fluid is related to the relaxation time τ by $\nu = c_s^2(\tau - 1/2)\Delta t$, and pressure p is related to density by $p = \rho c_s^2$.

2.2.3. FORCE AND TORQUE EVALUATION

The momentum contribution along a single fluid-solid link exerted on the particle by the fluid is computed using the momentum exchange method (Bouzidi *et al.*, 2001; Mei *et al.*, 2002; Lallemand & Luo, 2003) as

$$\boldsymbol{p}_\alpha(\boldsymbol{r}_b, t) = \boldsymbol{e}_\alpha(f_\alpha(\boldsymbol{r}_b, t) + f_{\overline{\alpha}}(\boldsymbol{r}_f, t)), \tag{2.16}$$

where $\boldsymbol{r}_b$ is the boundary solid node with $\boldsymbol{r}_b = \boldsymbol{r}_f + \boldsymbol{e}_\alpha\Delta t$. Correspondingly, the force and torque are computed as

$$\boldsymbol{F} = \sum_{\text{all } \boldsymbol{r}_b}\sum_{\alpha \neq 19}\boldsymbol{p}_\alpha(\boldsymbol{r}_b, t) \tag{2.17}$$

$$\boldsymbol{T} = \sum_{\text{all } \boldsymbol{r}_b}\sum_{\alpha \neq 19}(\boldsymbol{r}_w - \boldsymbol{r}_c) \times \boldsymbol{p}_\alpha(\boldsymbol{r}_b, t). \tag{2.18}$$

Here, $\boldsymbol{r}_w$ is the position of the particle wall and $\boldsymbol{r}_c$ is the center of gravity of the particle.

2.3. MASS LEAKAGE IN INTERPOLATED BOUNCE-BACK SCHEMES

Since the LBM is performed on equidistant Cartesian grids, boundary condition schemes were first introduced for straight walls. The bounce-back (BB) scheme is the most common, simplest and exactly mass conserving scheme for the solid wall boundary condition and provides a particularly straightforward approach for modelling no-slip conditions on solid walls. In this scheme, when a particle distribution streams to a wall node, it reflects back to the fluid node along its incoming link (Succi, 2001; Wolf-Gladrow, 2004). The on-site BB and the mid-grid BB are two types of BB schemes (Ziegler, 1993). In the on-site BB scheme, the physical boundary nodes lay exactly at the lattice nodes. In the mid-grid BB scheme, the solid boundary is located exactly mid-plane between the boundary fluid node and the off-lattice node inside the solid. The on-site BB scheme is first-order accurate, whereas the mid-grid BB scheme provides second-order accuracy in both space and time (Succi, 2001). Alternative wall boundary conditions with second-order accuracy were proposed by various researchers (Ziegler, 1993; Noble *et al.*, 1995; Inamuro *et al.*, 1995; Skordos, 1993). For all of these boundary condition treatments, the solid wall should be aligned with the computational grid (Latt *et al.*, 2008; Chen *et al.*, 1996).

   The above-mentioned schemes have been quite successful in improving numerical accuracy for flows with flat-wall boundaries aligned with the computational grid. However, they fail to accurately simulate curved boundaries (or flat-wall boundaries inclined with respect to the computational grid). For simulating flow with curved boundaries, we need to determine the distribution functions at the nodes nearest the curved boundaries based on the known boundary conditions. The use of BB schemes with curved boundaries leads to stair-case shaped boundaries (Ladd, 1994*a*; Ladd & Verberg, 2001). It should be noted that with a stair-shaped approximation, not only the fidelity of real geometry is lost, it may also introduce undesired errors (such as a non-zero wall velocity) in a simulation that could contaminate the results (Kandhai *et al.*, 1999).

   In the literature, various boundary treatments have been developed that provide a more accurate treatment of curved boundaries to determine the distribution functions on the boundary nodes. The first method for treating curved boundaries with the LBM was proposed by Filippova and Hanel based on inter/extrapolation of the distribution functions (Filippova & Hänel, 1997). It relies on ghost cells inside solid walls and applies a linear interpolation of particle distributions to enforce the boundary condition at the exact boundary location. This scheme has second order accuracy. However, it suffers from poor numerical stability, particularly when the near-wall fluid node is very close to the solid boundary. The stability issue of this scheme was improved by Mei *et al.* (1999)

by placing the boundary node used for velocity interpolation to the closest fluid nodes, if the actual wall boundary is too close to a solid node. The stability of this method was further improved by various researchers (Guo *et al.*, 2002; Tiwari & Vanka, 2012).

Bouzidi *et al.* (2001) proposed a method with second-order accuracy that does not require the extrapolations from the ghost nodes in solid wall. The proposed scheme combines the bounce-back concept with linear/quadratic interpolation of the distribution functions from the internal fluid nodes. The accuracy of this method has been improved by Ginzburg & d'Humières (2003) and extended to moving boundaries by Lallemand & Luo (2003). Yu *et al.* (2003*b*) proposed a unified version of the Bouzidi scheme by using a two-step sequential interpolations to avoid the discontinuity in the boundary treatment. Yin & Zhang (2012) modified the Ladd scheme with the boundary velocity at the midgrid computed using inter/extrapolation between the boundary node and fluid node. In addition to the above-mentioned boundary methods, several other approaches have been developed for simulating curved boundaries in the LBM (Feng & Michaelides, 2004; Suzuki & Inamuro, 2011; Ginzburg *et al.*, 2008). The different boundary conditions of LBM are compared on different lattice configurations by Nash *et al.* (2014).

Usually when using the inter/extrapolation-based curved boundary schemes in the LBM simulations, the mass of the system is not conserved exactly. In other words, there will be mass loss/gain at each time step during the simulation, which is called mass-leakage in the literature. Lallemand & Luo (2003) showed that the use of interpolation breaks mass conservation near curved boundaries. They found that the inaccuracy in evaluating momentum transfer can lead to a net mass flux at the boundary. There are also flux based finite-volume boundary schemes that are designed to conserve mass (Chen *et al.*, 1998; Rohde *et al.*, 2002). However, these require estimates of the cut-cell volume of the boundary cells, which add further complexity. From an implementation point-of-view, link based interpolation methods are much simpler. Various mass conserving boundary treatments have been proposed to avoid the mass-leakage issue and improve the numerical stability of the simulations (Kao & Yang, 2008; Bao *et al.*, 2008; Le Coupanec & Verschaeve, 2011). However, such proposed mass conserving boundary conditions either still exhibit minor leakage (Kao & Yang, 2008), are not analysed rigorously for mass leakage through various testcases (Chen *et al.*, 1998; Bao *et al.*, 2008), or are applicable only for specific problems such as tangential boundaries (Le Coupanec & Verschaeve, 2011). In general, such a mass leakage does not affect simulation results for inflow-outflow boundaries (Sanjeevi & Padding, 2017). However, the mass leakage accumulates over time for a periodic flow, driven by gravity. Such a flow problem is widely used in differ-

ent areas such as flows around stationary arrays of particles and flows through porous media. For low Re flows, such a leakage is minor and can be ignored in general. However at high Re, the change in system mass is large and cannot be ignored. The issue becomes even severe in the case of unsteady periodic flows, where a large number of time steps is required to reach statistical equilibrium. This subsequently results in drift in system mass and therefore, constantly increasing or decreasing forces.

In the following sections, we discuss the existing curved boundary conditions and analyse their performance. Our objective is to keep the grid Re high (relatively coarser grid and lower viscosity), since the mass leakage effects are directly a consequence and proportional to the grid Re than the flow Re itself. By this, we imply the importance of achieving good solution accuracy using a coarse grid against finer grid simulations as they are computationally more expensive.

Up to this point, there has not yet been a systematic comparison of the performance of curved boundary schemes with focus on mass leakage. We test the accuracy of most popular curved boundary condition schemes and schemes that showed potential for solving the mass leakage issue. It is the aim of this section to provide such a comparison for cases with significant mass-leakage issue, with focus on high Re flows. Further, in this section, we introduce forced conservation schemes that enforce strict mass conservation and test their performance.

2.4. TREATMENTS FOR CURVED-WALL BOUNDARY

Because a no-slip boundary with a wall can be modelled for each velocity direction separately, it is sufficient to consider a single lattice direction with a (curved) wall boundary surface at r_w, as shown in figure 2.2. The curved-wall boundary may be located at an arbitrary position between the solid and fluid nodes (i.e. r_b and r_f). The fraction of an intersected link in the fluid region is expressed using a parameter q as

$$q = \frac{|r_w - r_f|}{|r_b - r_f|}. \tag{2.19}$$

Various treatments for curved-wall boundary condition have been proposed in the literature to improve the accuracy of the LBM simulations. The work of Filippova & Hänel (1997) and Mei *et al.* (1999) were the first attempts to represent curved boundaries of a solid body. However, they are not stable for all relaxation times (Yu *et al.*, 2003*a*; Kao & Yang, 2008) and therefore are not considered in this work. Since the boundary schemes are formulated based on 1D approximation of the lattice direction, 2D testcases are sufficient to investigate their performance. Historically also, all or most of the proposed curved bound-
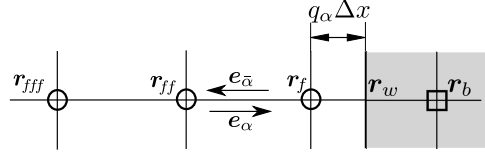
Figure 2.2: One-dimensional representation of a regular lattice and a curved-wall boundary.

ary condition literatures contain 2D testcases. Their extensions to 3D are always straight-forward and consistent. For this reason, we perform only 2D flow test-cases in the upcoming sections of this chapter. We use D2Q9 boundary condition to test the different boundary conditions. The lattice weights w_α and the discrete velocities $\boldsymbol{e}_\alpha$ of a D2Q9-lattice model are given by: $w_{\alpha=0} = 4/9$, $\boldsymbol{e}_\alpha = (0,0)$, $w_{\alpha=1\sim4} = 1/9$, $\boldsymbol{e}_\alpha = (\cos\theta_\alpha, \sin\theta_\alpha)$ with $\theta_\alpha = (\alpha - 1)\pi/2$ and $w_{\alpha=5\sim8} = 1/36$, $\boldsymbol{e}_\alpha = \sqrt{2}(\cos\theta_\alpha, \sin\theta_\alpha)$ with $\theta_\alpha = (\alpha - 5)\pi/2 + \pi/4$. In this section, we briefly introduce the schemes that are analysed in this work.

2.4.1. THE MIDGRID BOUNCE-BACK SCHEME

The most widely used boundary condition for the LBM is the midgrid bounce-back scheme (MGBB). For a midgrid bounce back scheme, the solid boundary is assumed exactly half-way between the fluid node and the solid node (i.e. $q = 1/2$). The midgrid bounce back scheme (see figure 2.2) is of second order and is given by:

$$f_{\bar{\alpha}}(\boldsymbol{r}_f, t + \Delta t) = \tilde{f}_\alpha(\boldsymbol{r}_f, t).\tag{2.20}$$

2.4.2. THE BOUZIDI SCHEMES

In this scheme, an interpolation is applied to calculate the unknown distribution function based on the position of the wall boundary. When linear interpolation is applied, the Bouzidi model (L-Bouzidi) is written as follows:

For $q < 0.5$:

$$f_{\bar{\alpha}}(\boldsymbol{r}_f, t + \Delta t) = (1 - 2q)\tilde{f}_\alpha(\boldsymbol{r}_{ff}, t) + 2q\tilde{f}_\alpha(\boldsymbol{r}_f, t),\tag{2.21}$$

and for $q \geq 0.5$:

$$f_{\bar{\alpha}}(\boldsymbol{r}_f, t + \Delta t) = \left(1 - \frac{1}{2q}\right)\tilde{f}_{\bar{\alpha}}(\boldsymbol{r}_f, t) + \frac{1}{2q}\tilde{f}_\alpha(\boldsymbol{r}_f, t).\tag{2.22}$$

Alternatively, when quadratic interpolation is applied, the scheme (Q-Bouzidi) has the following form for $q < 0.5$:

$$f_{\bar{\alpha}}(\boldsymbol{r}_f, t + \Delta t) = q(1 + 2q)\tilde{f}_\alpha(\boldsymbol{r}_f, t) + (1 - 4q^2)\tilde{f}_\alpha(\boldsymbol{r}_{ff}, t) - q(1 - 2q)\tilde{f}_\alpha(\boldsymbol{r}_{fff}, t)), \quad (2.23)$$

and for $q \geq 0.5$:

$$f_{\bar{\alpha}}(\boldsymbol{r}_f, t + \Delta t) = \frac{1}{q(2q + 1)}\tilde{f}_i(\boldsymbol{r}_f, t) + \frac{2q - 1}{q}\tilde{f}_{\bar{\alpha}}(\boldsymbol{r}_f, t) - \frac{2q - 1}{2q + 1}\tilde{f}_{\bar{\alpha}}(\boldsymbol{r}_{ff}, t). \quad (2.24)$$

It can observed that in the Bouzidi schemes, the unknown values of distribution functions are solved at the fluid nodes using an interpolation technique.

2.4.3. THE UNIFIED SCHEMES

The Bouzidi scheme requires separate treatments for $q < 0.5$ and $q \geq 0.5$ that may cause an abrupt change in calculated distribution function when q changes from less than 0.5 to more than 0.5 (as in moving boundaries). To overcome this issue, a unified version of the Bouzidi scheme was proposed by Yu *et al.* (2003*b*). The linear interpolation of Yu scheme (L-Uni) is written as:

$$f_{\bar{\alpha}}(\boldsymbol{r}_f, t + \Delta t) = \frac{1}{1 + q}[q\tilde{f}_\alpha(\boldsymbol{r}_f, t) + (1 - q)\tilde{f}_\alpha(\boldsymbol{r}_{ff}, t) + q\tilde{f}_{\bar{\alpha}}(\boldsymbol{r}_f, t)]. \quad (2.25)$$

If quadratic interpolation is applied (Kao & Yang, 2008), the model (Q-Uni) has the form:

$$\begin{aligned}
f_{\bar{\alpha}}(\boldsymbol{r}_f, t + \Delta t) = \frac{1}{(1 + q)(2 + q)}[q(1 + q)\tilde{f}_\alpha(\boldsymbol{r}_f, t) + 2(1 - q^2)\tilde{f}_\alpha(\boldsymbol{r}_{ff}, t) - \\
q(1 - q)\tilde{f}_\alpha(\boldsymbol{r}_{fff}, t) + 2q(2 + q)\tilde{f}_{\bar{\alpha}}(\boldsymbol{r}_f, t) - q(1 + q)\tilde{f}_{\bar{\alpha}}(\boldsymbol{r}_{ff}, t)].
\end{aligned} \quad (2.26)$$

It can be seen that the Yu scheme does not require conditional branching (by $q <$ or > 0.5). However, compared to the Bouzidi scheme, the Yu scheme involves more operations and distribution function evaluations.

2.4.4. THE INTERPOLATION-FREE SCHEMES

Previous investigations (Lallemand & Luo, 2003) indicated that interpolation-based schemes for treatment of curved boundaries destroy mass conservation at the boundaries. To overcome the drawback of these interpolation-based curved

boundary treatments, an interpolation-free technique was proposed by Kao &
Yang (2008). The interpolation free schemes are based on the concept of local
grid refinement similar to Filippova & Hänel (1998), albeit without the actual grid
refinement. The viscosities are modified depending on the q values, to mimic a
finer local grid. In the proposed on-site interpolation-free (OSIF) scheme, the
fluid distribution function is computed in the post-collision step and is then
streamed to the surface of the solid node $\boldsymbol{r}_b$. For all $0 < q \leq 1$:

$$\tilde{f}_\alpha(\boldsymbol{r}_f, t) = f_\alpha^{eq}(\boldsymbol{r}_f, t) + [\tilde{f}_\alpha(\boldsymbol{r}_f, t) - f_\alpha^{eq}(\boldsymbol{r}_f, t)]\frac{q\omega^c(1-\omega^f)}{\omega^f(1-\omega^c)}, \qquad (2.27)$$

where $\omega^c = \omega$, $\omega^f = 2q/(q-1+2\tau)$ and the superscripts c and f denote the coarse
and fine grid quantities. The composite interpolation-free (CPIF) model, as the
name suggests, is a hybrid approach encompassing midgrid and onsite bounce
back schemes. The viscosity is modified, accordingly resembling a midgrid
bounceback for $q \leq 0.5$ and an onsite bounceback for $q > 0.5$. For $q \leq 0.5$, the
fine-grid relaxation factor is $\omega^f = 4q/(2q-1+2\tau)$ and

$$\tilde{f}_{\bar{\alpha}}(\boldsymbol{r}_b, t) = f_\alpha^{eq}(\boldsymbol{r}_f, t) + [\tilde{f}_\alpha(\boldsymbol{r}_f, t) - f_\alpha^{eq}(\boldsymbol{r}_f, t)]\frac{2q\omega^c(1-\omega^f)}{\omega^f(1-\omega^c)}. \qquad (2.28)$$

For $q > 0.5$, $\omega^f = 2q/(q-1+2\tau)$ and

$$\tilde{f}_\alpha(\boldsymbol{r}_f, t) = f_\alpha^{eq}(\boldsymbol{r}_f, t) + [\tilde{f}_\alpha(\boldsymbol{r}_f, t) - f_\alpha^{eq}(\boldsymbol{r}_f, t)]\frac{q\omega^c(1-\omega^f)}{\omega^f(1-\omega^c)}. \qquad (2.29)$$

2.4.5. THE YIN-ZHANG SCHEME

Yin & Zhang (2012) proposed a modified version (Yin-Zhang) of the midgrid
BB scheme with moving boundaries (Ladd, 1994a) based on the velocity at the
midgrid position instead of the boundary velocity. The midgrid velocity is ob-
tained by inter-/extrapolating the velocities from the boundary and the fluid
node. For this purpose, the midpoint velocity of a boundary lattice link is cal-
culated as follows. With $\Delta = 1 - q$, and for $\Delta \leq 0.5$,

$$\boldsymbol{u}_m = \frac{0.5\boldsymbol{u}(\boldsymbol{r}_b, t) + (0.5 - \Delta)\boldsymbol{u}(\boldsymbol{r}_f, t)}{1 - \Delta} \qquad (2.30)$$

and for $\Delta > 0.5$,

$$\boldsymbol{u}_m = \frac{1.5\boldsymbol{u}(\boldsymbol{r}_b, t) - (\Delta - 0.5)\boldsymbol{u}(\boldsymbol{r}_{ff}, t)}{2 - \Delta}. \qquad (2.31)$$

This midpoint velocity is utilized to calculate the bounced back distribution functions as:

$$f_{\tilde{\alpha}}(\boldsymbol{r}_f, t + \Delta t) = \tilde{f}_{\alpha}(\boldsymbol{r}_f, t) - \frac{2w_{\alpha}\rho(\boldsymbol{r}_f, t)}{c_s^2}\boldsymbol{u}_m \cdot \boldsymbol{e}_{\alpha}. \qquad (2.32)$$

It is worth mentioning that from a coding perspective, when using the curved boundary schemes, it is more efficient to compute the unknown distribution functions after the streaming step (Lallemand & Luo, 2003). Streaming simply corresponds to shift of indices of the spatial nodes. This means that: $\tilde{f}_{\tilde{\alpha}}(\boldsymbol{r}_b, t) = f_{\tilde{\alpha}}(\boldsymbol{r}_f, t + \Delta t)$ or $\tilde{f}_{\alpha}(\boldsymbol{r}_{ff}, t) = f_i(\boldsymbol{r}_f, t + \Delta t)$ and so on. Therefore, the curved boundary schemes can also be re-written based on the distributions after the streaming. Regarding implementation, all the schemes are straight-forward to implement. However, the CPIF scheme is slightly complicated due to its combined mid-grid and onsite bounceback approach. Regarding computational performance, we observed near similar behaviour of all boundary schemes for different testcases and therefore, the schemes are not compared for execution speed.

2.5. RESULTS AND DISCUSSION

In this section, the no-slip curved boundary treatments of section 2.4 are applied to different flow testcases. Here the midgrid bounce-back, linear Bouzidi, quadratic Bouzidi, linear unified, quadratic unified, on-site interpolation free, composite interpolation free and the Yin-Zhang schemes are labelled as: MGBB, L-Bouzidi, Q-Bouzidi, L-Uni, Q-Uni, OSIF, CPIF and Yin-Zhang, respectively. Also, we introduce forced mass conservation cases and a constant density scheme, and investigate their performance.

2.5.1. FLOW AROUND SQUARE CYLINDER INSIDE A CHANNEL

In this testcase, we simulate the flow around a square cylinder confined between two parallel walls. The flow is periodic and is driven by gravity. The main advantage of this testcase is that all the simulation boundaries are grid aligned. This enables accurate simulation of the flow field using mid-grid bounce-back scheme and subsequently compare different boundary conditions for arbitrary position of the obstacle. The simulated test case is shown in figure 2.3 and is made of 200×51 nodes. The top and bottom walls of the channel are positioned half-way between their respective solid-fluid nodes. Effectively, the channel width is of 49 lattice units. The square obstacle is of size 15×15 lattice units. Different boundary conditions are tested with obstacle at different positions with the centers (C_x) starting from 50 to 51 along x-axis in 0.25 increments. All four sides of the obstacle are half-way between the solid-fluid node for the initial and final C_x
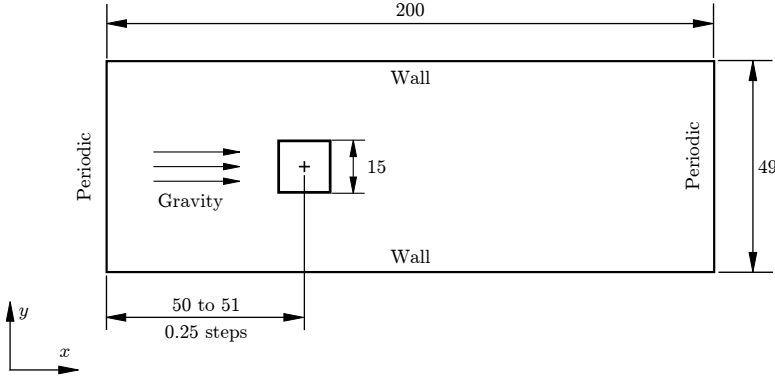
Figure 2.3: Simulation setup for flow around a square obstacle, driven by gravity.

positions, i.e. $C_x = 50$ and 51. The top and bottom sides of the obstacle are always halfway between solid-fluid nodes for all C_x. In other words, the q values for top and bottom sides of the square are always equal to 0.5 whereas q values change for front and rear sides of the square for different C_x.

Two different Re are simulated by appropriately changing the gravity - one with steady flow at $Re = 150$ and another with unsteady flow at $Re = 330$. Here, $Re = U_m H / \nu$ with U_m being the average x-velocity component (U_x) measured at the outflow of the domain and H is the domain height. It should be noted that the viscosity is maintained low such that the Re is high in order to deliberately amplify the mass-leakage effects. The relaxation time is maintained at $\tau = 0.52$ for both cases. At the same time, the maximum lattice velocity is kept below 0.15 to avoid compressibility effects.

The metrics we use to analyse the results are the change in system mass (m') at the end of simulations, the normalized flow rate (Q'), and the normalized drag (F_D'). The change in system mass is given by $m' = m_{BC} / m_{initial}$ with mass m being the sum of densities of all fluid nodes, $m = \sum_{i=\text{fluid}} \rho_i$. The subscript BC denote the final condition and "initial" denote the initial condition of the tested boundary scheme. The simulations are run for 130000 and 150000 timesteps for $Re = 150$ and 330 respectively. The normalized flow rate is given by $Q' = Q_{BC} / Q_{MGBB}$ with $Q = \int_0^H U_x \, dy$ at the outlet of the channel. The normalized force is given by $F' = F_{BC} / F_{MGBB}$. Here, the subscripts BC and MGBB denote the tested boundary condition and the mid-grid bounceback respectively. The m', Q' and F_D' for different schemes are shown in figures 2.4, 2.5 and 2.6 respectively. It can be observed that the mass-leakage is dependent on the Re on comparing figures 2.4(a) and (b) and increases for increasing Re.

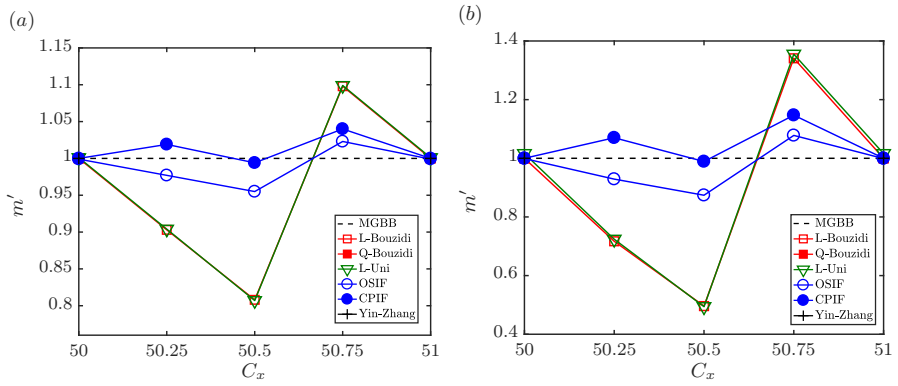The MGBB scheme is perfectly mass conserving and therefore serves as ref-

Figure 2.4: Change in system mass (m') for different obstacle positions (C_x), for (*a*) $Re = 150$ (steady flow) and (*b*) $Re = 330$ (unsteady flow). It should be noted that the scales are different for different Re. The data for Q-Bouzidi and Yin-Zhang schemes are available only for $C_x = 50$ and $C_x = 51$.
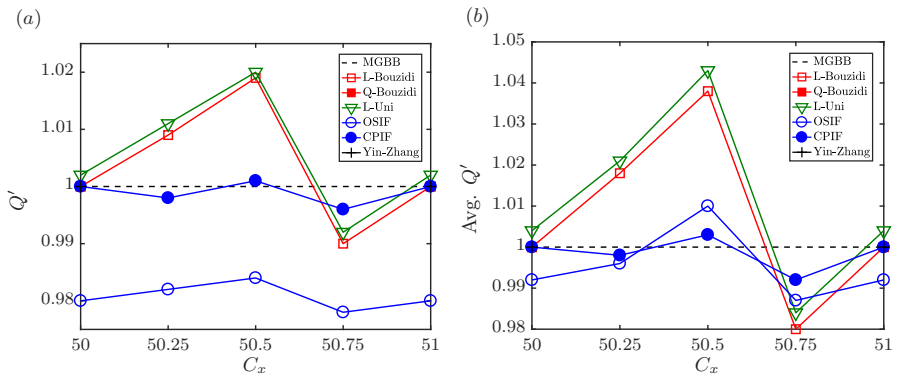

Figure 2.5: Normalized flow rate (Q') for different obstacle positions (C_x), for (*a*) $Re = 150$ (steady flow) and (*b*) $Re = 330$ (unsteady flow).
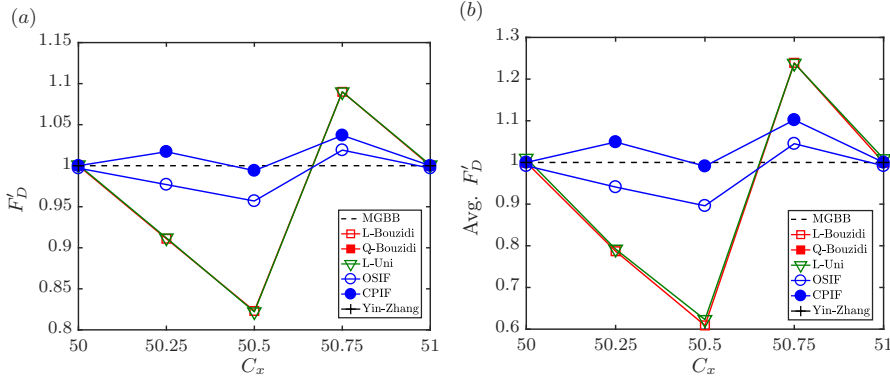
Figure 2.6: Normalized drag (F'_D) for different obstacle positions (C_x), for (*a*) $Re =$ 150 (steady flow) and (*b*) $Re = 330$ (unsteady flow).

erence in figures 2.4, 2.5, and 2.6. The linear Bouzidi scheme recovers perfectly mass conserving MGBB scheme, if the walls are exactly half-way. The walls are exactly half-way (i.e. $q = 0.5$) on all sides for square obstacle at $C_x = 50$ and 51. In figure 2.4(*b*), this is confirmed. The same perfect conservation at $C_x = 50$ and 51 was also observed for quadratic Bouzidi scheme. However, the quadratic scheme requires a much finer grid and higher viscosity (or lower grid Re) for arbitrary wall positions and is therefore not stable for C_x other than $C_x = 50$ and 51.

It has to be noted that the linear unified scheme (L-Uni) does not recover MGBB, even for $q = 0.5$ as in Bouzidi scheme. The same can be verified in figure 2.4(*b*) that there is a minor mass leakage even at $C_x = 50$ and 51. This is more apparent from the deviation of the normalized flow rate (Q') in figure 2.5(*b*). The quadratic unified scheme (Kao & Yang, 2008) failed for all the test cases. However, the scheme performed stable on a finer grid with higher viscosity to simulate same flow Re.

Also, the Yin-Zhang boundary condition with velocity inter/extrapolation was unstable for all positions except for $Cx = 50$ and 51, where it recovers the mid-grid bounceback condition. The low viscosity, needed to reach high Re at reasonable grid size, exposed the instability of different boundary conditions, especially the quadratic schemes and also the Yin-Zhang boundary condition, which were found only stable for higher relaxation times (for $\tau = 0.6$) and a finer grid. This implies that for high Re flows, the application of such boundaries is limited. More precisely, to simulate a specific flow Re, such schemes require a finer grid with higher τ (or low grid Re) than the other stable schemes.

It could be observed that the OSIF and the CPIF schemes perform better than all other schemes. Overall, CPIF performs best due to its composite design to

recover both mid-grid and onsite bounceback schemes. However, it should be noted that for other intermediate positions, such as $C_x = 50.25$ and $C_x = 50.75$, there is still a mass-leakage for CPIF. The highest mass-leakage of around 15% is observed at $C_x = 50.75$ for $Re = 330$ (see figure 2.4(b)). At $C_x = 50.5$, q becomes zero for the right wall of the square. Therefore, we use $C_x = 50.49$ for OSIF and CPIF as their working range is for $0 < q \leq 1$. For the same reason, there is a minor leakage observed for CPIF for both Re at $C_x = 50.5$.

The mass-leakage phenomenon would be acceptable provided that the flow field and force experienced by the object are not affected strongly. In reality, both the flow field and the force experienced by the object could be correlated with the mass-leakage. Further, if the simulations are run for a longer duration, the mass-leakage increasingly affects the simulation results. The linear Bouzidi scheme, which leaks upto 50% by the end of simulation at $C_x = 50.5$ (see figure 2.4(b)), shows a corresponding Q' of 4% (see figure 2.5(b)). Similarly, the corresponding F'_D deviates up to 40%, as can be observed from figure 2.6(b). Even the best performing CPIF scheme shows upto a deviation of 1% for Q' and 10% deviation for F'_D. Therefore, it can be concluded that none of the available schemes is perfectly mass conserving.

2.5.2. FORCED MASS CONSERVATION SCHEMES AND CONSTANT DENSITY SCHEME

To solve the mass-leakage, one can enforce mass conservation by explicitly adding or removing mass from the system. There are several ways to explicitly conserve the mass and at the same time conserve local momentum. The following first four cases conserve both mass and momentum. The last proposed case is slightly different and does not enforce mass conservation. Due to its simplicity, we test these corrections on the popularly used linear Bouzidi scheme. However, it should be observed that these concepts are general and can be applied on any curved boundary scheme.

Case 1: Adding the *local* change in mass per timestep ($\delta\rho$), only to the rest distribution of the particular fluid node: $f_0 = f_0 + \delta\rho$.

Case 2: Adding the *local* change in mass per timestep, to the distributions of the particular fluid node, multiplied by the corresponding weights: $f_\alpha = f_\alpha + w_\alpha\delta\rho$.

Case 3: Computing the *global* change in mass per timestep and evenly adding it to the rest distribution of all fluid nodes: $f_0 = f_0 + \sum \delta\rho/N_f$, where N_f is the total number of fluid nodes, and
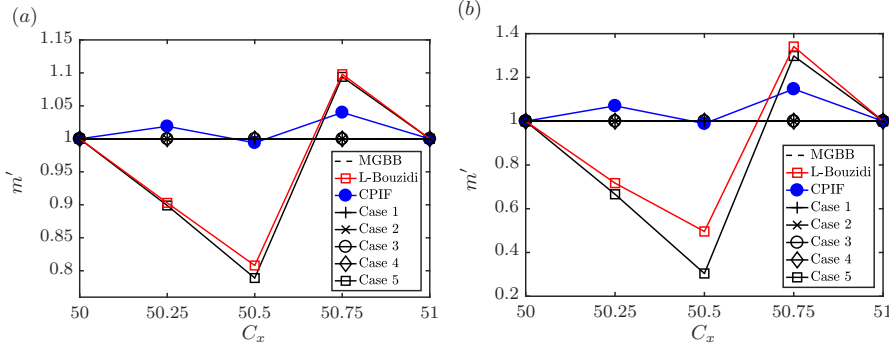
Figure 2.7: Change in system mass (m') for different obstacle positions (C_x), for (a) $Re = 150$ (steady flow) and (b) $Re = 330$ (unsteady flow).

Case 4: Computing the *global* change in mass per timestep and adding it to the distributions proportional to the weights: $f_\alpha = f_\alpha + w_\alpha \sum \delta\rho / N_f$. It should be noted that for cases 2 and 4, the density corrections are applied after the force measurements. Otherwise, the modified distributions would corrupt the actual force experienced by the particle. This implies that an additional variable needs to be introduced to save the leakage amount for individual fluid nodes. Therefore from an implementation point-of-view, cases 1 and 3 are simpler to implement.

Case 5: Additionally, we discuss a special case, denoted as case 5, based on the constant density approach (He & Luo, 1997), where the f_{eq} is given by

$$f_\alpha^{eq} = w_\alpha \left(\rho + \rho_0 \left[\frac{(\boldsymbol{e}_\alpha \cdot \boldsymbol{u})}{c_s^2} + \frac{(\boldsymbol{e}_\alpha \cdot \boldsymbol{u})^2}{2c_s^4} - \frac{(\boldsymbol{u} \cdot \boldsymbol{u})}{2c_s^2} \right] \right). \tag{2.33}$$

Here, ρ_0 is the constant density (equal to the initial density) and the momentum defined as $\rho_0 \boldsymbol{u} = \sum_\alpha f_\alpha \boldsymbol{e}_\alpha$. Further, the forcing term also involves a constant density term: $S_\alpha = -3w_\alpha \rho_0 (\boldsymbol{g} \cdot \boldsymbol{e}_\alpha)$ in equation 2.1. It should be noted that ρ_0 is used here instead of ρ earlier. Therefore, the fluid is driven with constant force instead of constant gravity otherwise. As can be seen, this scheme is different from the other four cases, because it does not enforce mass conservation. This means that the system mass m, defined as $\sum \rho$, is actually changing with time. However, as the essential parts of the scheme are based on the constant density ρ_0 instead of the actual density $\rho = \sum_\alpha f_\alpha$, the flow field and the forces experienced by the particle are not influenced by the mass-leakage.
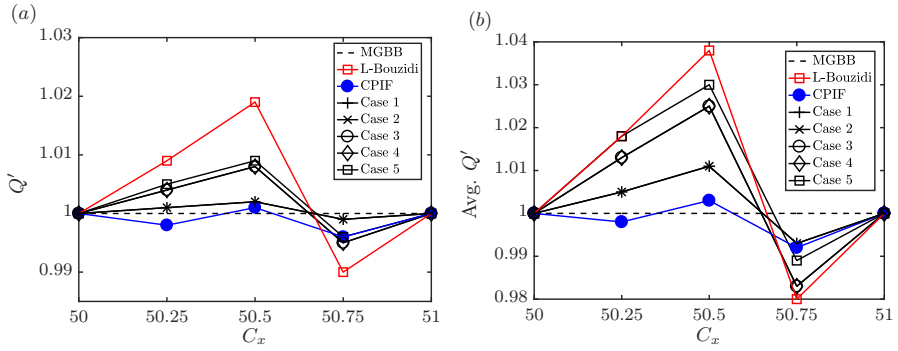
Figure 2.8: Normalized flow rate (Q') for different obstacle positions (C_x), for (a) $Re = 150$ (steady flow) and (b) $Re = 330$ (unsteady flow).
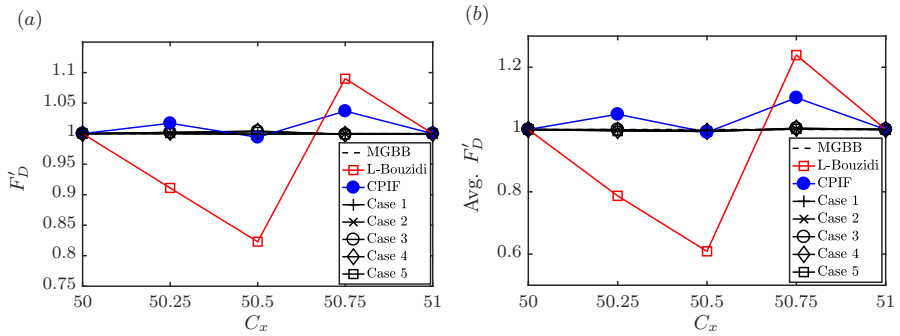

Figure 2.9: Normalized drag (F_D') for different obstacle positions (C_x), for (a) $Re = 150$ (steady flow) and (b) $Re = 330$ (unsteady flow).

All the four strict mass conservation schemes are originally conceived by us. However, we later found some literatures have applied such corrections, albeit only in a specific form, only case 1, i.e., adding the local mass leakage to the rest node (Yin *et al.*, 2012). Only in this study, we study different combinations of mass correction and their effects on flow field in a detailed manner and thereby making useful suggestions to the LBM community.

Each of the above mentioned cases is unique and will have its own implication to the flow field. Next, we apply these cases to the previous testcase and observe their performance. The performances are compared with the linear Bouzidi scheme without correction and also with the best performing CPIF scheme. The m' for different cases are given in figure 2.7. Due to their perfectly conserving nature, there is no deviation in system mass m' for cases 1-4, as can be seen from both figures 2.7(*a*) and (*b*). Case 5 shows slightly higher mass-leakage than the original linear Bouzidi scheme as it is not a mass conservation enforcing scheme.

The Q' for the different cases are given in figure 2.8. In terms of flow fields, we observe that both case 1 and 2 have similar performance, both performing better than the CPIF scheme for the steady flow, as can be seen in figure 2.8(*a*). For unsteady flows, again a similar performance from cases 1 and 2 with a comparable performance of CPIF, but slightly poorer only at $C_x = 50.5$. This is because the Bouzidi scheme does not recover onsite bounceback, which occurs for $C_x = 50.5$ for the front and rear sides of the obstacle. The cases 3-5 perform almost similar with slightly higher deviations shown by case 5. Importantly, it should be noted that all cases perform better than the original Bouzidi scheme. Therefore, we recommend the use of any explicit mass conserving scheme, specifically cases 1 and 2, which offer superior performance among the investigated cases.

For F'_D, it can be observed that all cases perform identical and show far superior performance over the CPIF scheme itself, as seen in figures 2.9(*a*) and (*b*). Similarly from Q', we conclude that the explicit mass conservation as in cases 1-4 and constant density approach of case 5 provide better accuracy than the existing schemes without explicit mass conservation. Even though case 5 shows significant mass-leakage, the case performs better in terms of computing the true velocity field as observed from Q' and also in terms of force experienced by the obstacle as in F'_D compared to conventional linear Bouzidi scheme.

Next, we analyse the flow field in detail for steady flow occurring at $Re = 150$. The horizontal velocity component (U_x) is measured along the centerline of the domain. Here, we consider the worst performing condition of the linear Bouzidi scheme, which occurs at $C_x = 50.5$. Then, we apply the proposed methods and compare their performance. The U_x for the different cases are plotted in figure 2.10. The results are compared with the true solution obtained from the midgrid
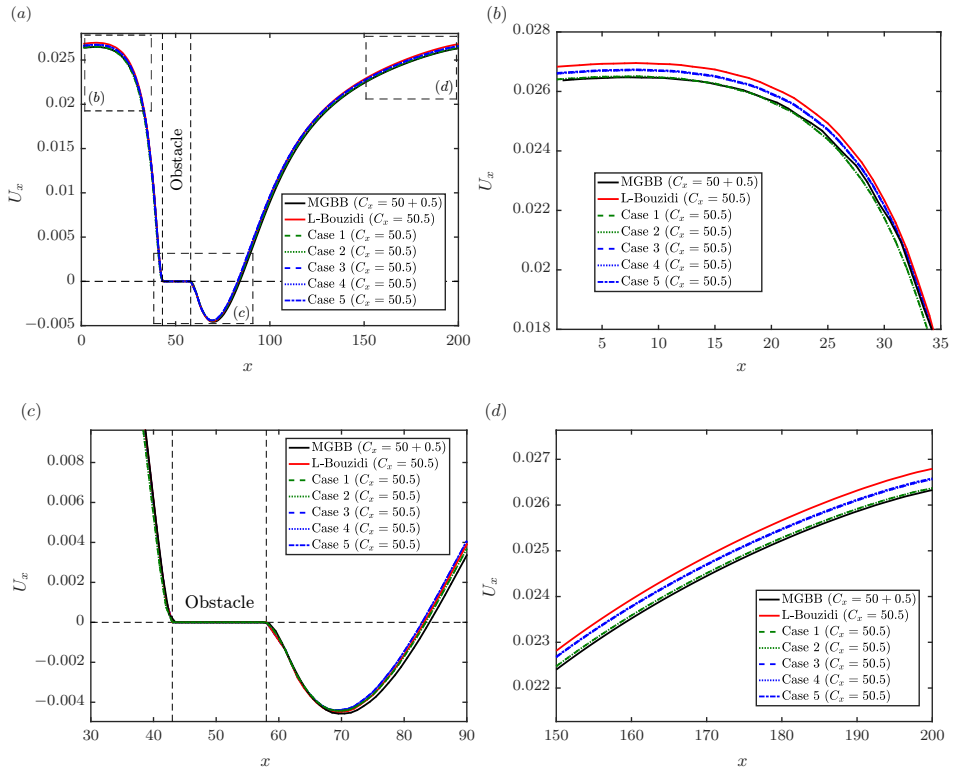
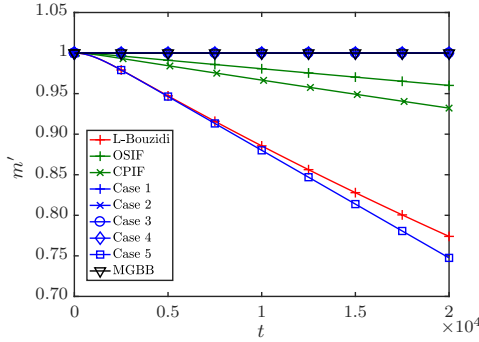Figure 2.10: Distribution of horizontal velocity component U_x for different schemes.

Figure 2.11: The normalized system mass (m') of different schemes for the inclined channel flow over time.

bounceback (MGBB) scheme. To maintain consistency, the MGBB results are shifted by 0.5 along the x-direction. From the results, it can be observed that there is a large deviation of the linear Bouzidi solution from the MGBB solution. However on applying the methods proposed, it is observed that the resulting flow field is closer to the true solution (of the MGBB). As mentioned earlier, cases 1 and 2 perform identical and are closest to the solution obtained from MGBB, which is evident from the zoomed figures 2.10(*b*), (*c*) and (*d*). Likewise, cases 3, 4 and 5 perform identical and are slightly away from the MGBB solution, but still better than the linear Bouzidi solution without any correction.

The characteristic of the current testcase is that the walls are flat and are perfectly aligned to the grid. This implies, for a particular wall, the interpolation distances q_α are the same for all wall-intersecting directions. Further, the testcase replicates flow conditions with strong pressure gradients, and therefore strong density gradients, in the stagnation flow in front of the square object.

2.5.3. FLOW THROUGH AN INCLINED CHANNEL

In this section, we simulate a pure shear flow through a periodic channel driven by gravity. To include effects of different interpolation distances q_α, we simulate the flow in an inclined channel. With this simulation, we investigate the effects of mass-leakage on pure shear flows. The channel width is 7 lattice units and the channel has an inclination of 3/5. The simulation parameters are $\tau = 0.52$ and $g = 10^{-4}$. The change in system mass after 20000 timesteps for different schemes is plotted in figure 2.11 and the resulting flow profile for different schemes is plotted in figure 2.12. The flow velocities are normalized against the maximum velocity obtained from the theory.
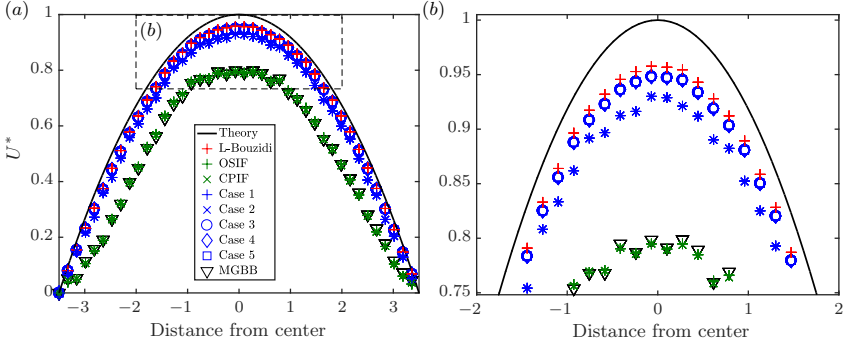
Figure 2.12: The normalized tangential velocity (U^*) of the flow inside a straight channel with an inclination of 3/5. (b) is a zoom-in of the full velocity profile shown in (a).

Regarding the performance of different schemes, the quadratic schemes perform better than linear schemes, even though τ is low. The results are not shown here for brevity and interested reader can refer to figure 2 of Bouzidi *et al.* (2001). Therefore, it can be inferred that the quadratic schemes are stable, even with low τ, for flows with no density gradient, as in the pure shear flow in this testcase. However, due to poor stability in flows with density gradients, as seen from previous testcase, these schemes are not considered for further comparison.

The different schemes achieve steady velocity profiles even after the steady leaking of the mass. Among the schemes shown, the linear Bouzidi scheme showed best performance. The performances of both the OSIF and CPIF schemes are poor and are comparable to that of the staircase approximation of the midgrid scheme. The reason why the interpolation free schemes perform poor could be due to different q_α values for a boundary fluid node for different directions. In the previous testcase, the q_α values are identical for all intersecting velocity directions for a particular side. The interpolation free schemes are based on varying the viscosity depending on the q_α. Therefore having different q_α for different velocity directions within a fluid node implies using different viscosities for a single fluid node. These simultaneous effects can affect the performance of the schemes.

Among the 5 cases proposed, cases 1 and 2 performed slightly poor than other correction cases. The reason why such cases perform poorly is due to the fact the mass corrections are applied locally at the boundary. The complete or significant part of the correction goes to the rest distribution f_0 and therefore could slightly increase the pressure locally, resulting in slight pressure fluctuations on the boundary. The cases 3, 4 and 5 perform identical and only slightly
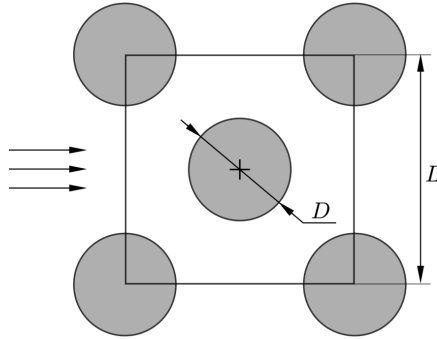
Figure 2.13: The staggered cylinder configuration: The domain is periodic and the flow is driven by gravity.

poorer than the linear Bouzidi scheme. This is contrary to the previous testcase, where all the cases performed better than the default linear Bouzidi scheme. However, it should be noted that many practical LBM simulations involve both shear and pressure effects. Therefore, we next select a testcase which involves both shear and stagnation pressure effects.

2.5.4. FLOW AROUND STAGGERED CIRCULAR CYLINDERS

In order to emulate a general particulate system or a porous medium, we simulate here periodic flow around staggered circular cylinders. Inline cylinders are avoided as it would result in flow channelling at higher Re and thereby purely dominated by shear effects alone. The staggered configuration considered here provides a good mix of stagnation and shear effects. The flow setup is shown in figure 2.13. The solids-volume fraction ϵ_s is 0.3 and the cylinder diameter D is chosen appropriately, depending on the domain size.

Since there is no analytic solution available for such a flow problem, a highly accurate solution is obtained with $D = 131.1$ in a 300×300 domain with the mid-grid bounce back scheme. The simulation has been performed for $Re = 40$ with $Re = U_0 D / \nu$. The flow is steady for this flow configuration. Here, $U_0 = (1 - \epsilon_s) U_{av}$ is the superficial fluid velocity with U_{av} the average velocity in the fluid domain. Since the flow is driven by gravity and the velocity field evolves accordingly, a feedback loop is used to control the gravity to achieve the desired U_0 precisely. The resulting velocity field is shown in figure 2.14. The drag coefficient is computed as $C_D = F_D / (1/2 \rho D U_0^2)$ where F_D is the drag acting on a single cylinder. A value of $C_D = 5.93$ is obtained for the highly refined grid.

Next, we simulate a domain of size 30×30 with the different boundary condi-
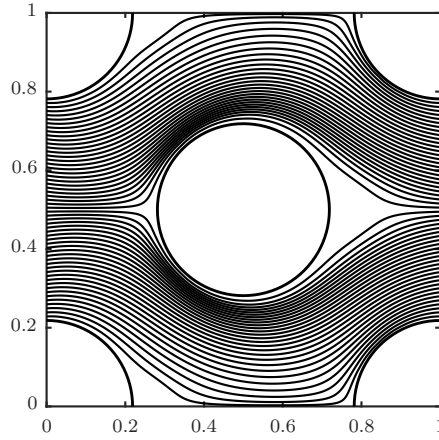
Figure 2.14: The accurate velocity field for $Re = 40$ obtained using the midgrid bounceback scheme with very high grid resolution.
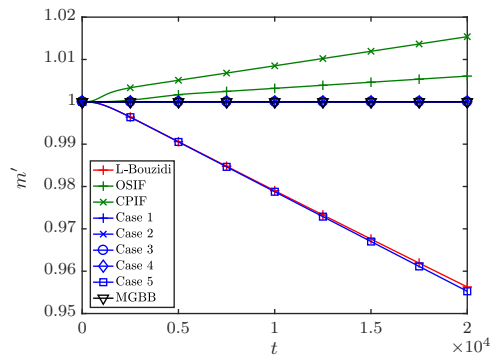

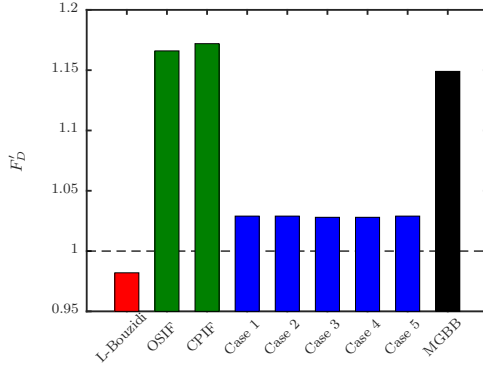Figure 2.15: The normalized system mass (m') of different schemes for the periodic flow around staggered cylinders.

Figure 2.16: The normalized drag (F'_D) of different schemes for the periodic flow around staggered cylinders. It should be noted that F'_D of L-Bouzidi scheme, though appears closest to 1, is time dependent. This implies a longer simulation would result in F'_D further away from 1. Only the results of cases 1-5 and MGBB are time independent.

tions, for the same Re, for 20000 timesteps. Based on the accurate C_D computed before, the true drag ($F_{D,true}$) for the new resolution is computed. We measure the F_D for the different boundary schemes from the simulations and compare with the $F_{D,true}$ as $F'_D = F_D/F_{D,true}$. The evolution of mass-leakage is plotted in figure 2.15. The normalized drag F'_D is plotted in figure 2.16. It should be noted that the first three schemes in figure 2.16, the Bouzidi and interpolation free schemes, have drag dependent on the average density of the system. This implies that they are dependent on the simulation duration and exhibit different drag for a longer simulation. In other words, though the linear Bouzidi scheme exhibits F'_D closest to 1, it should be noted that a longer simulation would imply a different F'_D with larger deviation due to mass-leakage. For the cases 1 to 5, the force observed is independent of time, including case 5 which exhibits mass-leakage. Further, it can be observed that the proposed correction cases perform better than the midgrid bounceback, which experiences higher drag on the particle due to the staircase approximation of the geometry. Overall, the cases 3 and 4 performed slightly better ($F'_D = 1.028$), than all other cases ($F'_D = 1.029$).

2.6. RECOMMENDATIONS FOR PRACTICAL USE

Among the 5 correction schemes proposed, we observed that cases 1 and 2 (enforcing local mass conservation) performed relatively better for flows with large stagnation effects. However, we also found that their performance is slightly

poorer in case of pure shear flows. This could be attributed to the fact that they are local correction schemes, which introduce local pressure differences on the boundaries. On the other hand, global correction schemes such as cases 3 and 4 perform relatively better in case of pure shear flows and also for flow around staggered cylinders. Therefore, global correction schemes (cases 3 and 4) are recommended if mass conservation is a desired property for the system. Furthermore, case 3 is easier to implement than 4. Mass corrections need to be performed after the force measurement for case 4 as the non-rest distributions are modified for case 4. Therefore, we can conclude that case 3, globally correcting the mass by distributing the correction over all fluid node rest distributions, would be the best choice among the different correction schemes proposed.

2.7. CONCLUSION

We tested different curved no-slip boundary conditions for LBM available in the literature with a focus on mass-leakage at high *Re*. Several testcases were proposed, such as periodic flow around a square cylinder, periodic inclined channel flow, and periodic flow around staggered cylinders. The performance of different schemes were tested based on the mass-leakage, flow velocity and the resulting force exerted by the fluid flow. The results were also compared to analytical solutions, where available.

Generally for flows exhibiting strong pressure gradients, we observed that quadratic schemes are unstable at low viscosities. However for pure shear flows, they are relatively stable and achieve better performance compared to linear schemes. Overall, the linear schemes performed better in terms of stability. We also observed that the variable viscosity interpolation-free schemes such as the OSIF and CPIF were stable for different flows. However, their performance was poor in terms of accuracy for curved boundaries or boundaries with different q_α as in inclined channel flow. The Yin-Zhang scheme has been found to be unstable for flows with high pressure gradients and is therefore not recommended on the basis of stability. For stable cases, the Yin-Zhang scheme did not yield better performance than the linear Bouzidi scheme.

Apart from different existing boundary conditions, we have also tested 4 different cases where mass conservation was explicitly enforced and one constant density case, applied on the linear Bouzidi scheme. For flows with large stagnation effects, we observed that enforcing local mass conservation performed slightly better than global correction schemes. However for pure shear flows, the global correction schemes performed much better than local schemes. In a general flow problem with combined shear and stagnation effects, we observe that global correction schemes perform better than local correction schemes. Over-

all, we recommend case 3 type correction (global correction of the fluid node rest distributions) considering the ease of implementation.

3

SCALING LAWS FOR DRAG AND LIFT OF NON-SPHERICAL PARTICLES

The flow around different prolate (needle-like) and oblate (disc-like) spheroids is studied using a multi-relaxation-time lattice Boltzmann method. We compute the mean drag coefficient $C_{D,\phi}$ at different incident angles ϕ for a wide range of Reynolds numbers (Re). We show that the sine-squared drag law $C_{D,\phi} = C_{D,\phi=0°} + (C_{D,\phi=90°} - C_{D,\phi=0°}) \sin^2 \phi$ holds up to large Reynolds numbers Re = 2000. Further, we explore the physical origin behind the sine-squared law, and reveal that surprisingly, this does not occur due to linearity of flow fields. Instead, it occurs due to an interesting pattern of pressure distribution contributing to the drag at higher Re for different incident angles. The present results demonstrate that it is possible to perform just two simulations at $\phi = 0°$ and $\phi = 90°$ for a given Re and obtain particle shape specific C_D at arbitrary incident angles. However, the model has limited applicability to flatter oblate spheroids, which do not exhibit the sine-squared interpolation, even for Re = 100, due to stronger wake-induced drag. Regarding lift coefficients, we find that the equivalent theoretical equation can provide a decent approximation, even at high Re, for prolate spheroids.

3.1. INTRODUCTION

Industrial applications and real life cases often involve suspensions of non-spherical particles, of either regular or irregular shapes. Prolate (needle-like) spheroids can be used to describe milled biomass particles, fibrous suspensions, and submarine hulls. On the other hand, oblate (disc-like) particles can be approximated to represent red blood cells. El Khoury *et al.* (2010, 2012) performed direct numerical simulations (DNS) with the flow perpendicular to the spheroid's symmetry axis and investigated the wakes behind a prolate spheroid of ratio 6:1. Hölzer & Sommerfeld (2009) and Zastawny *et al.* (2012) investigated different non-spherical particles at different flow incident angles at different Re, albeit limiting mainly to the steady flow regime. Very recently, Ouchene *et al.* (2016) proposed force correlations for prolate spheroids upto aspect ratio of 32, again limited to steady flows with $Re \leq 240$. They report an interesting finding that the drag coefficient C_D of the prolate spheroids follows a sine-squared interpolation between its extreme C_D values for $Re \leq 240$ for the reported aspect ratios. In this chapter, we investigate this phenomenon more deeply and to higher Re.

Some authors define the Reynolds number Re_d based on the minimum thickness of the particle d_{min}. For this work, the Reynolds number is defined as $Re = |\boldsymbol{u}_\infty| d_{eq} / \nu$, where $\boldsymbol{u}_\infty$ is the uniform inlet velocity, ν is the kinematic viscosity of the fluid, and d_{eq} is the diameter of the volume-equivalent sphere given by $d_{eq} = (6V_p/\pi)^{1/3}$ with V_p being the particle volume. The drag coefficient is defined as $C_D = |\boldsymbol{F}_D|/(\frac{1}{2}\rho|\boldsymbol{u}_\infty|^2 \frac{\pi}{4} d_{eq}^2)$. Here, $\boldsymbol{F}_D$ is the drag force acting on the particle and ρ is the fluid density. Similarly, we define the lift coefficient as $C_L = |\boldsymbol{F}_L|/(\frac{1}{2}\rho|\boldsymbol{u}_\infty|^2 \frac{\pi}{4} d_{eq}^2)$ with F_L being the measured lift force. For any particle in the Stokes regime (Happel & Brenner, 1983), based on linearity of the Stokes equations, the drag coefficient at different incident angles ϕ interpolates as

$$C_{D,\phi} = C_{D,\phi=0°} + (C_{D,\phi=90°} - C_{D,\phi=0°})\sin^2\phi. \qquad (3.1)$$

Here, the subscript ϕ implies the value at that particular incident angle ϕ. The proof of equation 3.1 is given in appendix A. It should be noted that C_D measured at different ϕ in equation 3.1 pertain to the same Re definition with $Re = |\boldsymbol{u}_\infty| d_{eq}/\nu$.

To motivate the reader, the drag on different spheroids is tested upto $Re = 2000$ and the mean C_D are plotted in figure 3.1. Surprisingly, the investigated particles follow sine-squared interpolation very well for both steady and unsteady regimes, even for Re as high as 2000. This interesting phenomenon appears to be similar to the Stokes regime prediction (equation 3.1) as mentioned by Ouchene *et al.* (2016). We investigated the phenomenon in detail and found a plausible reason and also the limitations of the sine-squared behaviour. Our findings
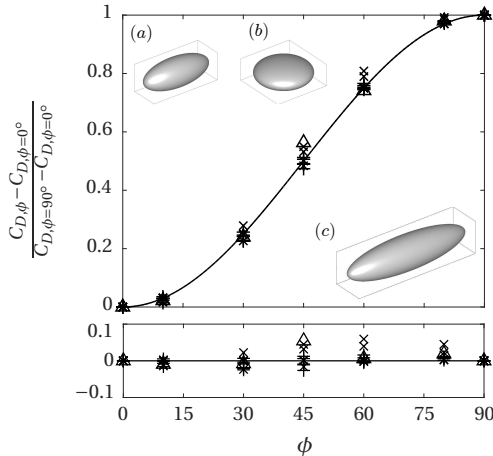
Figure 3.1: Top: The normalized drag coefficient $\frac{C_{D,\phi} - C_{D,\phi=0°}}{C_{D,\phi=90°} - C_{D,\phi=0°}}$ plotted against incident angle ϕ. The solid line indicates $\sin^2 \phi$. Data include (a) prolate spheroid (+) and (b) oblate spheroid (×), both of aspect ratio 5/2, both for Re=0.1, 10, 100, 1000 and 2000, (c) prolate spheroid of aspect ratio 4 ($\triangle$) for Re=2000. Averaged C_D values are used for cases with vortex shedding occurring at high Re. Bottom: Difference between normalized drag coefficient and $\sin^2 \phi$.

at high Re, in combination with observations of Ouchene *et al.* (2016) for prolate spheroids upto aspect ratio 32, extends the validity of the drag law to both high aspect ratio prolate spheroids and high Re. This implies that in many situations, the mean drag coefficient at any incident angle $C_{D,\phi}$ for a given Re can be obtained by just knowing two values: $C_{D,\phi=0°}$ and $C_{D,\phi=90°}$.

3.2. SIMULATION SETUP

The fluid flow is simulated using a D3Q19, multi-relaxation time (MRT) lattice Boltzmann method as discussed in chapter 2. Uniform velocity in the z-direction is prescribed at the inlet boundary based on Hecht & Harting (2010). The side walls are prescribed with free-slip boundaries rather than periodic boundary conditions, which could cause the flow to deflect either up or down based on inclination of the non-spherical particle (Hölzer & Sommerfeld, 2009). The downstream (outlet) is specified with axial-stress-free boundary condition with $\partial u_z / \partial z = 0$ (Aidun *et al.*, 1998). We use the linearly interpolated bounce back scheme (Bouzidi *et al.*, 2001; Lallemand & Luo, 2003) to accurately consider the curved geometry of the particle. The improvement in solution accuracy is neg-
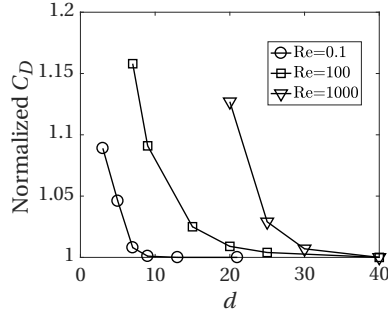
Figure 3.2: For a sphere, the normalized C_D as a function of diameter d in lattice cells for different Re, showing convergence of the method. The normalization is done with respect to the highest resolution C_D.

ligible between linear and quadratic interpolation schemes, provided sufficient resolution is used (Pan *et al.* (2006); Kruggel-Emden *et al.* (2016)). Detailed information about the simulation domain and their sizes are elaborated in sections 4.2.2 and 4.2.3 respectively.

3.2.1. INFLUENCE OF GRID RESOLUTION

The influence of the grid resolution is tested with the flow around an isolated sphere. The normalized C_D is plotted in figure 3.2. Three different regimes are tested (i) Stokes flow, (ii) intermediate Reynolds number at $Re = 100$ with a steady wake, and (iii) high Reynolds number $Re = 1000$ exhibiting a complex, unsteady wake and therefore the *mean* drag coefficient is shown. The influence of the resolution is stronger with increasing Re as seen in figure 3.2. For $Re = 1000$, the observed C_D at resolution $d_{eq} = 40$ is 0.456 and is in good agreement with literature results: $C_D = 0.464$ from Vakarelski *et al.* (2016) and $C_D = 0.48$ from Ploumhans *et al.* (2002). This resolution information is considered in maintaining the minimum thickness d_{min} of our non-spherical particles at different Re. Due to the non-sphericity, the other dimension is always larger than the minimum thickness and therefore a good particle resolution is ensured.

3.3. TEST OF LINEARITY FOR PRESSURE AND VELOCITY FIELDS

The drag law for Stokes flow (equation 3.1) for non-spherical particles is based on the linearity of the Stokes equations in the creeping flow limit. As figure 3.1 shows, we observe that the mean C_D follows the same sine-squared behaviour even in regimes with a complex unsteady wake at Re as high as 2000. It has
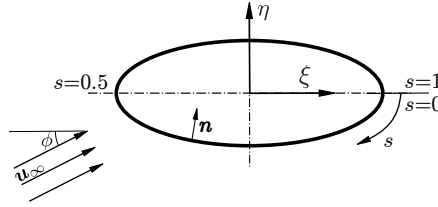
Figure 3.3: The local coordinate system (ξ, η) of the ellipsoidal section. s is the normalized distance along the circumference. $\boldsymbol{n}$ is the inward facing, local unit normal vector. The simulations are performed in a rectangular domain with particle rotated for different incident angles. For clarity and consistency, the results are analysed in the local coordinate system of the section (ξ, η).

to be noted that all the investigated geometries are axi-symmetric, smooth and rounded. Though non-linear effects dominate at higher Re, we first investigate if the inherent smooth nature of the geometries results in cancellation of non-linearity effects in the region close to the particle surface. In other words, we test whether the velocity and pressure fields for an arbitrary particle at incident angle ϕ obey the following conditions sufficiently close to the surface:

$$\boldsymbol{u}_\phi = \boldsymbol{u}_{\phi=0°} \cos \phi + \boldsymbol{u}_{\phi=90°} \sin \phi, \tag{3.2}$$

$$p_\phi - p_\infty = (p_{\phi=0°} - p_\infty) \cos \phi + (p_{\phi=90°} - p_\infty) \sin \phi. \tag{3.3}$$

Here, $\boldsymbol{u}_\phi$ is the velocity field and p_ϕ is the pressure field around the particle, based on the incoming flow $\boldsymbol{u}_\infty$ oriented at angle ϕ, as shown in figure 3.3. The proof of equations 3.2 and 3.3 are given in appendix B. If equations 3.2 and 3.3 are true, the corresponding drag components, i.e. the viscous drag $C_{Dv,\phi}$ and the pressure drag $C_{Dp,\phi}$, also follow the sine-squared law.

Throughout this chapter, from the *three-dimensional* simulations, the flow fields are analysed along the meridional plane. The meridional plane contains the axis of symmetry of the particle at different incident angles and the inflow velocity vector $\boldsymbol{u}_\infty$. Of the different particles tested, we consider the prolate spheroid of aspect ratio 5/2 for the linearity study. A special case of $\phi = 30°$ is tested along the meridional plane. The velocity and pressure fields from the theoretical linear combination in equations 3.2 and 3.3 are compared with the actual flow field from the simulations. Two cases, one for the Stokes flow at $Re = 0.1$ and another exhibiting steady flow, yet sufficiently large Re compared to the Stokes regime, $Re = 100$, are considered. The velocity fields based on the theory and the actual flow are given in figure 3.4. For Stokes flow, the linear superposition of velocity fields result in attached flow around the particle. There is a good match between the theoretical and actual fields with deviations upto 2%. At $Re = 100$,
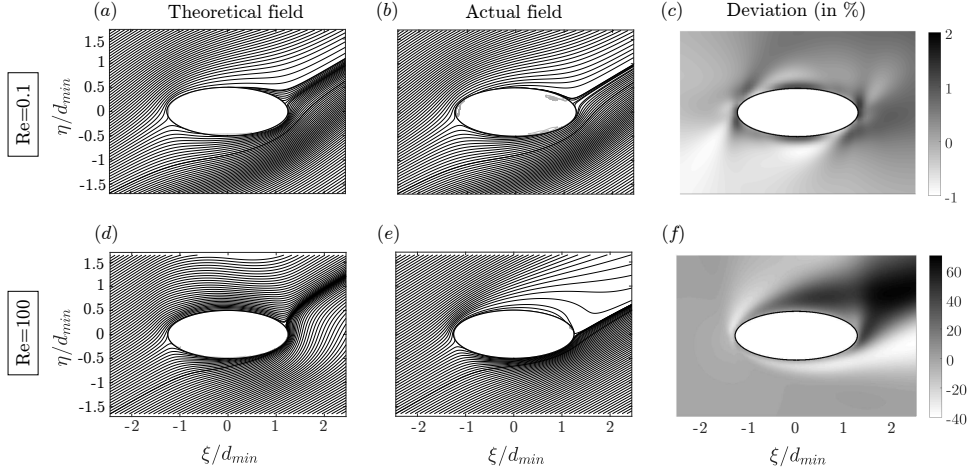
Figure 3.4: The theoretical and actual velocity fields and the deviation between these fields for $Re = 0.1$ (a, b, c) and $Re = 100$ (d, e, f), respectively. The deviation is computed as $\frac{\|\boldsymbol{u}_{th} - \boldsymbol{u}_{act}\|}{\|\boldsymbol{u}_\infty\|}$ in %. Note the deviation scales are different for different Re.

the flow field exhibits attached flow for $\phi = 0°$ due to streamlining and a strong recirculation for $\phi = 90°$. In figure 3.4(d), the linear combination of them for $\phi = 30°$ still appears attached, whereas the actual flow field as shown in figure 3.4(e) exhibits recirculation in the wake of the particle. There is a strong mismatch between the fields, as shown in figure 3.4(f) with deviations upto 60%.

At the same time, it is interesting to note that the viscous drag force resulting from the velocity field becomes increasingly independent of incident angle ϕ at higher Re. Figure 3.5 shows the viscous and pressure drag components (and similarly figure 3.6 for lift components) at Re=0.1, 10 and 100 for the prolate
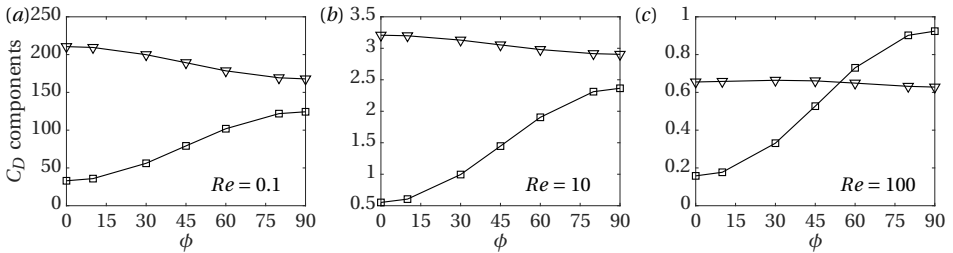

Figure 3.5: ($\triangledown$) Viscous and ($\square$) pressure components of the drag coefficient for a prolate spheroid of aspect ratio 5/2 at (a) $Re = 0.1$, (b) $Re = 10$, and (c) $Re = 100$.

Figure 3.6: ($\triangledown$) Viscous and ($\square$) pressure components of the lift coefficient for a prolate spheroid of aspect ratio 5/2 at (*a*) $Re = 0.1$, (*b*) $Re = 10$, and (*c*) $Re = 100$.
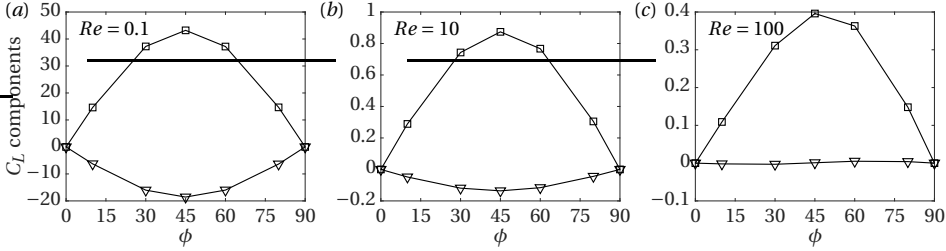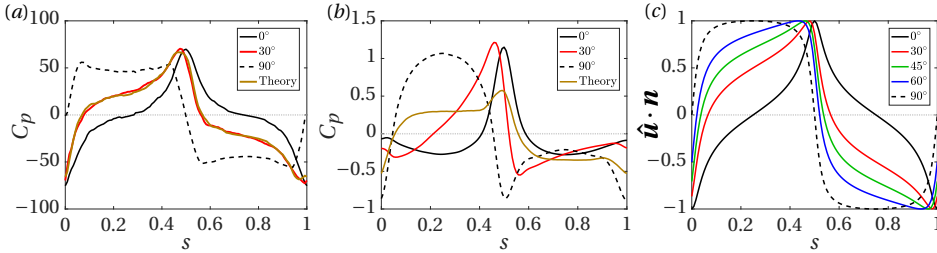

Figure 3.7: Distribution of C_p against normalized distance s along the circumference of the meridional section for (*a*) $Re = 0.1$ and (*b*) $Re = 100$; (*c*) surface normal projections $\hat{\boldsymbol{u}} \cdot \boldsymbol{n}$ for different incident angles ϕ. Note the linearity theory (at $\phi = 30°$) matches perfectly with simulations (at $\phi = 30°$) for $Re = 0.1$ and shows strong mismatch for $Re = 100$. For the different ϕ shown, note the matching trends of C_p at $Re = 0.1$ with $\hat{\boldsymbol{u}} \cdot \boldsymbol{n}$.

spheroid of aspect ratio 5/2. Indeed, it is observed that the viscous effects become weakly dependent on incident angle ϕ at $Re = 10$. Eventually at $Re = 100$, the viscous drag becomes independent of ϕ compared to change in the pressure drag, with $C_{Dv,\phi} \approx C_{Dv,\phi=0°} \approx C_{Dv,\phi=90°}$. This implies that the dependence of the drag on the particle's incident angle ϕ, at higher Re, is purely coupled to the ϕ-dependence of the pressure drag. Therefore, we next focus on the pressure coefficient on the surface of the meridional plane section.

The pressure coefficient is defined as $C_p = (p - p_\infty)/(1/2\rho|\boldsymbol{u}_\infty|^2)$ with pressure p measured on the surface and p_∞ the pressure at the far field. C_p is plotted as a function of the distance s along the circumference of the meridional section, normalized with the section circumference, as shown in figure 3.3. The C_p distributions on the section along the spheroid's meridional plane are plotted for $Re = 0.1$ and $Re = 100$ in figures 3.7(*a*) and (*b*), respectively. Referring to figure 3.3, the $\boldsymbol{u}_\infty$ at $\phi = 0°$ is along the $+\xi$ axis and the C_p peaks are observed near $s = 0.5$ in figures 3.7(*a*) and (*b*), which is at the leading edge of the spheroid for

that incident angle. At $Re = 0.1$, we observe an exact match between C_p using the linearity theory (equation 3.3) and the actual simulation for $\phi = 30°$. At $Re = 100$, the actual C_p distribution for $\phi = 30°$ is different compared to the distribution based on linearity theory as seen in figure 3.7(b). Therefore, it can be concluded that it is not due to linearity that the drag law shows sine-squared behaviour at higher Re.

3.4. REASON FOR SINE-SQUARED DRAG LAW AT HIGHER Re

Again we consider the meridional section of the prolate spheroid of aspect ratio 5/2 for this study. We hypothesize that the C_p distribution takes the form

$$C_p = -m + (1 + m)(\hat{\boldsymbol{u}} \cdot \boldsymbol{n})^k. \tag{3.4}$$

Here, m and k are constants, $\hat{\boldsymbol{u}} = \boldsymbol{u}_\infty / |\boldsymbol{u}_\infty|$ is the orientation of the far-field flow direction, and $\boldsymbol{n}$ is the inward facing local unit normal vector, as in figure 3.3. The above form $-m + (1 + m)(\hat{\boldsymbol{u}} \cdot \boldsymbol{n})^k$ is inspired from the inviscid flow around a sphere, where $C_p = 1 - c \sin^2 \theta$ with $c = 9/4$ and the θ measured from the stagnation point. For a sphere, $\hat{\boldsymbol{u}} \cdot \boldsymbol{n} = \cos \theta$ and rearranging terms with $m = c - 1$, the C_p distribution for a sphere becomes $C_p = -m + (1 + m)(\hat{\boldsymbol{u}} \cdot \boldsymbol{n})^2$. A more general form is considered in our case with an arbitrary exponent k.

The term $-m$ acts as a negative offset and the term $(1 + m)$ acts as a scaling factor, such that $C_p = 1$ at the stagnation point ($\hat{\boldsymbol{u}} \cdot \boldsymbol{n} = 1$), as would be expected from Bernoulli's law at the point where $\boldsymbol{u} = \boldsymbol{0}$. For increasing Re, the high pressure region localizes more around the stagnation point and this can be confirmed by comparing the C_p distribution for $\phi = 0°$ at Re=0.1 and 100 in figure 3.7(a) and (b), respectively. Also for $Re \gg 1$, figures 3.8(a) and (b) show that the dominant part of the pressure drag originates from the particle's front side ($\hat{\boldsymbol{u}} \cdot \boldsymbol{n} > 0$, see figure 3.7($c$)) and therefore we focus on this region. For $Re \gg 1$, we choose $k = 2$. The value $k = 2$ is inspired by inviscid irrotational flow theory as discussed above, although the flow is not exactly inviscid. The distributions of C_p for $Re = 100$, $Re = 2000$ (time averaged), and $(\hat{\boldsymbol{u}} \cdot \boldsymbol{n})^2 \mathcal{H}(\hat{\boldsymbol{u}} \cdot \boldsymbol{n})$ are given in figures 3.8(a), (b) and (c) respectively. Here, $\mathcal{H}$ is the Heaviside step function given by

$$\mathcal{H}(x) = \begin{cases} 1 & \text{if } x > 0, \\ 0 & \text{otherwise.} \end{cases} \tag{3.5}$$

The term $\mathcal{H}(\hat{\boldsymbol{u}} \cdot \boldsymbol{n})$ is introduced above to consider only the front side of the particle projected to the inflow.
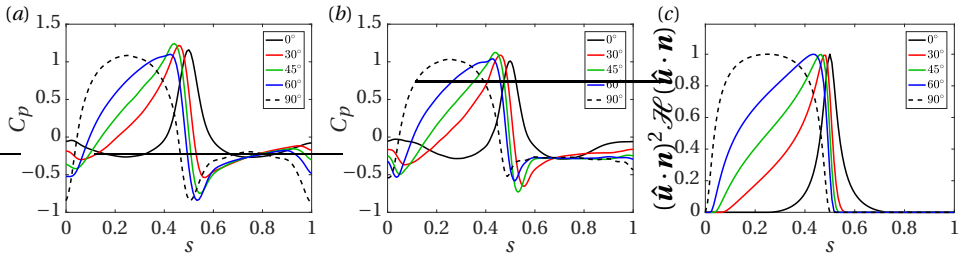
Figure 3.8: Distributions of C_p at (*a*) $Re = 100$, (*b*) $Re = 2000$ (time averaged), and (*c*) second power surface normal projections $(\hat{\boldsymbol{u}} \cdot \boldsymbol{n})^2 \mathcal{H}(\hat{\boldsymbol{u}} \cdot \boldsymbol{n})$ versus the normalized distance s along the circumference of the meridional section for different ϕ.
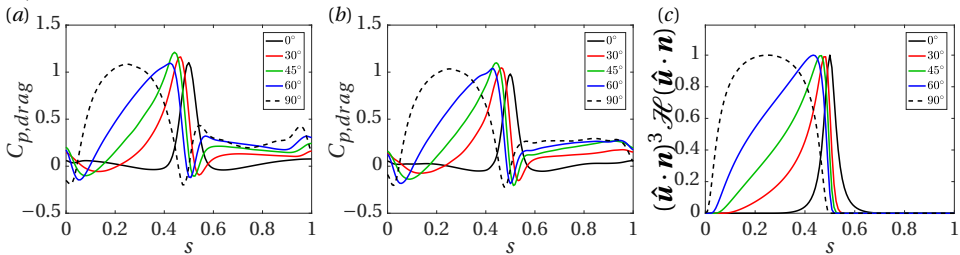

Figure 3.9: Distributions of $C_{p,drag}$ at (*a*) $Re = 100$, (*b*) $Re = 2000$ (time averaged), and (*c*) third power surface normal projections $(\hat{\boldsymbol{u}} \cdot \boldsymbol{n})^3 \mathcal{H}(\hat{\boldsymbol{u}} \cdot \boldsymbol{n})$ versus the normalized distance s along the circumference of the meridional section for different ϕ.
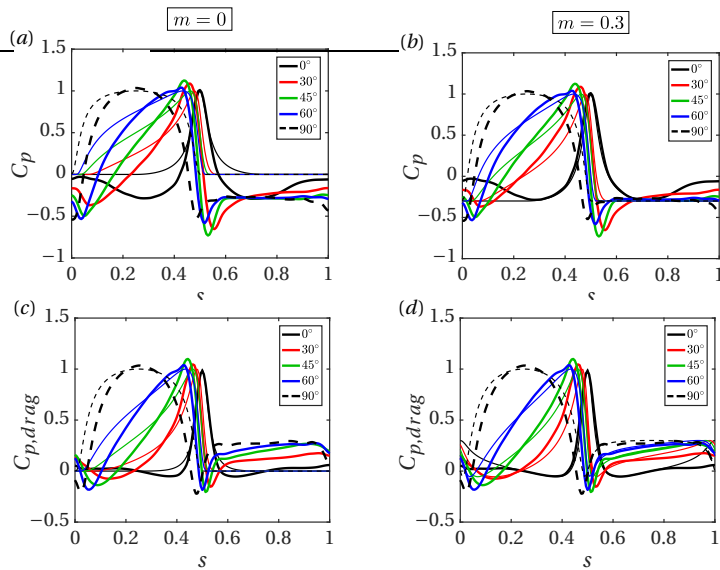
Figure 3.10: Quantitative comparison of the C_p (a, b) and $C_{p,drag} = C_p \hat{\boldsymbol{u}} \cdot \boldsymbol{n}$ (c, d) from the proposed theory (equation 3.4, thin lines) with the actual measurements at $Re = 2000$ (thick lines). We used $m = 0$ (a, c) and $m = 0.3$ (b, d), respectively. Note that the influence of the value of m is weaker for $C_{p,drag}$ compared to C_p.

It can be observed that the maximum values of C_p for different ϕ are nearly the same and close to 1, as expected at the stagnation point in inviscid flow. Also, the overall trend of the C_p curves in figures 3.8(a) and (b), and the $(\hat{\boldsymbol{u}} \cdot \boldsymbol{n})^2 \mathcal{H}(\hat{\boldsymbol{u}} \cdot \boldsymbol{n})$ in figure 3.8(c) are almost similar, including the trends of curvature. Actually for the pressure drag, we specifically need to look at the surface projection of C_p along the flow direction, i.e. $C_{p,drag} = C_p \hat{\boldsymbol{u}} \cdot \boldsymbol{n}$. The similarity between $C_{p,drag}$ and $(\hat{\boldsymbol{u}} \cdot \boldsymbol{n})^3$ for different angles can be observed in figures 3.9(a), (b) and (c). The trends agree well for different incident angles. Further, the C_p and $C_{p,drag}$ distributions for $Re = 100$ and $Re = 2000$ indicate that they are self-similar and independent of Re, at least for the front side of the particle ($\hat{\boldsymbol{u}} \cdot \boldsymbol{n} > 0$). Note that the influence of the offset m is less significant for $C_{p,drag}$ than it is for C_p. Also, the precise value of m may be position and incident angle dependent, but its variation is negligible compared to the overall variation in the pressure drag. This is shown explicitly in figure 3.10, where the measured C_p distributions are compared with our proposed C_p form computed as: $C_p = -m + (1 + m)(\hat{\boldsymbol{u}} \cdot \boldsymbol{n})^2 \mathcal{H}(\hat{\boldsymbol{u}} \cdot \boldsymbol{n})$ and the $C_{p,drag}$ accordingly. The term $\mathcal{H}(\hat{\boldsymbol{u}} \cdot \boldsymbol{n})$ is introduced here to consider C_p distribution only the front side of the particle projected to the inflow. It can be observed that the value m influences C_p considerably (see figure 3.10). However, its influence on $C_{p,drag}$ is much weaker and therefore, we proceed with $m = 0$ in upcoming steps.

$C_{p,drag}$ corresponds to the local contribution of pressure to the sectional pressure drag. Therefore, we require integrals to compute the total pressure drag due to this section. We define the integral of kth power of projection $\hat{\boldsymbol{u}} \cdot \boldsymbol{n}$ for the front side of the section as

$$b_k = \int_0^1 (\hat{\boldsymbol{u}} \cdot \boldsymbol{n})^k \mathcal{H}(\hat{\boldsymbol{u}} \cdot \boldsymbol{n}) \, ds. \tag{3.6}$$

An interesting property is that the integral of the second power of projection, b_2, exactly obeys sine-squared behaviour for different ϕ. This can be written as $b_{2,\phi} = b_{2,\phi=0°} + (b_{2,\phi=90°} - b_{2,\phi=0°}) \sin^2 \phi$ and is shown in figure 3.11(a). This law holds for the family of ellipsoidal sections and is independent of aspect ratio. This can also be confirmed from the fact that the C_p distribution is proportional to $\hat{\boldsymbol{u}} \cdot \boldsymbol{n}$ in Stokes flow (see figures 3.7(a) and (c)) and therefore $C_{p,drag} = C_p \hat{\boldsymbol{u}} \cdot \boldsymbol{n}$ is proportional to $(\hat{\boldsymbol{u}} \cdot \boldsymbol{n})^2$.

As per our earlier observation, at higher Re, the $C_{p,drag}$ distribution is proportional to $(\hat{\boldsymbol{u}} \cdot \boldsymbol{n})^3$. However, the integral $b_{3,\phi}$ does not exactly hold sine-squared behaviour, as shown in figure 3.11(a). It trends slightly below the sine-squared curve. The equivalent of $b_{3,\phi}$ is the sectional pressure drag from the upstream side of the section, which we compare in the upcoming steps. We define sectional pressure drag integrated over the circumference of an ellipsoidal section
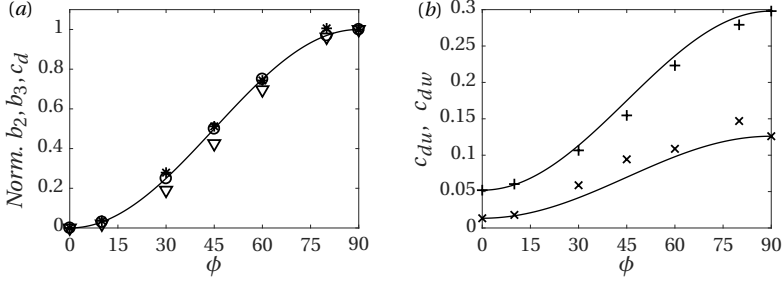
Figure 3.11: For a prolate spheroid of aspect ratio 5/2: (*a*) the normalized $b_{2,\phi}$ (○), $b_{3,\phi}$ (▽), sectional pressure drag $c_{d,\phi}$ at $Re = 2000$ (∗), and $\sin^2 \phi$ (solid line); (*b*) components of sectional pressure drag $c_{d,\phi}$ at $Re = 2000$ decomposed into upstream drag $c_{du,\phi}$ (+) and wake side drag $c_{dw,\phi}$ (×), together with their corresponding sine-squared interpolating curves. Note that the trends of $b_{3,\phi}$ and $c_{du,\phi}$ are similar, both under their respective sine-squared curves.

as

$$c_d = \int_0^1 C_{p,drag} \, ds. \tag{3.7}$$

We then decompose c_d into upstream side (c_{du}) and wake side (c_{dw}), respectively, as

$$c_{du} = \int_0^1 C_{p,drag} \mathcal{H}(\hat{\boldsymbol{u}} \cdot \boldsymbol{n}) \, ds, \quad \text{and} \quad c_{dw} = \int_0^1 C_{p,drag} \mathcal{H}(-\hat{\boldsymbol{u}} \cdot \boldsymbol{n}) \, ds.$$

The above integrals for different incident angles ϕ, i.e. $c_{du,\phi}$ and $c_{dw,\phi}$, for $Re = 2000$ are plotted in figure 3.11(*b*) and their corresponding sine-squared interpolation curves based on the end values. As seen from figures 3.11(*a*) and (*b*), the upstream drag $c_{du,\phi}$ trend is very similar to $b_{3,\phi}$ and both are slightly below their respective sine-squared curves. At the same time, the wake induced drag component $c_{dw,\phi}$ values are slightly above their respective sine-squared curve at the intermediate angles, i.e. $0° < \phi < 90°$. Therefore, the wake drag adequately compensates the upstream drag proportionately at the intermediate angles and thereby making the total section drag appear to scale in a sine-squared manner. The normalized, sectional pressure drag $c_{d,\phi}$ for different angles for $Re = 2000$ itself follows near sine-squared pattern as shown in figure 3.11(*a*). The spheroid by itself is made of different such ellipsoidal sections, each obeying sine-squared behaviour of different scales and altogether giving the total drag sine-squared behaviour. We have tested the reasoning in this section for different aspect ratio prolate spheroids, and found similar dependencies of $C_{p,drag}$ with $(\hat{\boldsymbol{u}} \cdot \boldsymbol{n})^3 \mathcal{H}(\hat{\boldsymbol{u}} \cdot \boldsymbol{n})$ for different ϕ.
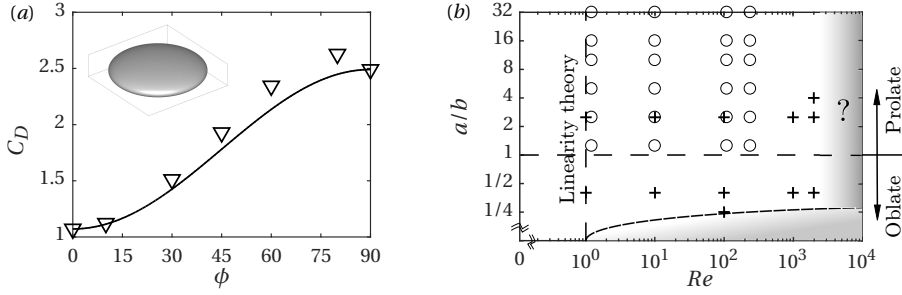
Figure 3.12: (*a*) C_D against ϕ at $Re = 100$ for oblate spheroid of aspect ratio 4 ($\triangledown$) and the corresponding sine-squared interpolating curve (solid line), (*b*) the tested data points (+) and the *plausible* valid region for sine-squared scaling (unshaded). The valid region is based on our results and the data of Ouchene *et al.* (2016) for prolate spheroids upto aspect ratios 32 and $Re = 240$ ($\circ$). The ratio a/b is the ratio of lengths parallel and orthogonal to the axis of rotation.

3.4.1. LIMITATIONS AND COMMENTS

In the introduction, we showed results of prolate spheroids of different aspect ratios and an oblate spheroid of ratio 5/2. However, increasing the aspect ratio for an oblate spheroid results in an increasing digression from the sine-squared drag law, even at moderate Re. The C_D results of oblate spheroid of aspect ratio 4 at $Re = 100$ are presented in figure 3.12(*a*). Clearly, a non-monotonic dependence of C_D on the incidence angle ϕ is observed. The observed maximum deviation is around 10% at $\phi = 60°$ against the sine-squared curve. The reason why the drag law fails for flatter discs can be explained from our earlier observation that the wake has a higher drag contribution at intermediate angles $0° < \phi < 90°$ (see c_{dw} in figure 3.11(*b*)), when compared with the sine-squared curve. The flat-disc like geometry experiences a stronger wake, amplifying the effect strongly. If we assume a 10% deviation to be the limit of applicability, the oblate spheroid of aspect ratio 4 is at the bounding limit for the drag law. On the other hand, prolate spheroids of larger aspect ratio, as shown in the introduction, still obey the sine-squared behaviour even at $Re = 2000$, due to the weaker wake side drag. A sketch of the *plausible* valid region of the sine-squared behaviour is shown in figure 3.12(*b*). We have also tested a capsule-like spherocylinder of aspect ratio 4 and it also exhibits sine-squared drag scaling at high Re, due to closer resemblance to prolate spheroid. The C_D results are published as correlations dependent of Re and ϕ in the following chapter. Since the prolate spheroid of aspect ratio 4 is simulated only for $Re = 2000$, the corresponding results are given here, with $C_{D,\phi=0°} = 0.147$ and $C_{D,\phi=90°} = 1.105$.

The $Re = 2000$ limit for the tested particles is rather limited by the LBM solver and not by the flow physics itself. We believe that the drag law might hold to even higher Re. However, flow fields are indeed complex for high Re and the extent to which the drag law is valid needs further investigation. For example, Jiang *et al.* (2015) simulated flow around a 6:1 prolate spheroid at $\phi = 45°$ at $Re = 3000$ based on minor diameter. They reported a side force, almost 75% in magnitude of the drag force, perpendicular to the meridional plane. This indicates the flow is highly asymmetric about the meridional plane. However, they do not investigate the incident angle dependence of the drag force. To which extent their reported flow asymmetries might influence the sine-squared drag behaviour is not yet known and therefore needs further investigation.

3.5. LIFT FORCES

Besides drag, any non-spherical particle at an inclination with respect to a uniform flow will experience lift. Here, we provide a concise section with interesting observations and comments regarding the lift forces.

For a particle in the Stokes regime, based on linearity theory, the C_L at an incident angle ϕ is

$$C_{L,\phi} = (C_{D,\phi=90°} - C_{D,\phi=0°})\sin\phi\cos\phi. \tag{3.8}$$

The proof of equation 3.8 is given in appendix A.

From our experience of the different non-spherical particles tested, equation 3.8 is still a *decent approximation* in the complete absence of C_L data for prolate spheroids, even at high Re, as seen in figure 3.13(*a*). The average of the absolute deviations between $C_{L,\phi}$ from the simulations and the equation 3.8 is less than 15% for the tested prolate spheroids at different Re. For oblate spheroids, with increasing aspect ratios, the deviations increase more, as seen in figure 3.13(*b*). For the oblate spheroid of aspect ratio 4 at $Re = 100$, the simulated C_L is much larger, by around 60%, than the theory for the reasons already observed in figure 3.11(*b*). Similar to the drag, the wake induced force is also contributing strongly to the lift and thereby making the observed C_L much larger than the theory at intermediate incident angles.

There are different reasons the incident angle dependence of the lift coefficient C_L cannot be *accurately* quantified in a predictable fashion like that of C_D. The lift coefficient's order of magnitude depends on the difference of C_D at two extreme incident angles, i.e. $(C_{D,\phi=90°} - C_{D,\phi=0°})$ and goes to zero at the extreme ends of incident angles, i.e. at $\phi = 0°, 90°$. However for C_D at different incident angles ϕ, apart from the C_D difference term, there is an additional term giving a

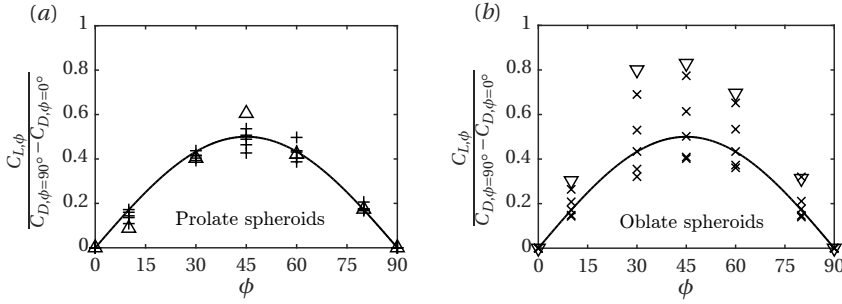Figure 3.13: The normalized lift coefficient $\dfrac{C_{L,\phi}}{C_{D,\phi=90°} - C_{D,\phi=0°}}$ plotted against incident angle ϕ. The solid line indicates $\sin\phi\cos\phi$. (*a*) prolate spheroid of aspect ratio 5/2 for Re=0.1, 10, 100, 1000 and 2000 (+); prolate spheroid of aspect ratio 4 at Re=2000 ($\triangle$), and (*b*) oblate spheroid of aspect ratio 5/2 for Re=0.1, 10, 100, 1000 and 2000 ($\times$); oblate spheroid of aspect ratio 4 at $Re = 100$ ($\triangledown$). Note that the oblate spheroids are experiencing stronger deviations compared to prolate spheroids.

constant offset, i.e. C_D at $\phi = 0°$. In other words, the magnitudes of C_D are much larger compared to that of C_L for a given Re and ϕ. This implies that the variation of $C_{L,\phi}$ is much more sensitive than that of $C_{D,\phi}$. Therefore, any variation in pressure distribution at higher Re would be more amplified for C_L than for C_D. The C_L results are also reported as correlations dependent of Re and ϕ in the next chapter.

3.6. CONCLUSION

The flow around prolate and oblate spheroids of different aspect ratios was studied. We explored the sine-squared drag law in detail with a prolate spheroid of aspect ratio 5/2. We found that the reason for the drag law at high Re is not due to linearity theory, which results in an identical drag law in the Stokes regime. At high Re, the viscous drag becomes almost independent of incident angle ϕ and the pressure drag is the only factor influenced by incident angle ϕ. At high Re, the pressure distribution contributing to the drag shows a dependency of the surface normal's orientation with the incoming flow in a consistent pattern as discussed. Prolate spheroids of higher aspect ratios follow the sine-squared pattern even at $Re = 2000$. Oblate spheroids of aspect ratio 4 or larger do not exhibit sine-squared pattern due to strong wake induced drag. Regarding lift coefficients, we find that the theoretical C_L equation can provide a decent approximation, even at high Re, for prolate spheroids.

Both the drag law, valid at high Re for the prolate spheroids and low aspect ratio oblate spheroids, and the lift law for the prolate spheroids, hold good potential for different applications. For example, they are very useful for Euler-Lagrangian flow simulations of non-spherical particles. Any particle shape-specific C_D and C_L for a given Re at different ϕ, even at high Re, can be obtained by performing just two simulations: C_D at $\phi = 0°$ and $\phi = 90°$.

4

HYDRODYNAMIC FORCES AND TORQUE ON ISOLATED NON-SPHERICAL PARTICLES

Accurate direct numerical simulations are performed to determine the drag, lift and torque coefficients of non-spherical particles. The motivation for this work is the need for accurate drag, lift and torque correlations for high Re regimes, which are encountered in Euler-Lagrangian simulations of fluidization and pneumatic conveying of larger non-spherical particles. The simulations are performed in the Reynolds number range 0.1 ≤ Re ≤ 2000 for different incident angles φ. Different tests are performed to analyse the influence of grid resolution and confinement effects for different Re. The measured drag, lift and torque coefficients are utilized to derive accurate correlations for specific non-spherical particle shapes. The functional forms for the correlations are chosen to agree with the expected physics at Stokes flow as well as the observed leveling off of the drag coefficient at high Re flows. Therefore the fits can be extended to regimes outside the Re regimes simulated. We observe sine-squared scaling of the drag coefficient for the particles tested even at Re = 2000 and sine-cosine scaling for lift coefficient for the elongated particles. The current work would greatly improve the accuracy of Euler-Lagrangian simulations of larger non-spherical particles considering the existing literature is mainly limited to steady flow regimes and lower Re.

4.1. INTRODUCTION

Particulate suspensions are involved in different natural and man-made processes. Examples are red blood cells in plasma, fluidization of pulverized coal and milled biomass, and fibrous pulps in the paper manufacturing industry, etc. Traditionally, particulate suspension studies simplify the particles as spheres (Ladd, 1994*a,b*; Ladd & Verberg, 2001; Beetstra *et al.*, 2007), thereby eliminating orientation and shape effects. In general, simplifying non-spherical particles with an equivalent sphere can provide an approximate drag prediction, but the effects of lift and torque and also their dependence with orientation are often ignored. The spherical particle approximation for applications like fluidized beds with non-spherical particles could significantly influence the minimum fluidization velocity, power consumption and also affect the overall bed dynamics (Hilton *et al.*, 2010). Therefore, quantification of the effects of particle orientation on drag, lift and torque is important.

In the Stokes limit, theoretical investigations are available for different non-spherical particles. Oberbeck (1876) derived the drag for translation of a spheroid parallel to its principal axis. Jeffery (1922) studied the motion of an ellipsoid in shear flow. He suggested that the ellipsoidal particle translates in a way corresponding to least dissipation of energy, and that the final state depends on the initial state of the particle. Several empirical drag correlations have been proposed in the past for isolated non-spherical particles as a function of the Reynolds number Re. Leith (1987) extended Stokes' law for a sphere to arbitrary non-spherical objects by decomposing the pressure and viscous components and accordingly using the object's projected area and surface area, respectively, to represent the total drag.

Haider & Levenspiel (1989) proposed a drag correlation for arbitrary particles as a function of sphericity, but not considering the orientation. Ganser (1993) compiled experimental data of several non-spherical shapes and proposed a drag correlation as a function of two shape factors, namely Stokes' and Newton's shape factors. Recently, Hölzer & Sommerfeld (2008) proposed a drag correlation based on a large set of numerical and experimental data, involving two different projected areas to account for particle orientation. Hölzer & Sommerfeld (2009) and Zastawny *et al.* (2012) investigated different non-spherical particles at different flow incident angles ϕ and Re, albeit limiting mainly to the steady flow regime. Richter & Nikrityuk (2012, 2013) simulated heat transfer and drag of an ellipsoid and a cube. Very recently, Ouchene *et al.* (2016) proposed force and torque correlations for prolate spheroids, applicable to a range of aspect ratios up to 32. Their work was limited to steady flows with $Re \leq 240$.

Zastawny *et al.* (2012) provide correlations for drag, lift and torque based on

immersed boundary direct numerical simulations (DNS). Their particle's equivalent volume sphere diameters (d_{eq}) range between 8 to 12 grid cells for Re from 0.1 upto 300. However, their work does not provide a detailed study on the influence of grid resolution as function of Re. Even their highest resolution of $d_{eq} = 12$ implies that the critical minimum thickness would be of the order of a few cells for high aspect ratio disk and a fibre of aspect ratio 5. In our current work, detailed studies on grid resolution and wall confinement effects are performed for different Re. We also observe that the Zastawny *et al.* (2012) results are not accurate at Stokes flow, but improve at larger Re. Similar deviations in the results of Zastawny *et al.* (2012) have also been observed by Ouchene *et al.* (2015, 2016).

Some authors define the Reynolds number Re_d based on the minimum thickness of the particle d_{min}. For this work, the Reynolds number is defined as

$$Re = |\boldsymbol{u}_\infty| d_{eq} / \nu, \tag{4.1}$$

where $\boldsymbol{u}_\infty$ is the uniform inlet velocity, d_{eq} is the diameter of the volume-equivalent sphere, and ν is the kinematic viscosity of the fluid. The drag, lift and torque coefficients respectively are defined as

$$C_D = |\boldsymbol{F}_D| / (\frac{1}{2} \rho_f |\boldsymbol{u}_\infty|^2 \frac{\pi}{4} d_{eq}^2), \tag{4.2}$$

$$C_L = |\boldsymbol{F}_L| / (\frac{1}{2} \rho_f |\boldsymbol{u}_\infty|^2 \frac{\pi}{4} d_{eq}^2), \text{ and} \tag{4.3}$$

$$C_T = |\boldsymbol{T}| / (\frac{1}{2} \rho_f |\boldsymbol{u}_\infty|^2 \frac{\pi}{8} d_{eq}^3). \tag{4.4}$$

Here, $\boldsymbol{F}_D, \boldsymbol{F}_L$ and $\boldsymbol{T}$ are drag, lift, and pitching torque acting on the particle, and ρ_f is the fluid density.

The motivation for this work is the need for highly accurate C_D, C_L, and C_T correlations for high Re regimes, which are encountered in Euler-Lagrangian simulations of fluidization and pneumatic conveying of larger non-spherical particles. We performed such simulations of spherocylindrical (biomass-like, type Geldart D) particles of aspect ratio 4, using the Hölzer & Sommerfeld (2008) drag correlation with Di Felice (1994) voidage correction. The resulting distribution of particle Re encountered during the simulation is plotted in figure 4.1. It can be observed that the median of the distribution is around $Re \approx 1200$ and the maximum is around $Re \approx 2000$. For this Re range, we perform fully resolved simulations of the fluid flow around the particles using the lattice Boltzmann method (LBM) and suitably parametrize the simulation data to obtain the C_D, C_L, and C_T correlations.

The work of Rubinstein *et al.* (2017) (in their figure 2) shows that fixed particle simulations are sufficient to compute forces in moving particulate systems,
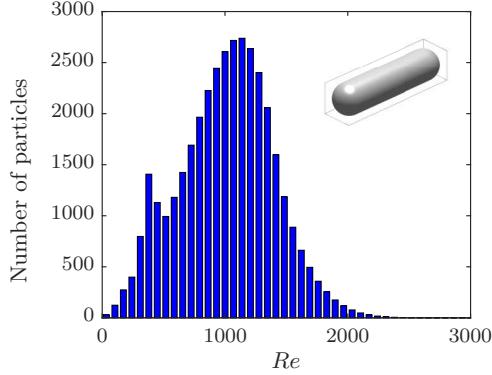
Figure 4.1: Time-averaged distribution of particle Re from Euler-Lagrangian fluidization simulations of spherocylindrical particles of aspect ratio 4 (inset).

provided the Stokes number (St) is sufficiently high, around $St \geq 10$. The Stokes number is the measure of timescales of the particle against the fluid. The relation between St and Re is given by $St = (\rho_p/(18\rho_f))Re$, where ρ_p is the particle density. The above relationship is of order $St = 50Re$ for gas-solid systems (assuming a typical value of ρ_p/ρ_f of 10^3) and therefore generally results in very large Stokes numbers. Therefore, in gas-solid fluidization and other typical engineering applications such as pneumatic conveying, riser flows, etc., a quasi-steady particle orientation assumption can be applied for Euler-Lagrangian simulations.

The simulated non-spherical particles are shown in figure 4.2. LBM simulations for high Re flows have been performed in the past. Eitel-Amor *et al.* (2013) performed detailed simulations of flow past a sphere in the laminar regime of $100 \leq Re \leq 300$ and sub-critical turbulent flow regime $3700 \leq Re \leq 10000$ using a single-relaxation scheme (SRT) with hierarchical grid refinement. In this work, we use a multi-relaxation time (MRT) LBM scheme, which adds stability required for the high Re simulations. Kruggel-Emden *et al.* (2016) provide a good overview of coupled fluid flow and heat transfer simulations for particulate flows using LBM.

For Stokes flow (Happel & Brenner, 1983), C_D and C_L at different incident angle ϕ are given by

$$C_{D,\phi} = C_{D,\phi=0°} + (C_{D,\phi=90°} - C_{D,\phi=0°})\sin^2\phi, \tag{4.5}$$

$$C_{L,\phi} = (C_{D,\phi=90°} - C_{D,\phi=0°})\sin\phi\cos\phi. \tag{4.6}$$

Interestingly, for all the investigated particles, C_D scales as a *sine-squared* function as in equation 4.5, even for Reynolds numbers as high as 2000. Further, C_L also scales as $\sin\phi\cos\phi$ as in equation 4.6, for the *elongated* particles even at
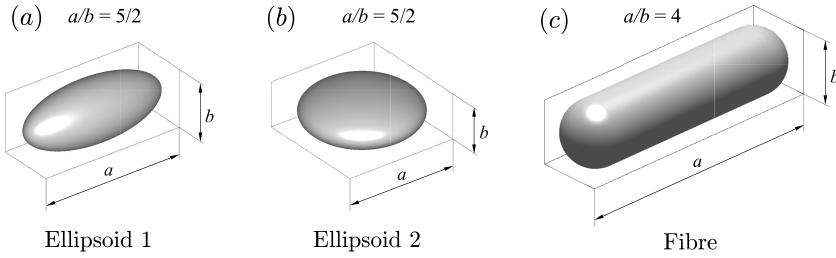
Figure 4.2: Different non-spherical particles simulated in this work: (*a*) Ellipsoid 1 - a prolate spheroid of aspect ratio 5/2, (*b*) Ellipsoid 2 - an oblate spheroid of aspect ratio 5/2, and (*c*) Fibre - a spherocylinder of aspect ratio 4.

Re = 2000. Equations 4.5 and 4.6 arise from the linearity of the Navier-Stokes equations in the Stokes regime. We have investigated these scaling phenomena in detail for high Re (Sanjeevi & Padding, 2017). However, we found that the real cause is due to the dependency of pressure on the local surface normal's orientation with the incoming flow and not due to the flow linearity as in Stokes flow.

To the best of our knowledge, the present work is the only work that in detail investigates different non-spherical particles upto high Reynolds numbers of Re = 2000 for different incident angles $0° \leq \phi \leq 90°$. There have been similar works providing C_D, C_L, and C_T correlations as a function of Re and ϕ (Zastawny *et al.*, 2012; Richter & Nikrityuk, 2013; Ouchene *et al.*, 2016), but our work considers approximately an order of magnitude larger Re than these studies. By extending the measurements to larger flow velocities, our correlations take into account the leveling off of the drag coefficient observed at higher Re. Note that our work does not aim to give a generic correlation for *all* particle shapes and/or aspect ratios. Rather, by defining separate correlation functions for each specific particle shape and aspect ratio, we are able to derive more accurate correlation functions for the chosen particle shapes.

This work will be helpful for the community dealing with Euler-Lagrangian simulations of non-spherical particles, for practical industrial applications such as biomass fluidization, pneumatic conveying and riser flows of non-spherical particles.

4.2. NUMERICAL METHOD

The numerical method applied is the MRT-LBM scheme already discussed in chapter 2. Here, we explain the interpolated bounce back scheme used and the computational details of particle geometry-lattice direction intersection.
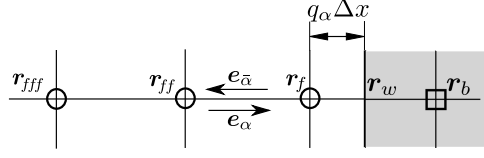
Figure 4.3: The linearly interpolated bounce-back scheme simplified in one-dimension.

4.2.1. Interpolated bounceback scheme

The conventional no-slip boundary in LBM is based on the simple bounce-back scheme, which approximates the geometry in stair-case form. The effects of such an approximation are more pronounced at high Reynolds number, where the boundary layers are thinner, resulting in poor accuracy. In our simulations, we use a linearly interpolated bounce back scheme (Bouzidi *et al.*, 2001) to accurately consider the curved geometry of the particle. A simplified one-dimensional interpolated bounce-back scheme is shown in figure 4.3. The parameter q_α is the fractional distance along the direction α of the fluid node to the actual wall and is given by $q_\alpha = |\boldsymbol{r}_w - \boldsymbol{r}_i|/|\boldsymbol{r}_b - \boldsymbol{r}_i|$. Depending on whether $q_\alpha < 1/2$ or $q_\alpha \geq 1/2$, two different cases are to be considered:

$$f_{\bar\alpha}(\boldsymbol{r}_i, t) = 2q_\alpha \hat{f}_\alpha(\boldsymbol{r}_i, t) + (1 - 2q_\alpha)\hat{f}_\alpha(\boldsymbol{r}_j, t), \qquad q_\alpha < 1/2, \qquad (4.7)$$

$$f_{\bar\alpha}(\boldsymbol{r}_i, t) = \frac{1}{2q_\alpha}\hat{f}_\alpha(\boldsymbol{r}_i, t) + \frac{(2q_\alpha - 1)}{2q_\alpha}\hat{f}_{\bar\alpha}(\boldsymbol{r}_i, t), \qquad q_\alpha \geq 1/2. \qquad (4.8)$$

Here the subscript $\bar\alpha$ denotes the opposite direction of α. The notations $\hat{f}_\alpha$ and f_α denote the post-collision distribution functions before and after advection. From an implementation point of view, storing the distribution before and after advection ($\hat{f}_\alpha$ and f_α) results in additional memory burden. Therefore, Lallemand & Luo (2003) suggested to make use of the fact that advection is simply a spatial shifting of distributions, and that therefore the indices can be accordingly modified as

$$f_{\bar\alpha}(\boldsymbol{r}_i, t) = 2q_\alpha f_\alpha(\boldsymbol{r}_i + \boldsymbol{e}_\alpha\Delta t, t) + (1 - 2q_\alpha)f_\alpha(\boldsymbol{r}_i, t), \qquad q_\alpha < 1/2, \qquad (4.9)$$

$$f_{\bar\alpha}(\boldsymbol{r}_i, t) = \frac{1}{2q_\alpha}f_\alpha(\boldsymbol{r}_i + \boldsymbol{e}_\alpha\Delta t, t) + \frac{(2q_\alpha - 1)}{2q_\alpha}f_{\bar\alpha}(\boldsymbol{r}_i - \boldsymbol{e}_\alpha\Delta t, t), \qquad q_\alpha \geq 1/2. \qquad (4.10)$$

The linear interpolation scheme was chosen for the no-slip boundary, as the parallel code requires only one layer of ghost cells as opposed to two layers in case of a quadratic scheme, resulting in additional communication overhead. Further, the improvement in solution accuracy is negligible between linear and quadratic
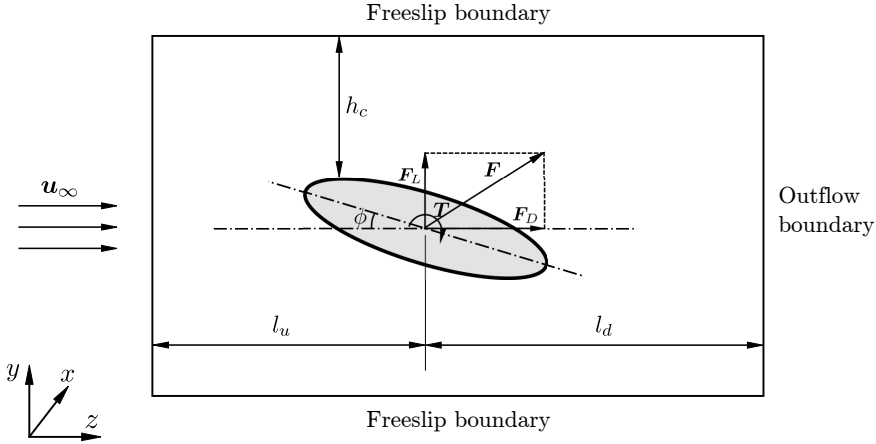
Figure 4.4: Simulation domain, the forces and torque acting on the particle and the boundary conditions.

interpolation schemes, provided sufficient resolution is used (Kruggel-Emden *et al.* (2016); Pan *et al.* (2006)). For the shapes considered - prolate & oblate ellipsoids and spherocylinder - the distance from fluid node to the wall boundary along the velocity directions are computed using ray-geometry intersection algorithms (Akenine-Möller *et al.*, 2008). As ellipsoids can be described by a single equation, the ray-ellipsoid intersection is solved as a single problem. The ray-spherocylinder intersection is decomposed into three ray-intersection problems - (i) ray-cylinder and (ii) two ray-sphere intersection problems for the top and bottom hemispheres.

4.2.2. BOUNDARY CONDITIONS AND FORCE EVALUATION

The schematic geometry of the domain is described in figure 4.4. A uniform velocity is prescribed at the inlet based on Hecht & Harting (2010), which extends the Zou and He boundary condition (Zou & He, 1997) to a D3Q19 lattice. The side walls are prescribed as free-slip boundary rather than as periodic boundary condition, which could cause the flow to deflect either up or down based on inclination of the non-spherical particle (Hölzer & Sommerfeld, 2009). The downstream (outlet) is specified by an axial-stress-free boundary condition with $\partial u_z / \partial z = 0$ (Aidun *et al.*, 1998). All the simulations are initialized with uniform inlet velocity in the domain. The momentum contribution along a single fluid-solid link exerted on the particle by the fluid is computed using the momentum exchange method (Bouzidi *et al.*, 2001; Mei *et al.*, 2002; Lallemand & Luo, 2003)
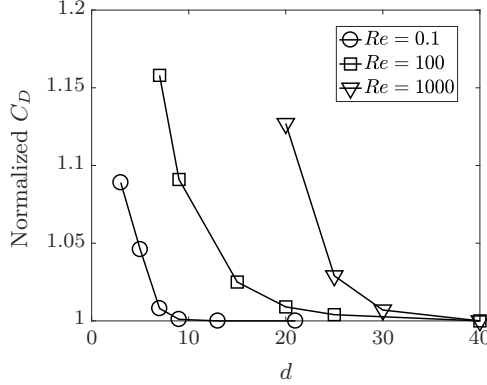
Figure 4.5: Normalized drag coefficient C_D of a sphere as function of particle resolution in diameter d (in lattice cells) for different Re.

as

$$\boldsymbol{p}_\alpha(\boldsymbol{r}_b, t) = \boldsymbol{e}_\alpha(f_\alpha(\boldsymbol{r}_b, t) + f_{\overline{\alpha}}(\boldsymbol{r}_i, t)). \tag{4.11}$$

Correspondingly, the force and torque are computed as

$$\boldsymbol{F} = \sum_{\text{all } \boldsymbol{r}_b} \sum_{\alpha \neq 19} \boldsymbol{p}_\alpha(\boldsymbol{r}_b, t) \tag{4.12}$$

$$\boldsymbol{T} = \sum_{\text{all } \boldsymbol{r}_b} \sum_{\alpha \neq 19} (\boldsymbol{r}_w - \boldsymbol{r}_c) \times \boldsymbol{p}_\alpha(\boldsymbol{r}_b, t). \tag{4.13}$$

Here $\boldsymbol{r}_c$ is the center of gravity of the particle.

4.2.3. GRID RESOLUTION AND DOMAIN INDEPENDENCE STUDY

Before proceeding to the simulations of non-spherical particles, the influence of grid resolution and domain size at different Re are assessed. The influence of grid resolution is tested with flow around an isolated sphere. The normalized C_D for different Re is plotted in figure 4.5. The normalization is done using the highest resolution C_D and not against any popularly available C_D correlations for a sphere. This is because at high Re, the C_D value becomes smaller and the available correlations themselves have minor deviations compared to the true C_D. This would be amplified strongly for small C_D values and therefore are not the best choice. Three different regimes are tested: (i) Stokes flow, (ii) intermediate Reynolds number at $Re = 100$ with a steady wake, and (iii) high Reynolds number $Re = 1000$ exhibiting complex, unsteady wake behind the sphere (in which case the mean C_D is reported). The influence of grid resolution is stronger with
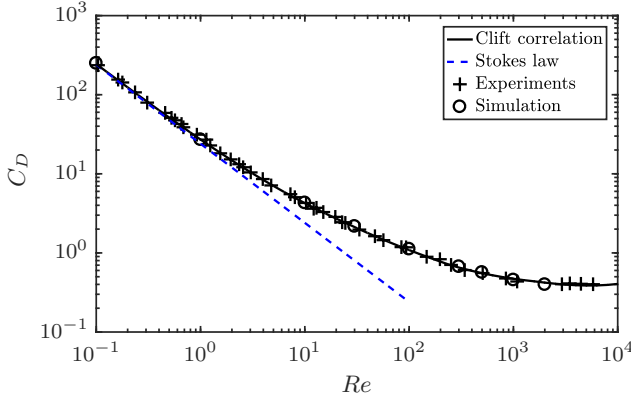
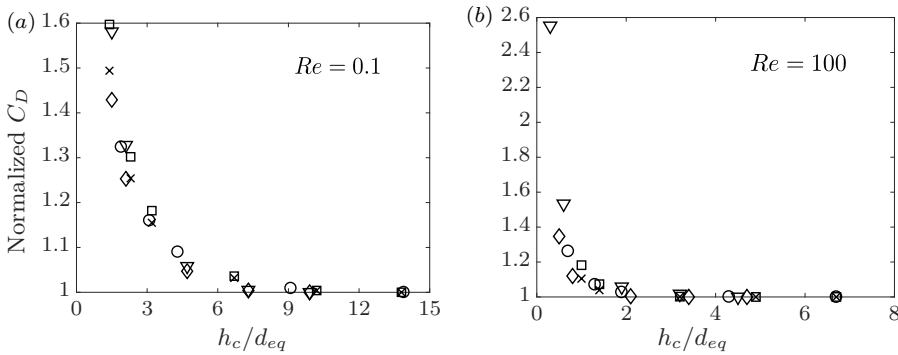Figure 4.6: C_D at different Re for flow around sphere.

Figure 4.7: Influence of the clearance for (*a*) $Re = 0.1$ and (*b*) $Re = 100$. (○) sphere, ellipsoid 1 at (×) $\phi = 0°$ and (□) $\phi = 90°$, ellipsoid 2 at (◇) $\phi = 0°$ and (▽) $\phi = 90°$.

increasing Re, as seen in figure 4.5. For $Re = 1000$, we observe $C_D = 0.456$ at resolution $d_{eq} = 40$, which is in good agreement with the literature result, $C_D = 0.464$ from Vakarelski *et al.* (2016). The absolute C_D values for flow around sphere at different Re from our simulations are given in figure 4.6 along with the Clift correlation as listed in Brown & Lawler (2003). It can be observed that there is good match from our results compared with the Clift correlation and also the experimental results at different Re.

The influence of the presence of side walls (confinement effect) is tested as a function of h_c/d_{eq}, where h_c is the clearance between the particle and the side walls (see figure 4.4), which is kept the same for the four lateral walls for a particular Re. Tests are performed for a sphere, ellipsoid 1 and ellipsoid 2 for $Re = 0.1$

| Re | d_{min} | | | h_c/d_{eq} | l_u/d_{eq} | l_d/d_{eq} |
	Ellipsoid 1	Ellipsoid 2	Fibre			
$0.1 \leq Re < 10$	16	16	16	10	10	10
$10 \leq Re \leq 100$	20	20	20	7	7.5	7.5
300	30	20	20	5	5	10
$1000, 2000$	40	30	30	4.5	5	10

Table 4.1: Details of the particle resolution in lattice cells and domain sizes at different Re. d_{min} is the minimum thickness of the particle.

and $Re = 100$. It can be observed from figure 4.7 that all the different geometries have consistent confinement effects for different Re, provided the clearance h_c is used to characterize confinement rather than particle center to wall distance. As observed, between $Re = 0.1$ and $Re = 100$, the wall effects tend to become weaker for increasing Re and therefore confinement tests for $Re > 100$ are not presented here. For simulations with $Re > 100$, random confinement tests are performed and also literature data (Zastawny *et al.*, 2012) are used for selecting appropriate h_c. It has been observed that $h_c \geq 4.5$ is sufficient to produce confinement independent results, as the viscous effects get weaker for increasing Re. Therefore, we maintained at least $h_c = 4.5$ for $Re > 100$.

Different simulations have different particle resolutions, upstream length l_u, downstream length l_d, and clearance h_c, depending on the Re. An extensive study regarding the upstream and downstream lengths is avoided to simplify the parameter space. Again, we have examined different literature containing flows around particles regarding the domain lengths (Zastawny *et al.*, 2012; Hölzer & Sommerfeld, 2009). With this information, we have selected the upstream and downstream lengths. From our experience, only the downstream length is found to be significantly influencing results, specifically at high Re. Therefore, we have kept downstream length sufficiently long with $l_d/d_{eq} = 10$ for $Re \geq 300$ to avoid any influence of outflow boundary on the particle wake.

The influence of particle resolution (see figure 4.5) and the effects of domain size (see figure 4.7) at different Re are considered carefully on choosing the particle sizes. The chosen particle resolutions and the simulation domain sizes are listed in table 4.1. It has to be noted that the listed resolutions are the least thickness (d_{min}) of the particle. The other dimensions are always larger than d_{min} and therefore a good particle resolution is ensured. Since the grid independence study is performed prior to the actual simulations, the particle resolution is chosen such that the deviations are less than 3% of the true value.
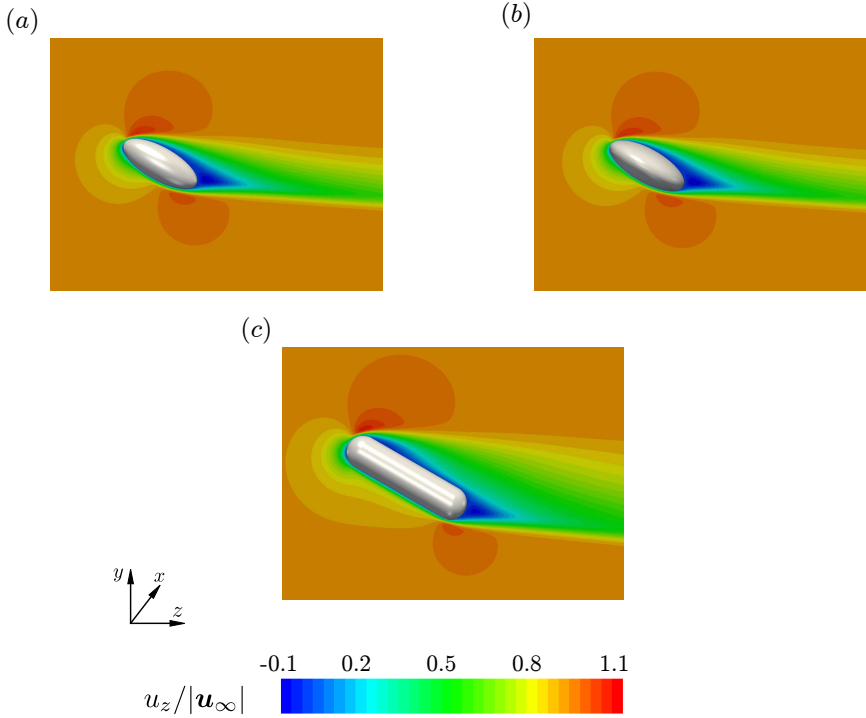
(a)

(b)

(c)

y ↑ x
z

-0.1   0.2   0.5   0.8   1.1

$u_z/|\boldsymbol{u}_\infty|$

Figure 4.8: Velocity contours for flow around different particles at $Re = 300$ and $\phi = 30°$: (a) ellipsoid 1, (b) ellipsoid 2, and (c) fibre.

4.3. FLOW AROUND VARIOUS NON-SPHERICAL PARTICLES

Detailed LBM simulations of the flow around 3 different non-spherical particles are performed. The simulated range of Reynolds number is $0.1 \leq Re \leq 2000$ at incident angles $0° \leq \phi \leq 90°$. As an example, the flow around different particles at $Re = 300$ and $\phi = 30°$ is shown in figure 4.8. Apart from producing accurate results through the simulations, fitting the observed data to a custom function, which has the least relative deviation is itself a challenge. As we will discuss, the functional form of the correlation should have relevant physical backing to produce the best fit and also to be applicable to extended Re ranges. We considered the physics carefully while proposing the functional forms. The magnitude of the relative deviation between the correlation and simulation data is globally minimized using a Python optimization function. We used Powell's method (Powell, 1964), which was found to be best among the available optimization methods for our data.

4.3.1. DRAG

We simulated different non-spherical particles at different incident angles ϕ and Re. The resulting C_D at different ϕ for various Re are plotted in figure 4.9. It can be noted that the exponent of the $\sin(\phi)$ term in the fits of C_D in Zastawny *et al.* (2012) are very close to 2 (see table 2 in Zastawny *et al.* (2012)). The same has been observed by Ouchene *et al.* (2016) for different prolate spheroids of aspect ratios upto 32. It might be tempting to relate this finding to a similar correlation expected in the Stokes flow for non-spherical particles. We have investigated this sine-squared behaviour for different non-spherical particles, both in the Stokes limit and at Re as high as 2000 (Sanjeevi & Padding, 2017). Surprisingly, the tested non-spherical particles exhibited *sine-squared* dependence of the mean C_D, even for complex unsteady flows at $Re = 2000$. We found that the linearity assumption, the reason for the sine-squared behaviour in the Stokes regime, does not hold at high Re, as may have been expected due to the flow non-linearities occurring at high Re. Rather, we find that the pressure distribution along the particle surface for different ϕ scales in a particular pattern. The pattern is dependent on the angle between the particle's surface-normal and the direction of the incident flow. This leads to the observed near *sine-squared* phenomenon. The phenomenon is found to be primarily holding for different elongated particles such as prolate spheroids, spherocylinders as well as low aspect ratio oblate spheroids. Flatter, high aspect ratio oblate spheroids do not exhibit the sine-squared dependence for reasons discussed in Sanjeevi & Padding (2017).

Initially, we considered the use of correlations similar to the popularly available Zastawny *et al.* (2012) form, since their form is quite flexible to capture the dependencies of C_D on Re and ϕ. Since the Re range is much larger in our case, with $0.1 \leq Re \leq 2000$ compared to $0.1 \leq Re \leq 300$ studied by Zastawny *et al.* (2012), our proposed correlations require further modifications. For reasons mentioned already, our proposed form takes an exponent 2 for the sine-term. We correlate the measured C_D at different Re and ϕ for the different tested non-spherical particles in the following form:

$$C_{D,\phi} = C_{D,\phi=0°} + (C_{D,\phi=90°} - C_{D,\phi=0°})\sin^2\phi \qquad (4.14)$$

with

$$C_{D,\phi=0°,90°} = \left(\frac{a_1}{Re} + \frac{a_2}{Re^{a_3}}\right)e^{-a_4 Re} + a_5(1 - e^{-a_4 Re}) \qquad (4.15)$$

The coefficients for the C_D correlation at $0°$ and $90°$ incident angle are listed in table 4.2. The table values close to 0 should not be ignored as they have a strong influence at high Re. Physically, the C_D should exhibit $1/Re$ scaling at
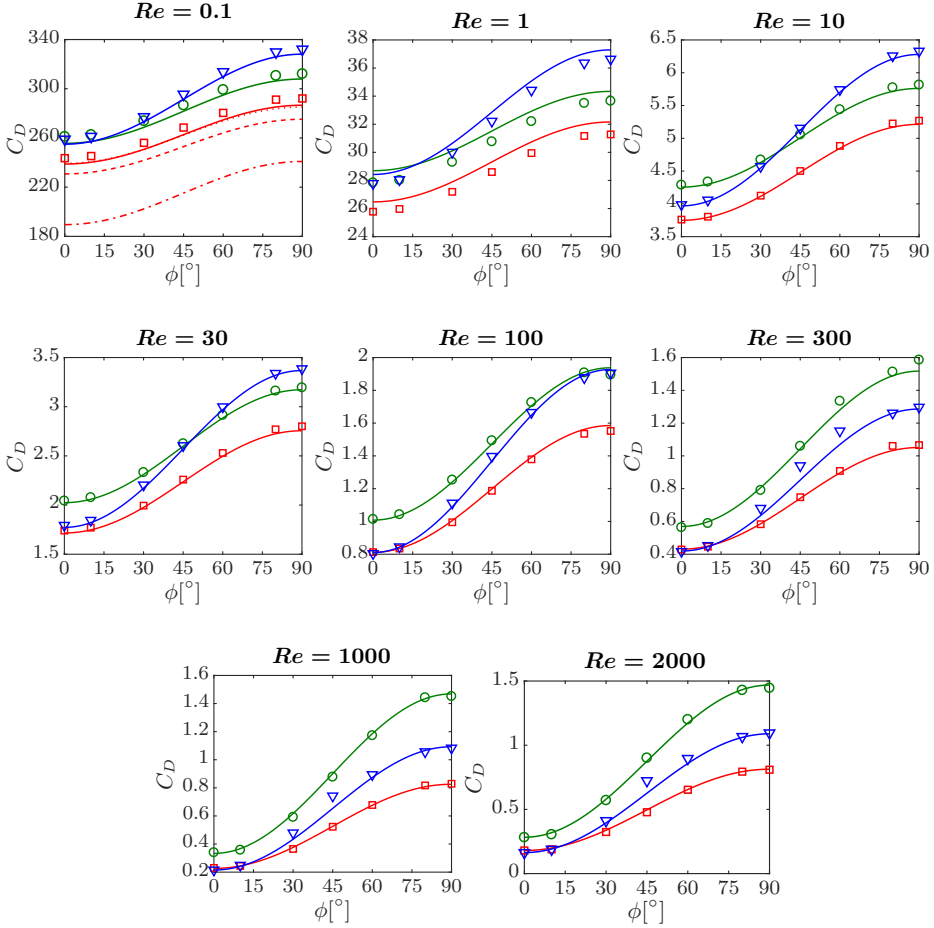
Figure 4.9: C_D vs ϕ at different Re for ellipsoid 1 (□), ellipsoid 2 (○), and fibre (▽). The corresponding solid lines in respective colors indicate the fit. At $Re = 0.1$ for ellipsoid 1, the dashed line corresponds to theory (Happel & Brenner, 1983), dashed-dot line for Zastawny *et al.* (2012) and dotted lines for Ouchene *et al.* (2016).
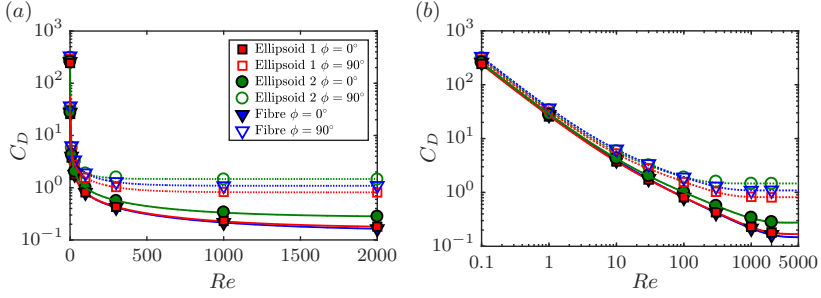
Figure 4.10: C_D against Re for different non-spherical particles with Re in (a) linear scale and (b) log-scale. The corresponding C_D correlations fit at $\phi = 0°$ (solid lines) and $\phi = 90°$ (dotted lines) are also shown.

	Ellipsoid 1		Ellipsoid 2		Fibre	
	$\phi = 0°$	$\phi = 90°$	$\phi = 0°$	$\phi = 90°$	$\phi = 0°$	$\phi = 90°$
a_1	23.10	27.93	24.66	30.18	24.48	31.89
a_2	3.397	4.286	4.059	4.396	3.965	5.519
a_3	0.364	0.234	0.349	0.156	0.41	0.229
a_4	0.0008	0.0018	0.0007	0.0073	0.0005	0.0032
a_5	0.169	0.815	0.278	1.469	0.15	1.089

Table 4.2: Coefficients for the C_D correlation.

	Ellipsoid 1	Ellipsoid 2	Fibre
Mean(%)	1.48	1.66	2.18
Max.(%)	5.23	4.52	13.38

Table 4.3: Relative deviation between C_D results and the correlation.

Stokes flow, irrespective of the particle shape. In our form, the term a_1/Re replicates this behaviour. For intermediate Re, the term a_2/Re^{a_3} is dominant. Additionally, it is known that for a sphere, the C_D decays to a near constant value at large $Re > 10^3$ (see figure 4.6). Similar behaviour is observed for the different tested non-spherical particles and the term a_5 captures the near constant C_D at high Re (see figure 4.10). Appropriately, the factors $e^{-a_4 Re}$ and $1 - e^{-a_4 Re}$ act as a smooth switch between these moderate and high Re regimes. Figure 4.10 shows the C_D values at $\phi = 0°$ and $\phi = 90°$ for different Re. With the proposed functional form for the correlation, the decay rate of C_D with respect to Re is captured well and therefore, we suggest that the C_D correlation can be extended to much lower Re in the Stokes regime and also to a few thousand Re magnitude greater than our simulations. To demonstrate this, figure 4.10(*b*) is shown with the fit from equation 4.15 upto $Re = 5000$ and it can observed that the trends are captured well for Re greater than the simulated limit of $Re = 2000$. Further, we show that the proposed C_D correlations are very accurate with respect to the measured coefficients and the same can be observed from figure 4.9. The mean and the maximum of the deviations between the C_D correlations and the actual results are listed in table 4.3. It can be observed that the mean of the absolute deviations are around 2% or less.

For creeping flows, it is known that the viscous forces dominate and the viscous forces themselves are dependent on the surface area of the particle. Conversely, for high Re, the pressure forces dominate and the pressure forces themselves are predominantly dependent on the projected surface area against the oncoming flow. This can also be observed in our simulations on comparison of C_D at $Re = 0.1$ and $Re = 2000$ in figure 4.9. For $Re = 0.1$, it is seen that the C_D of the fibre at different ϕ is at least equal or greater than that of disc-like ellipsoid 2. However at $Re = 2000$, we observe that the disc-like ellipsoid 2 has C_D values larger than that of the fibre.

STEADY AND UNSTEADY REGIMES

The triggering of unsteady behaviour from a steady flow regime for a non-spherical particle depends not only on the Re but also on the incident an-
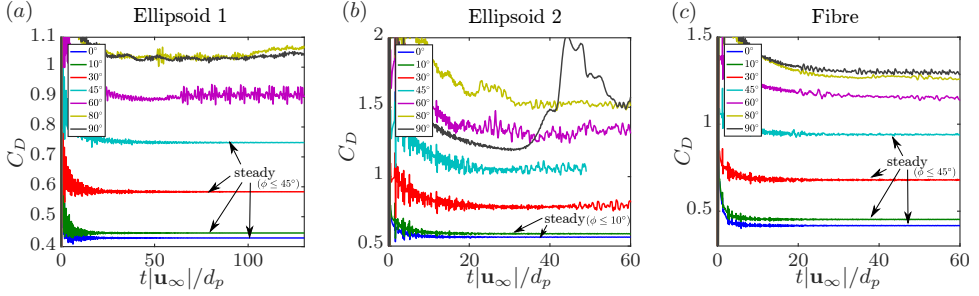
Figure 4.11: Time dependent behaviour of C_D at different incident angles ϕ at $Re = 300$ for (a) ellipsoid 1, (b) ellipsoid 2 and (c) fibre.

gle ϕ. For a 6:1 prolate spheroid, Jiang *et al.* (2014) investigated the flow at a specific inclination of $\phi = 45°$ at approximately $Re = 91, 363$, and 1817 ($Re_d = 50, 200$, and 1000 respectively). They report that even at $Re = 1817$, the flow exhibits predominantly steady and symmetric behaviour with the measured force coefficients exhibiting steady behaviour, with a mention that the flow field is on the verge of exhibiting vortex shedding behaviour for higher Re. These results are contrasting with the work of El Khoury *et al.* (2012) where the same prolate spheroid of ratio 6:1 is investigated at $91 \leq Re \leq 545$ ($50 \leq Re_d \leq 300$ respectively), but at cross-flow with $\phi = 90°$. They observe that unsteady behaviour is triggered at Reynolds numbers as low as $Re \approx 182$ ($Re_d = 100$). Therefore, we can say that the incident angle ϕ plays a major role in triggering unsteadiness. The simulations are run for a sufficiently large time $t_* = |\boldsymbol{u}_\infty| t / d_{eq}$, specifically for Re expected to exhibit unsteady regimes.

At $Re \leq 100$, all three tested particles show steady flow behaviour for all ϕ. However at $Re = 300$, the particles show unsteady behaviour for certain angles. Figure 4.11 shows the time-dependent drag of different non-spherical particles at $Re = 300$. It can be observed that the ellipsoid 1 and the fibre, both slender objects, exhibit steady behaviour for $\phi \leq 45°$ and unsteady behaviour for higher ϕ. However, the disc-like ellipsoid 2 exhibits steady behaviour only for low incident angles, i.e. $\phi \leq 10°$ and unsteady behaviour at higher incident angles. At higher $Re = 1000$, both the ellipsoid 1 and the fibre exhibit steady behaviour until $\phi \leq 10°$ and ellipsoid 2 exhibits unsteady behaviour for all ϕ. At $Re = 2000$, all particles exhibit unsteady behaviour for all incident angles ϕ, except for the fibre at $\phi = 0°$.
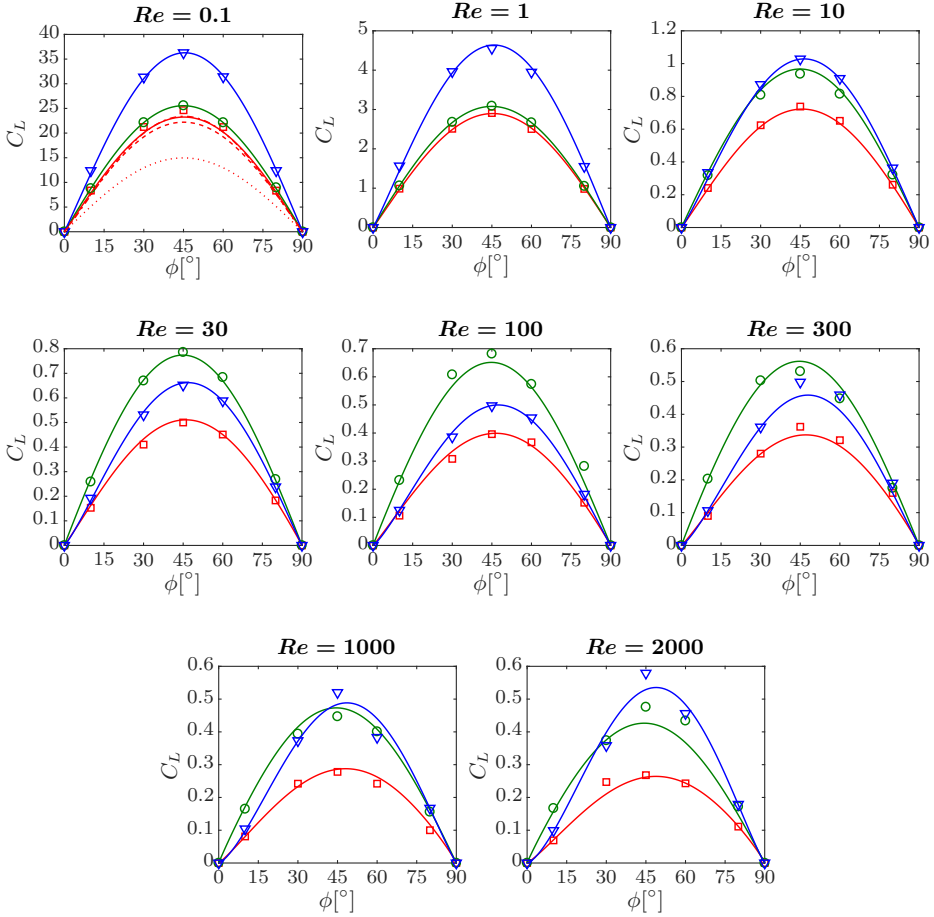
Figure 4.12: C_L vs ϕ at different Re for ellipsoid 1 ($\square$), ellipsoid 2 ($\circ$), and fibre ($\triangledown$). The corresponding solid lines in respective colors indicate the fit. At $Re = 0.1$ for ellipsoid 1, the dashed line corresponds to theory (Happel & Brenner, 1983), dashed-dot line for Zastawny *et al.* (2012) and dotted lines for Ouchene *et al.* (2016).

4.3.2. Lift

The lift coefficients C_L of the different tested particles and the corresponding correlation fits are plotted in figure 4.12. The proposed C_L fit takes the following form

$$C_{L,\phi} = \left(\frac{b_1}{Re} + \frac{b_2}{Re^{b_3}} + \frac{b_4}{Re^{b_5}}\right) \sin\phi^{(1+b_6 Re^{b_7})} \cos\phi^{(1+b_8 Re^{b_9})} \tag{4.16}$$

with the coefficients listed in table 4.4. The proposed C_L correlation form has both sine and cosine terms approaching exponent 1 for low Re, because this is the exact physical limit for Stokes flow (Happel & Brenner, 1983). As equation 4.6 is valid for Stokes flow, the corresponding $1/Re$ term of the C_L fit is dependent on the C_D, i.e. $b_1 \approx a_1(\phi = 90°) - a_1(\phi = 0°)$.

The mean and the maximum of the deviations between the C_L results and the fit are listed in table 4.5. The proposed correlation fits the observed results with good agreement with around 3-4% mean deviation. It is difficult in general to achieve a better fit due to the fact that the order of magnitudes of C_L are smaller than C_D and any small deviation is amplified. There is also a trend reversal in the skewness of the C_L vs ϕ curve for increasing Re. At Stokes flow, the C_L at different ϕ is symmetric. With increasing Re, up to the steady limits i.e. around $Re = 300$, the distribution skews to a particular direction and upon onset of unsteady behaviour, the skewness changes direction. This is observed for ellipsoid 1 and ellipsoid 2. Ellipsoid 1 results skew to the right upto $Re = 300$ and to the left for higher Re and vice versa for ellipsoid 2.

In general, the maximum C_L generated at a given Re is a function of the particle aspect ratio itself and also of the projected area of the particle at $\phi = 45°$. For the same reason, even though both ellipsoids 1 and 2 are of same aspect ratio, the disc-like ellipsoid 2 always experiences more lift than the needle-like ellipsoid 1. Interestingly the fibre, which has aspect ratio 4, experiences the highest lift both in the Stokes regime and at $Re = 2000$ among the 3 tested particles. However at intermediate $Re = 100$, the disc-like ellipsoid 2 experiences maximum lift until the Re corresponding to onset of the unsteady flow. This is due to the fact that at intermediate Re, the disc-like ellipsoid 2 experiences stronger wake (compared to an elongated ellipsoid) at intermediate angles and this increases C_L directly. By stronger wake, we imply that the wake size is large and proportional to the projected area of the particle against the flow. Another interesting observation is that the maximum C_L of the fibre monotonously reduces with increasing Re like other non-spherical particles. However after a critical Re, the trend reverses and the maximum C_L starts to increase again compared to other particles (see figure 4.12).

	Ellipsoid 1	Ellipsoid 2	Fibre
b_1	4.484	5.28	6.83
b_2	1.326	8.96	0.071
b_3	0.122	0.234	−0.352
b_4	0	−8.095	2.592
b_5	0	0.325	0.298
b_6	0.016	−0.004	0.065
b_7	0.286	0.352	0.262
b_8	−0.010	−0.002	0.003
b_9	0.332	0.273	0.491

Table 4.4: Coefficients for the C_L correlation. The near zero coefficients should not be ignored as they would influence C_L at high Re.

	Ellipsoid 1	Ellipsoid 2	Fibre
Mean(%)	3.73	3.50	3.60
Max.(%)	18.54	20.86	15.74

Table 4.5: Relative deviation between C_L results and the correlation. It should be noted that the maximum relative deviations are observed at incident angles ϕ with C_L close to zero, i.e. ϕ near 0° and 90°.
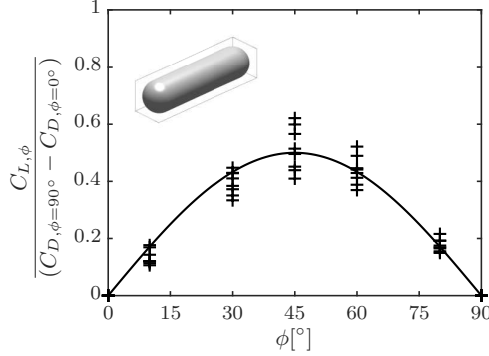
Figure 4.13: The normalized lift coefficient $C_{L,\phi}/(C_{D,\phi=90°} - C_{D,\phi=0°})$ for the fibre plotted against ϕ for different Re from 0.1 up to 2000. The solid line indicates $\sin\phi\cos\phi$. It should be noted that the used C_D and C_L values are from the simulations and not from the correlations.

Even though equation 4.6 is only valid in the Stokes regime, we find that the same equation can be used as a reasonable approximation at higher Re, *specifically* for smooth, elongated particles. Examples of smooth, elongated particles include prolate spheroids, spherocylindrical capsules, etc. Sufficient care has to be exercised on applying equation 4.6 to shapes such as simple cylinders due to their sharp edges, as sharp edges might affect flow pattern and evolution of the instabilities significantly. However for high aspect ratio elongated cylinders, the influence of these sharp edges would be relatively weak compared to the frontal projected area of the particle for different ϕ. Equation 4.6 has been tested by us for different slender particles such as the prolate spheroids of different aspect ratios upto $Re = 2000$ (Sanjeevi & Padding, 2017). The mean of deviations between the simulations and equation 4.6 is under 15%. In this work, we also show that equation 4.6 can also be used for spherocylinders (fibres) as a decent approximation. Figure 4.13 shows the distribution of normalized C_L for the fibre at different Re upto 2000.

At the same time, it is interesting to note that a similar observation does not hold for disc-like oblate spheroids. Ellipsoid 2 in this work tested for $Re \leq 2000$ does not exhibit this behaviour. Another, flatter oblate spheroid of aspect ratio 4 has been tested by us at $Re = 100$ (Sanjeevi & Padding, 2017). The same oblate spheroid also does not exhibit the reasonable approximation of equation 4.6. The disc-like spheroids in general experience stronger wake compared to needle-like spheroids at Re beyond the Stokes regime. The stronger wake translates to larger lift at intermediate incident angles ϕ and thereby making the deviation larger for oblate spheroids (Sanjeevi & Padding, 2017). However in the ab-
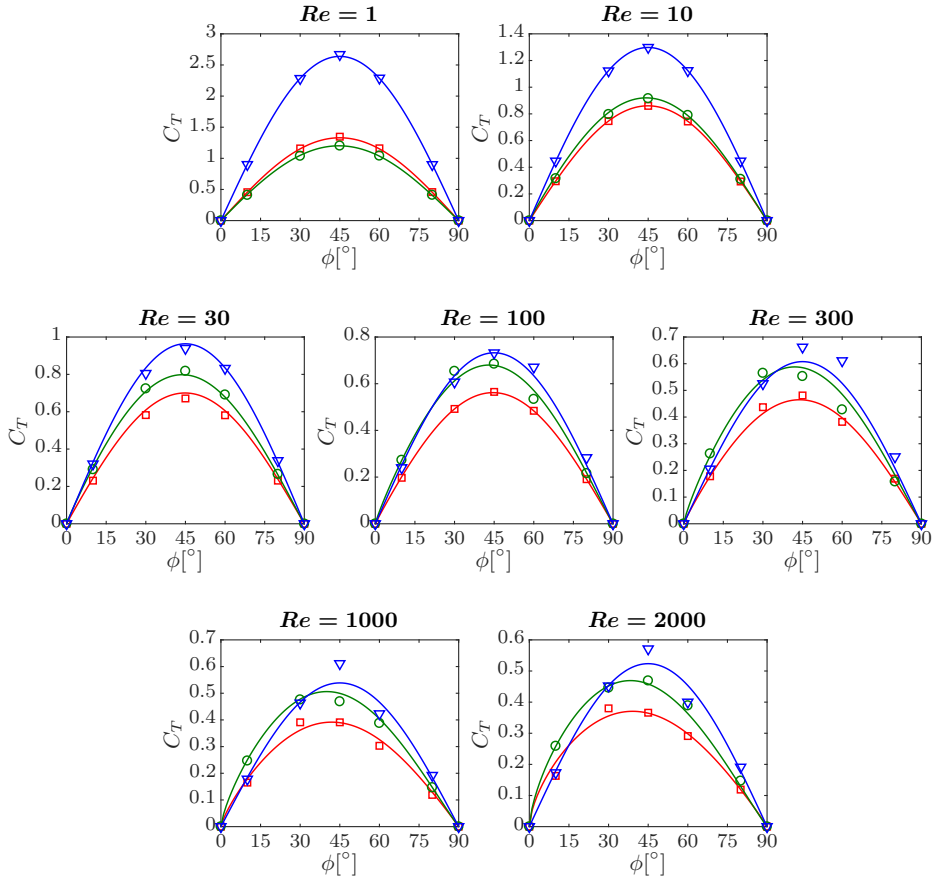
Figure 4.14: C_T vs ϕ at different Re for ellipsoid 1 ($\square$), ellipsoid 2 ($\circ$), and fibre ($\triangledown$). It has to be noted that torque vanishes in Stokes flow and therefore ignored for the correlation.

sence of complete C_L data, equation 4.6 could still be used for oblate spheroids as an approximation.

4.3.3. TORQUE

Any non-spherical particle inclined with respect to a homogeneous flow also experiences a pitching torque. The torque coefficient C_T from the simulations and the correlation fits are plotted in figure 4.14. For Stokes flow, the pitching torque is known to vanish. Therefore, the Stokes regime C_T results are ignored while making the fit. The proposed C_T correlation fitted for the range $1 \leq Re \leq 2000$

	Ellipsoid 1	Ellipsoid 2	Fibre
c_1	2.660	3.643	5.079
c_2	0.190	0.178	0.342
c_3	0	-1.252	0.197
c_4	0	0.319	-0.161
c_5	-8.73×10^{-4}	-0.018	0
c_6	0.798	0.387	0
c_7	-3.70×10^{-5}	0.004	0
c_8	0.963	0.349	0

Table 4.6: Coefficients for the C_T correlation. The near zero coefficients should not be ignored as they would influence C_T at high Re.

	Ellipsoid 1	Ellipsoid 2	Fibre
Mean(%)	3.40	3.43	4.12
Max.(%)	27.30	15.13	17.18

Table 4.7: Relative deviation between C_T results and the correlation. The maximum relative deviations are observed at incident angles ϕ with C_T close to zero, i.e., near 0° and 90°.

takes the following form

$$C_{T,\phi} = \left(\frac{c_1}{Re^{c_2}} + \frac{c_3}{Re^{c_4}} \right) \sin\phi^{(1+c_5 Re^{c_6})} \cos\phi^{(1+c_7 Re^{c_8})} \tag{4.17}$$

with coefficients listed in table 4.6. Similar to C_L, the C_T values exhibit near symmetric behaviour and vanish to zero at the extreme incident angles ϕ and therefore, the fitted correlation is very sensitive to minor deviations. The mean and maximum deviations of the correlation for the different tested particles are listed in table 4.7. Even though good agreements are observed in figure 4.14, the overall mean relative deviation is around 3.5%. This mainly stems from larger relative deviations for the near-zero C_T values observed close to $\phi = 0°$ and $\phi = 90°$.

4.4. COMPARISON WITH LITERATURE CORRELATIONS

In this section, we compare our simulation results with different correlations available in the literature. Hölzer & Sommerfeld (2008) provide only a C_D correlation, but it is applicable to arbitrary non-spherical particles. We use it at $\phi = 0°, 90°$ and interpolate for intermediate incident angles ϕ using equation
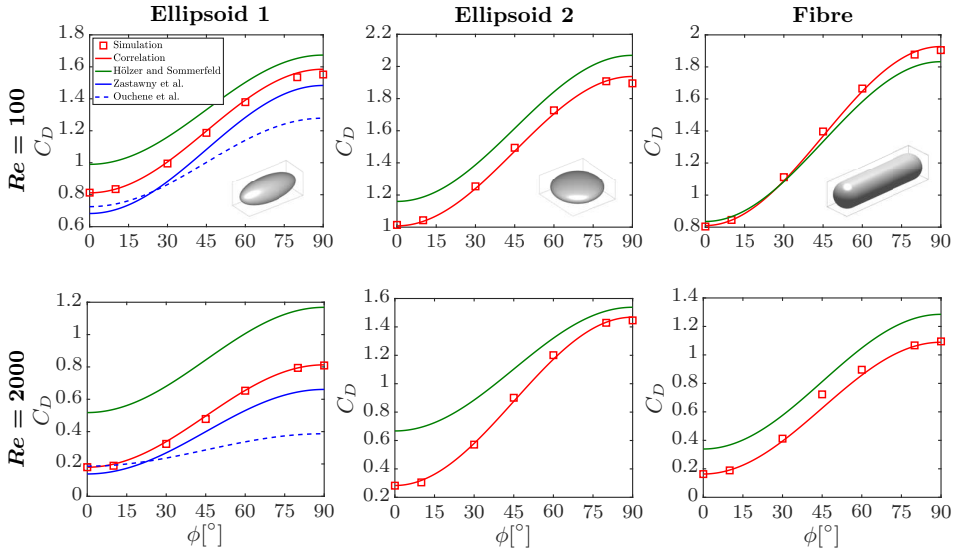
Figure 4.15: Comparison of C_D results with literature correlations.

4.14 as all tested particles exhibit near sine-squared C_D behaviour for all Re. Zastawny *et al.* (2012) and Ouchene *et al.* (2016) provide C_D, C_L and C_T for specific non-spherical particles limited to steady flows. The provided correlations have different decay rates for different Re regimes. If such decay rates are captured accurately, it is possible that their correlations can be extended to ranges beyond their tested limits. It is shown in figure 4.1 that the fluidized particles experience flows upto $Re = 2000$. In this section, we therefore test the correlations of both Zastawny *et al.* (2012) and Ouchene *et al.* (2016) upto $Re = 2000$, even though their tested Re regime is roughly an order of 10 less. Two cases are considered, one at $Re = 100$ and another at $Re = 2000$ and the corresponding drag, lift and torque coefficients are compared. At the moment of writing, we are not able to reproduce the C_D and C_L correlation results available in Ouchene *et al.* (2016) due to typographical errors in their published correlation. The corresponding typographical corrections have been communicated to us by Ouchene *et al.* (2016).

The C_D comparisons for the different non-spherical particles are shown in figure 4.15. For ellipsoid 1, we observe that our C_D results are in good agreement with Zastawny *et al.* (2012) for both $Re = 100$ and $Re = 2000$, even though their correlation is valid only up to $Re = 300$. However, the results of Zastawny *et al.* (2012) are not accurate for Stokes flow as can be observed from figure 4.9 for $Re = 0.1$ on comparison with theoretical solutions and other literature results. This is primarily due to the fact that Zastawny *et al.* (2012) use a domain of $20d_{eq} \times 20d_{eq} \times 10d_{eq}$ for $Re < 1$. Their lowest domain dimension $10d_{eq}$ is not sufficient
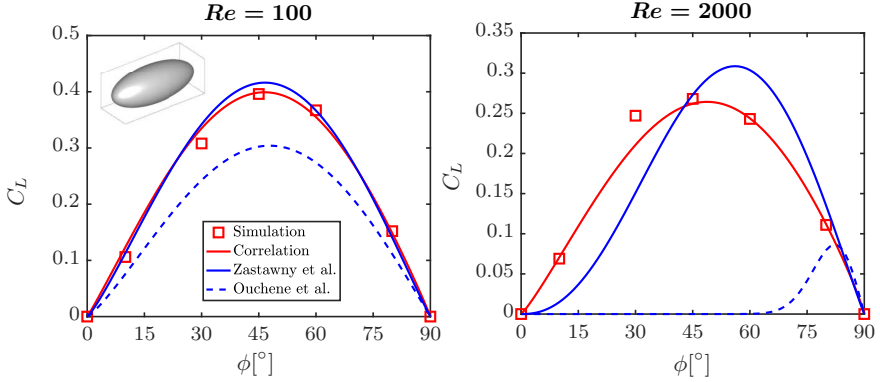
Figure 4.16: Comparison of C_L results of ellipsoid 1 with literature correlations.

for Stokes flow, where viscous effects are dominant and thereby requiring larger domain size.

On the other hand, the more generic correlation of Ouchene *et al.* (2016) for different prolate spheroids is comparatively less accurate. While their $C_{D,\phi=0°}$ is found to be sufficiently accurate, the $C_{D,\phi=90°}$ is not accurate, thereby leading to an inaccurate prediction overall with increasing Re. We find that the Hölzer & Sommerfeld (2008) correlation works reasonably well for all the tested non-spherical particles at $Re = 100$ but not well for $Re = 2000$. This is due to the fact that their correlation is intended to be more generically applicable to all non-spherical particles and for a wide range of Re. Further, the C_D itself reduces with increasing Re, with a rate that depends on the particle geometry. Therefore at high Re, any deviation is amplified due to the smaller C_D value.

The comparison of C_L values for ellipsoid 1 are given in figure 4.16. For $Re = 100$, we observe that our simulations results are in very good agreement with Zastawny *et al.* (2012). The results of Ouchene *et al.* (2016) exhibit large deviations, with a maximum deviation of around 40%. For $Re = 2000$, the results of Zastawny *et al.* (2012) are still reasonably accurate considering their tested limit is $Re = 300$. However, the C_L correlation of Ouchene *et al.* (2016) performs poorly at $Re = 2000$. As discussed earlier for C_D, if the coefficient decay rates are captured with proper physical bounds, the Re limits can be extended much further. In a similar sense, the C_L correlation of Ouchene *et al.* (2016) does not capture the decay rates accurately and also their skewness term $\sin^{1.002^{Re}}\phi\cos\phi$ makes the C_L skewness extreme for higher Re.

Generally, determining the particle correlations involves a two-step process: (i) performing accurate simulations and (ii) fitting the simulation results in an accurate form. The work of Ouchene *et al.* (2016) is performed using Ansys Flu-
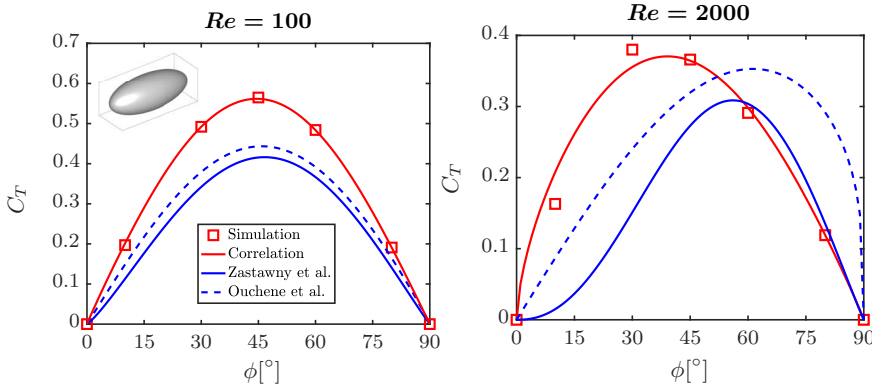
Figure 4.17: Comparison of C_T results of ellipsoid 1 with literature correlations.

ent, which is one of the most reliable commercial solvers and therefore, simulation accuracy is good. However, the choice of the fitting form is where most of the precision is lost, since the work of Ouchene *et al.* (2016) covers a wide range of aspect ratios, Re and incident angles. Even for a simple C_D correlation for a sphere, the accurate correlation forms (for example the Clift correlation) split the correlation into multiple Re range. For the same reason, we observe that C_D and C_L correlations of Ouchene *et al.* (2016) have poor accuracy (see figures 4.15 and 4.16) as they are done by a single fit. However, their C_T is found to be more accurate as it is split for two different aspect ratio ranges (see figure 4.17). Our work does not have this issue as the fits are independent for the different particles investigated and hence simpler.

Regarding C_T, the correlations of Zastawny *et al.* (2012) and Ouchene *et al.* (2016) are compared for ellipsoid 1 with our results in figure 4.17. We observe that both the literature results are in good agreement with our simulation results for $Re = 100$. At $Re = 2000$, there is still a reasonable match on comparing the maximum amplitudes of the C_T, but slight variation in the skewness. Our C_T distribution is slightly skewed to the left and the literature results slightly to the right. This is again due to the fact that the literature results are only performed for predominantly steady flow regimes with $Re \leq 300$.

4.5. CONCLUSION

The flow around different non-spherical particles has been simulated using the MRT-LBM scheme for different incident angles ϕ. Interpolated bounce-back is used to achieve high accuracy compared to the conventional staircase no-slip boundaries in LBM, especially at high Re. The simulations have been performed

from the Stokes limit to $Re = 2000$, while previous works were mainly limited to steady flows up to $Re = 300$. Different tests have been performed to assess the influence of grid resolution and also the size of the domain, thereby ensuring the quality of the results. The influence of the particle's geometry and also the incident angle ϕ has a significant effect on the onset of unsteady flow behaviour. We observed that the simulated particles exhibit sine-squared mean drag scaling with ϕ, starting from the Stokes limit and even upto $Re = 2000$. Such an agreement at high Re is not due to linearity of the flow fields as in Stokes flow, but rather due to consistent pressure pattern depending on local surface normal of the particle (Sanjeevi & Padding, 2017).

At the same time, we observed that the lift and torque coefficient display a symmetric behaviour at Stokes flow and a slightly skewed trend for larger Re. The onset of unsteady flow behaviour also influences the direction of the skewness i.e. different skewing directions before and after the transient Re for unsteady flow behaviour. Correlations for drag, lift and torque coefficients have been proposed, taking in consideration of known theoretical limits at low Re and different decay rates at high Re. This implies that our correlations can be extended to regimes beyond our tested limits, to lower Re in the Stokes regime and $Re > 2000$ to a considerable extent, especially the correlations of C_D and C_L. We also propose that in the absence of complete C_L data for intermediate incident angles ϕ, the C_L equation of the Stokes flow (equation 4.6) can be used as a reasonable approximation at high Re. Better agreement is observed for smooth, elongated particles such as prolate (needle-like) spheroids and spherocylindrical fibres compared to oblate (disc-like) spheroids. The reason why disc-like spheroids show poor agreement is due to increased lift at intermediate incident angles ϕ due to stronger wake (Sanjeevi & Padding, 2017).

Good agreement between the measured data and the fits is observed, with deviations of around 2% for C_D and around 3.5% for C_L and C_T. The proposed correlations will greatly help Euler-Lagrangian simulations, catering the practical Re regimes observed in fluidized beds.

HYDRODYNAMIC FORCES AND TORQUE ON ASSEMBLIES OF NON-SPHERICAL PARTICLES

This chapter provides a recipe for creating closures of average drag, lift and torque for static assemblies of axisymmetric, non-spherical particles. Apart from Reynolds number Re and solids volume fraction ϵ_s, we propose four additional parameters to characterize the flow through non-spherical particle assemblies. Two parameters consider the mutual orientations of particles (the orientation tensor eigenvalues S_1 and S_2) and two angles represent the flow direction (polar and azimuthal angles α and β). Interestingly, we observe that the hydrodynamic forces on the particles are independent of the mutual particle orientations. Rather, the most important parameter representing the particle configuration itself is the incident angle φ of the individual particles with respect to the incoming flow. Moreover, we observe that our earlier finding of sine-squared scaling of drag for isolated particles (Sanjeevi & Padding, 2017) holds on average even for a multiparticle system in both the viscous and inertial regimes. Similarly, we observe that the average lift for a multiparticle system follows sine-cosine scaling, as is observed for isolated particles. Such findings are very helpful since the pressure drop of a packed bed or porous media can be computed just with the knowledge of orientation distribution of particles and their drag at φ = 0° and φ = 90° for a given Re and ϵ_s. With the identified dependent parameters, we propose drag, lift and torque closures for multiparticle systems.

5.1. Introduction

Accurate fluid-particle drag, lift and torque closures are required for precise Euler-Lagrangian simulations of non-spherical particles. Historically, different drag closures have been developed for assemblies of spherical particles (Beetstra *et al.*, 2007; Tenneti *et al.*, 2011; Tang *et al.*, 2015). However, practical flows often involve assemblies of non-spherical particles for which there exist no closures at the moment. Even for static, mono-disperse, non-spherical particle assemblies, creating the required closures is complicated due to the different possible mutual orientations of the particles. Furthermore, there is a lack of knowledge identifying the relevant parameters that can parametrize the drag, lift and torque, which adds to the complication. Most fluidization applications involve gas-solid flows, in which case the large density ratios ensure large Stokes numbers, i.e. the typical relaxation time of the solid particle velocity is large relative to the response time of the gas (Sanjeevi *et al.*, 2018*a*). It has been shown that under such conditions, it is sufficient to assume the particle configurations to be quasi-static (Rubinstein *et al.*, 2017).

Conventionally, fluidization simulations of non-spherical particles are performed by combining isolated particle drag correlations with correlations expressing the voidage effects as determined for sphere assemblies. There have been several works in the past focussing on the drag experienced by isolated non-spherical particles. Hölzer & Sommerfeld (2008) proposed a correlation for the drag coefficient C_D for non-spherical particles. The proposed correlation is a function of particle sphericity and crosswise-sphericity, based on the projected area, which indirectly represents the particle orientation. Their proposed correlation is based on literature data of different non-spherical particles of various shapes and aspect ratios. More recently, drag, lift and torque closures for isolated non-spherical particles have been derived based on direct numerical simulations. Zastawny *et al.* (2012) developed drag, lift and torque coefficients for four different non-spherical particles as a function of Reynolds number Re and incident angle ϕ with respect to the incoming flow. The investigated particles have aspect ratios ranging from 1.25 to 5 and $Re \leq 300$. Similarly, Richter & Nikrityuk (2013) proposed fits for drag, lift, torque coefficients for cubic and ellipsoidal particles. The above mentioned literature is primarily limited to steady flow conditions. Recently, we developed drag, lift and torque closures for three different non-spherical particles from the viscous Stokes regime upto the high Re regime of $Re = 2000$, involving complex, unsteady flows (Sanjeevi *et al.*, 2018*a*). In an earlier work (Sanjeevi & Padding, 2017), we reported the interesting finding that the drag coefficient C_D at different incident angles ϕ follows a sine-squared

scaling given by

$$C_{D,\phi} = C_{D,\phi=0°} + (C_{D,\phi=90°} - C_{D,\phi=0°}) \sin^2 \phi. \tag{5.1}$$

Likewise, we reported another interesting finding that the lift coefficient C_L follows sine-cosine scaling at different ϕ as

$$C_{L,\phi} = (C_{D,\phi=90°} - C_{D,\phi=0°}) \sin\phi \cos\phi \tag{5.2}$$

for various elongated particles. The above mentioned scaling laws must be mathematically true in the Stokes regime due to linearity of the flow fields. However, their validity in the inertial regimes is primarily due to an interesting pattern of pressure distribution contributing to the drag and lift for different incident angles (Sanjeevi & Padding, 2017). In equations 5.1 and 5.2, the drag coefficients at incident angles of 0 and 90 degrees still depend on particle shape and Reynolds number. The Reynolds number in the present work is defined as $Re = |\boldsymbol{u}_s| d_{eq} / \nu$, where $\boldsymbol{u}_s$ is the superficial flow velocity, ν is the kinematic viscosity of the fluid, and d_{eq} is the diameter of the volume-equivalent sphere given by $d_{eq} = (6V_p/\pi)^{1/3}$ with V_p the particle volume.

For multiparticle systems, various literature is available to include the voidage effects, often developed through experiments and numerical simulations. One of the most widely used expressions is that of Ergun (1952), which has been developed based on a series of packed bed experiments of different particle shapes. The only limitation of this work is that it is applicable primarily in the dense limit. Richardson & Zaki (1954) performed various sedimentation and fluidization experiments and proposed accordingly the effect of particle volume fraction on the drag. Based on the previous literature on sedimentation and packed bed experiments, Di Felice (1994) bridged the dilute and dense particulate regimes through a unified function, which also extends from low to high Re. Though the above correlations provide a good approximation, the use of such closures in Euler-Lagrangian simulations often do not represent accurate physics. This is mainly due to the inability to construct moderate solids volume fractions ($\epsilon_s \approx 0.3$) in experiments.

There is a growing interest to use numerical simulations to accurately develop drag closures for different Reynolds numbers Re and solids volume fractions ϵ_s, albeit primarily for spheres. Initially, lattice Boltzmann method (LBM) has been the choice for simulating assemblies of spheres (Hill *et al.*, 2001; van der Hoef *et al.*, 2005; Beetstra *et al.*, 2007). Recently, Tenneti *et al.* (2011) used an immersed boundary method (IBM) to develop drag closures for static assemblies of spheres for $0.01 \leq Re \leq 300$ and $0.1 \leq \epsilon_s \leq 0.5$. They observed a deviation of 30% in the Re range from 100 to 300 with respect to the earlier work of Beetstra *et al.*

(2007). This is possible because Beetstra *et al.* (2007) used LBM with the conventional stair-case boundary condition to represent the sphere boundaries, for which at high Re thinner boundary layers result in larger deviations. In this work, we use a multi-relaxation time (MRT) LBM for high Re flows and an interpolated bounceback scheme to much more accurately represent the particle geometry. Recently, Tang *et al.* (2015) used an IBM based solver to create drag closures for static assemblies of spheres upto $Re \leq 1000$ and $\epsilon_s \leq 0.6$.

There are several disadvantages with combining an isolated non-spherical particle drag with a voidage function based on spheres. First, the assumption that the voidage effects are independent of particle shape is probably incorrect, since there exist different closures even for assemblies of polydisperse spheres (Beetstra *et al.*, 2007; Holloway *et al.*, 2010). Second, the voidage effects on lift and torque in a multiparticle system are unknown and hence are often neglected in Euler-Lagrangian simulations (Oschmann *et al.*, 2014; Mahajan *et al.*, 2018). Thirdly, using the same factor for voidage effects for all incident angles ϕ may hold in sufficiently dilute regimes but its validity in the dense limit is unknown. At the moment, only He & Tafti (2018) have discussed the drag, lift and torque for an assembly of non-spherical particles. However, they do not propose any correlations which can be used in Euler-Lagrangian simulations. This could be due to the difficulty in identifying the dependent parameters which represent the orientation effects in non-spherical, multiparticle system adequately.

In this work, we propose and subsequently identify the important dependent parameters for static, mono-disperse assemblies of axisymmetric non-spherical particles. With the identified parameters, we create the drag, lift and torque closures accordingly. Our particle of interest is a capsule-like spherocylinder of aspect ratio 4 (total length/shaft diameter). Compared to the two parameters for sphere assemblies, i.e. Reynolds number Re and solids volume fraction ϵ_s, we propose four additional parameters for the assembly of axisymmetric non-spherical particles. Two parameters describe the mutual orientations of the particles, namely two eigenvalues S_1 and S_2 of the orientation tensor, and two angle parameters α and β represent the polar and azimuthal angles of the average flow (in the coordinate frame determined by the principal directions of the order tensor). The resulting six dimensional parameter space is adequately explored and correlations are proposed accordingly. It should be noted that the fixed nature of the particles in our simulations imply that the proposed correlations are applicable for high Stokes number flows as typically experienced by Geldart D category particles (Geldart, 1973).

Re	L_D	d_{eq}	ν
$0.1 \leq Re \leq 10$	288	$28.36 - 48.5$	$1.3/3$
$10 < Re \leq 100$	576	$56.72 - 97.0$	0.1 to $0.08/3$
300	576	$56.72 - 97.0$	$0.04/3$
600	576	$56.72 - 97.0$	$0.015/3$
1000	768	$75.63 - 129.3$	$0.01/3$

Table 5.1: Details of the simulation parameters used in our simulations in LB units. L_D denotes the side length of the cubic domain. The range of d_{eq} specified is respectively for $0.1 \leq \epsilon_s \leq 0.5$.

5.2. SIMULATION SETUP

The numerical method is adequately explained and validated in our previous works (Sanjeevi & Padding, 2017; Sanjeevi *et al.*, 2018*a*). The flow is driven by a body force $\boldsymbol{g}$ and the simulated cubic domain is periodic in all three directions. The use of the interpolated bounce back scheme within a periodic domain results in a slow mass leakage/gain in the system. Accordingly, the mass is corrected using a case 3 type correction described in Sanjeevi *et al.* (2018*b*). The results for the multiparticle system are validated in section 5.2.5.

The ratio of d_{eq}/d_{min} equals 1.765 for the considered spherocylinder of aspect ratio 4, where d_{min} implies diameter of the cylinder. The simulation parameters used in our LBM simulations are summarized in table 5.1. Specifically, it can observed that a good particle resolution (d_{eq}) is maintained for different Re. Further with increasing ϵ_s, the d_{eq} is increased accordingly to resolve increased velocity gradients at high ϵ_s. All LBM simulations have cubic domain, each with 200 particles unless otherwise specified. At least two independent simulations are performed for each Re and ϵ_s and the details of independent number of simulations are discussed later (see figure 5.13).

5.2.1. FLOW CONTROL

In order to perform a simulation for a specific Re, it is required to control the superficial flow velocity $\boldsymbol{u}_s$ by applying a body force $\boldsymbol{g}$. The relationship between the superficial velocity and the average interstitial flow velocity $\boldsymbol{u}_{avg}$ is given by $\boldsymbol{u}_s = (1 - \epsilon_s)\boldsymbol{u}_{avg}$. Due to the non-spherical nature of the particles, the sum of lift forces is often non-zero, and the resultant direction of $\boldsymbol{u}_s$ can be different from the direction of $\boldsymbol{g}$. This necessitates the need to control both direction and

$$
\begin{pmatrix} \frac{1}{3} & 0 & 0 \\ 0 & \frac{1}{3} & 0 \\ 0 & 0 & \frac{1}{3} \end{pmatrix}
\qquad
\begin{pmatrix} 0 & 0 & 0 \\ 0 & \frac{1}{2} & 0 \\ 0 & 0 & \frac{1}{2} \end{pmatrix}
\qquad
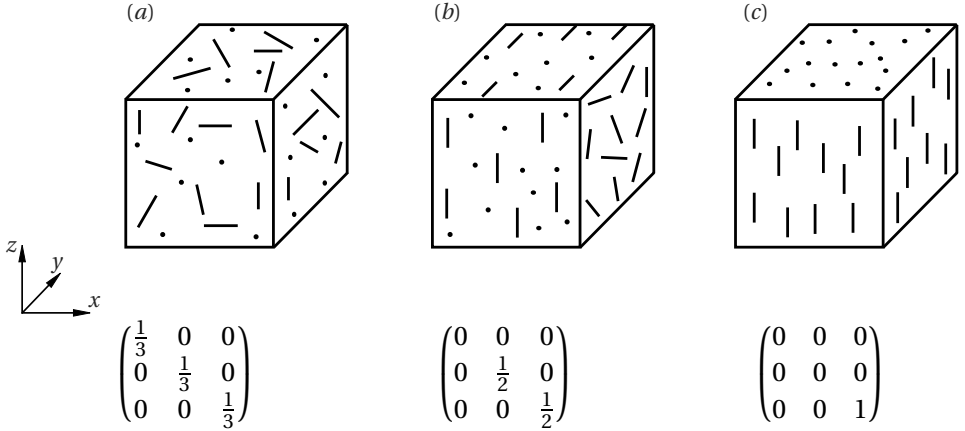\begin{pmatrix} 0 & 0 & 0 \\ 0 & 0 & 0 \\ 0 & 0 & 1 \end{pmatrix}
$$

Figure 5.1: Different particle configurations and their orientation tensors: (*a*) Random, (*b*) planar random, and (*c*) unidirectional (nematic) configuration.

magnitude of the body force. Initially, the fluid is at rest with both $\boldsymbol{u}_s$ and $\boldsymbol{g}$ zero. The flow is slowly ramped up by increasing $\boldsymbol{g}$ until the desired $\boldsymbol{u}_s$ is achieved. For each timestep, the updated gravity $\boldsymbol{g}_{new}$ is computed as

$$
\boldsymbol{g}_{new} = \boldsymbol{g}_{prev} + \frac{(\boldsymbol{u}_{s,ref} - \boldsymbol{u}_{s,prev})}{K_p^2} \Delta t, \tag{5.3}
$$

where $\boldsymbol{g}_{prev}$ is the gravity from the previous timestep, $\boldsymbol{u}_{s,ref}$ is the desired reference superficial velocity, and $\boldsymbol{u}_{s,prev}$ is the superficial velocity from the previous timestep. K_p is a time constant which controls the system response rate. The stopping criterion for the simulations is when the system $\boldsymbol{u}_s$ reaches 99.9% of the reference setpoint.

5.2.2. Orientation tensors

In this section, we briefly explain the characterization of mutual orientations in an assembly of axisymmetric non-spherical particles with orientation tensors. We subsequently explain the use of a Maier-Saupe potential to achieve the desired particle configurations through Monte-Carlo simulations.

To describe the orientation of a single axisymmetric particle, the azimuthal and polar angles are sufficient. For a multiparticle configuration, it is important to parametrize the mutual orientations of the particles, with the least number of parameters. For this, we propose to use the orientation tensor S which is defined as the average of the dyadic products of the particle orientation vectors. In other

words,

$$S = \langle \boldsymbol{p}\boldsymbol{p}^{T} \rangle. \tag{5.4}$$

Here, $\boldsymbol{p}$ is the unit orientation vector of a particle along the axis of symmetry. The 3 eigenvalues (which we order as S_1, S_2, S_3 from small to large) characterize the type of mutual alignment, as shown in figure 5.1. The corresponding 3 eigenvectors define the principal directions of mutual particle alignment.

Because the trace of S is 1, only 2 eigenvalues are sufficient to specify the amount of randomness, planar random (bi-axial), or unidirectional (nematic) order. It should be noted that the tensor S is insensitive to an orientation $\boldsymbol{p}$ or $-\boldsymbol{p}$ of particles. In other words, the tensor captures essentially the mutual alignment of particles irrespective of particles oriented in positive or negative direction. Figure 5.1(a) shows a completely random configuration with $S_1 = S_2 = S_3 = 1/3$. Figure 5.1(b) shows a planar random configuration with particles primarily confined to planes (in this example with random orientations in planes normal to the x-direction) resulting in $S_1 = 0, S_2 = S_3 = 1/2$, and similarly a unidirectional (nematic, in this example in the z-direction) configuration in figure 5.1(c) with $S_1 = S_2 = 0, S_3 = 1$. In practical conditions, particles can exhibit more complex configurations in between these extremes but can be adequately described by 2 eigenvalues S_1 and S_2. Regarding the unidirectional case, we consider only nematic configurations but not smectic because ordering of both positions and orientations is rare in fluidization conditions.

The above metrics can be used to describe the particle configuration. However, due to the nonsphericity of the particles, the flow orientation with respect to the principal directions of the particle orientations is also important. This results in two parameters, namely the polar angle (α) and azimuthal angle (β) of the average flow velocity vector with respect to the space spanned by the 3 eigenvectors of the orientation tensor. In summary, the parameter space to be explored for our flow problem has 6 parameters, namely Reynolds number Re, solids volume fraction ϵ_s, two particle configuration parameters S_1, S_2 and two angles α and β describing the mean flow orientation with respect to the configuration.

5.2.3. GENERATION OF BIASED PARTICLE CONFIGURATIONS

The generation of non-overlapping configurations of the particles in a periodic domain is required as an input for the flow simulations. Further, it is also required to generate configurations of particles with a prescribed orientation tensor, which adds further complexity. In this section, we briefly describe
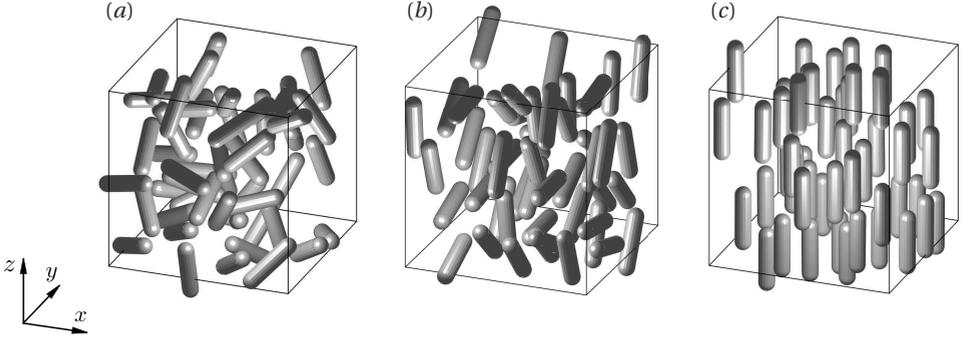
Figure 5.2: Different configurations of non-spherical particles generated us-
ing the Monte-Carlo simulations: (*a*) Random configuration without the use of
Maier-Saupe potential, (*b*) planar random, and (*c*) unidirectional configuration
generated using the Maier-Saupe potential. For better clarity, the shown exam-
ples have only 50 particles. The actual simulations involve 200 particles.

the Monte-Carlo simulation algorithm for generating configuration of non-
overlapping particles and the use of a Maier-Saupe potential (Maier & Saupe,
1959) to bias the system to produce the required orientation tensor.

As the particles are spherocylindrical in shape, a simple way to detect overlap
is to find the minimum distance between two line segments. We define the line
segment as the line connecting the centres of the two spheres at the extremes
of the spherocylinder. If the distance between two line segments is less than
the particle diameter (i.e. sum of the radii of two interacting particles), then the
spherocylinders overlap. A fast algorithm is used to measure the shortest dis-
tance between the line segments (Vega & Lago, 1994).

Using the above overlap detection algorithm, the particles are randomly
translated in small steps compared to the particle size and rotated by a small
angle around a randomly chosen axis. This procedure results in a random con-
figuration after many iterations. If a prescribed orientation tensor is required,
besides the requirement of no overlap, the following Maier-Saupe potential is
applied to accept or reject a new orientation of a particle. We define a director
$\boldsymbol{n}$ along which the system is biased towards or against. Inside each Monte-Carlo
simulation step, a new particle orientation $\boldsymbol{p}_{new}$ can be accepted or rejected
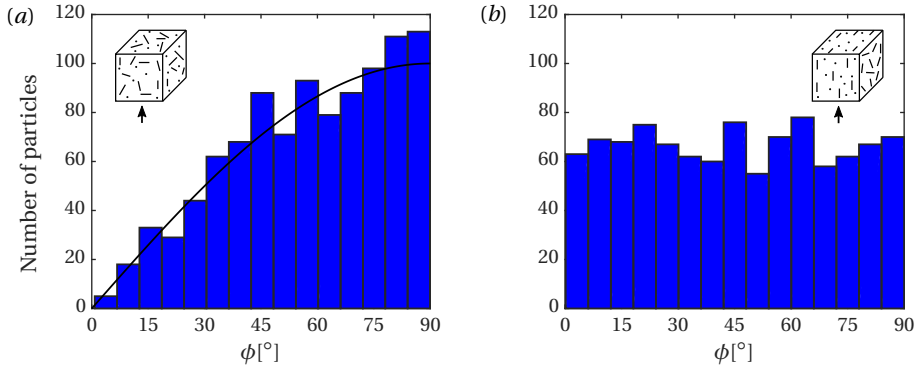
Figure 5.3: Histogram of particles with different incident angles ϕ with respect to the flow vector (indicated by an arrow) for (a) random and (b) planar random configuration. The shown example has 1000 particles. It should be noted that the ϕ distribution for a random configuration will always scale as $\sin\phi$ (solid black curve) irrespective of the flow direction.

from the current orientation $\boldsymbol{p}_{curr}$ based on following criteria:

$$\boldsymbol{p}_{new} = \begin{cases} \boldsymbol{p}_{new}, & \text{if } dE < 0 \\ \boldsymbol{p}_{new}, & \text{if } dE \geq 0 \text{ and } U([0,1]) < \exp(-dE) \\ \boldsymbol{p}_{curr}, & \text{otherwise} \end{cases} \tag{5.5}$$

where
$$dE = A((\boldsymbol{p}_{new} \cdot \boldsymbol{n})^2 - (\boldsymbol{p}_{curr} \cdot \boldsymbol{n})^2). \tag{5.6}$$

Here, dE is the increase in Maier-Saupe potential and $U([0,1])$ is a random number uniformly distributed between 0 and 1. The mutual particle orientations emerge from the balance between the random rotations, which tend to disorder the particle orientations, and the Maier-Saupe potential, which tend to order the particle orientations. The magnitude of A determines the intensity of the configuration towards the director. A planar random configuration is achieved with the plane perpendicular to the director $\boldsymbol{n}$, if A is positive. A unidirectional configuration along the direction of $\boldsymbol{n}$ is achieved, if A is negative. Higher absolute A values result in better perfection towards the desired configuration. With the mentioned strategy, any configuration in-between the ideal cases shown in figure 5.1 can be achieved. Some sample configurations generated using the above mentioned algorithm are shown in figure 5.2. For simplicity, the eigenvectors of the orientation tensor S are considered as aligned with the Cartesian coordinate system in figure 5.2. The shown configurations are respectively equivalent to figure 5.1. For better clarity, the shown configuration has only 50 particles and the solids volume fraction ϵ_s is 0.1. The actual flow simulations have 200 particles
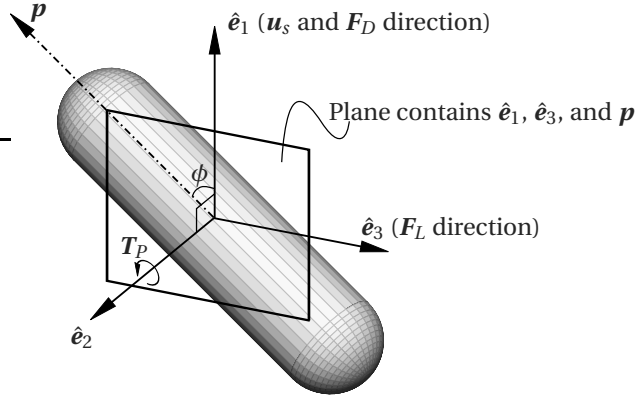
Figure 5.4: The local coordinate system of a particle. u_s and F_D act along $\hat{e}_1$, F_L along $\hat{e}_3$ and T_P about the $\hat{e}_2$ axis.

and are performed for various ϵ_s.

A common intuition may be that a random configuration would result in particles with evenly distributed values of the incident angle ϕ. However for a random configuration, the available number of particles at different ϕ are not uniform, as shown in figure 5.3(a). This is due to the higher probability to find particles at an angle ϕ near 90° because the Jacobian for a spherical coordinate system scales as $\sin\phi$. Therefore, the disadvantage for a random configuration is that there are actually few data points at $\phi = 0°$ to create angle-dependent closures. On the contrary, the planar configuration with the planes parallel to the flow direction results in even particle distributions, as shown in figure 5.3(b). This information is considered while we generate configurations for the flow simulations.

5.2.4. FORCES AND TORQUES ACTING ON A PARTICLE

For an assembly of particles, different definitions are used to report the forces (Beetstra *et al.*, 2007; Tenneti *et al.*, 2011; Tang *et al.*, 2015). To ensure consistency, it is important to know the form of the reported results. For a packed bed of particles in a flow induced by a macroscopic pressure gradient ∇P, each particle of volume V_p experiences a resulting force F due to the flow and a buoyancy force $F_b = -V_p \nabla P$ due to the pressure gradient. For such a case, the total fluid-to-particle force $F_{f \to p}$ acting on a particle is

$$F_{f \to p} = F + F_b. \tag{5.7}$$

Given N particles with each of volume V_p and total volume of the system V, the solids volume fraction is given by $\epsilon_s = N V_p / V$. Further, the relationship between
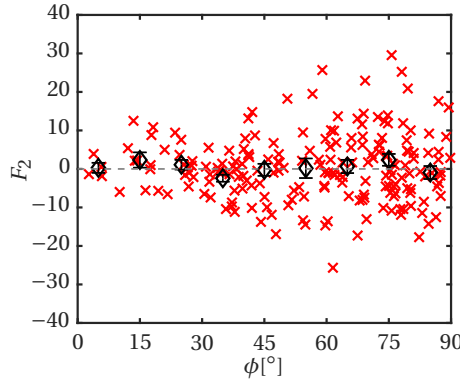
Figure 5.5: Lateral force F_2 distribution for different particles (×) with averages at regular ϕ intervals (◇) in a random configuration at $Re = 100$ and $\epsilon_s = 0.3$.

F and $F_{f \to p}$ is given by (Tang *et al.*, 2015)

$$F = F_{f \to p}(1 - \epsilon_s). \tag{5.8}$$

In this work, we report the forces F due to the flow and not $F_{f \to p}$. The effects of buoyancy on torques are unknown and hence the reported torques T are also as they are determined from the simulations. We normalize the force and torque with the Stokes drag and torque of a volume-equivalent sphere:

$$F_{norm} \quad = \frac{F}{6\pi\mu R_{eq}|u_s|}, \text{ and} \tag{5.9}$$

$$T_{norm} \quad = \frac{T}{8\pi\mu R_{eq}^2|u_s|}. \tag{5.10}$$

Here, μ is the dynamic viscosity and R_{eq} is the radius of the volume equivalent sphere. Let p be the normalized orientation vector of the considered particle. The local coordinate system for each particle is defined as

$$\hat{e}_1 \quad = \frac{u_s}{|u_s|}, \tag{5.11}$$

$$\hat{e}_2 \quad = \frac{\hat{e}_1 \times p}{|\hat{e}_1 \times p|} \text{sign}(\hat{e}_1 \cdot p), \text{ and} \tag{5.12}$$

$$\hat{e}_3 \quad = \hat{e}_1 \times \hat{e}_2. \tag{5.13}$$

The above defined axes are accordingly illustrated in figure 5.4. The incident angle ϕ a particle makes with respect to the incoming flow is given by $\phi = \cos^{-1}(|\hat{e}_1 \cdot p|)$. We also compute the average forces and torques for different ϕ intervals.

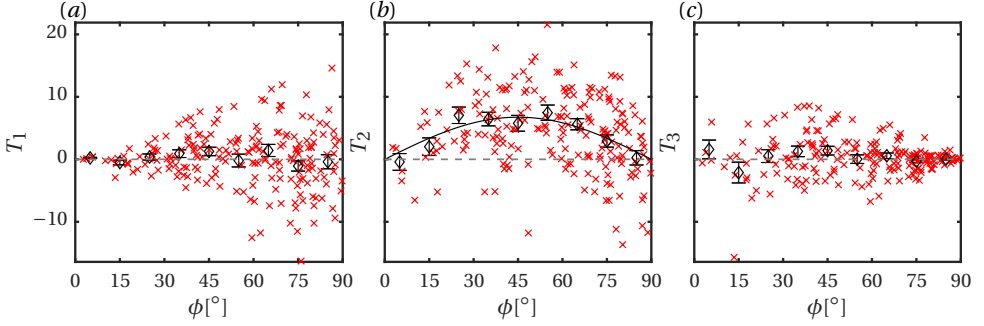Figure 5.6: Torques (*a*) T_1, (*b*) T_2, and (*c*) T_3 distribution for different particles (✗) with averages at regular ϕ intervals (◇) in a random configuration at $Re = 100$ and $\epsilon_s = 0.3$. Due to flow symmetry, the average T_1 and T_3 acting on particles are statistically zero. However, the pitching torque T_P (or T_2) scales proportional to $\sin\phi\cos\phi$ (solid black line).

Due to the finite number of measurements in these intervals, there is an error on the mean $\bar{x}$ of any property x. We use the standard error on the mean $\sigma_{\bar{x}}$ for the errorbars, computed as

$$\sigma_{\bar{x}} = \sigma/\sqrt{n}. \tag{5.14}$$

Here σ is the standard deviation of the corresponding variable x and n is the number of data points within the given ϕ interval. The normalized drag F_D and lift F_L can be computed from $\boldsymbol{F}_{norm}$ as

$$F_D = \quad F_1 \quad = \boldsymbol{F}_{norm} \cdot \hat{\boldsymbol{e}}_1, \tag{5.15}$$
$$F_2 \quad = \boldsymbol{F}_{norm} \cdot \hat{\boldsymbol{e}}_2, \text{ and} \tag{5.16}$$
$$F_L = \quad F_3 \quad = \boldsymbol{F}_{norm} \cdot \hat{\boldsymbol{e}}_3. \tag{5.17}$$

Since the reported forces are without buoyancy effects, the $(1 - \epsilon_s)$ term must be considered accordingly for both drag and lift while performing Euler-Lagrangian simulations. Due to the influence of neighbouring particles, the lateral force F_2 for each individual particle may not be equal zero, as shown in figure 5.5 ($Re = 100$ and $\epsilon_s = 0.3$). However, due to symmetry, the average F_2 does equal zero. Therefore, F_2 is not considered in our further discussion. The torques about the above defined axes are

$$T_1 \quad = \boldsymbol{T}_{norm} \cdot \hat{\boldsymbol{e}}_1, \tag{5.18}$$
$$T_P = \quad T_2 \quad = \boldsymbol{T}_{norm} \cdot \hat{\boldsymbol{e}}_2, \text{ and} \tag{5.19}$$
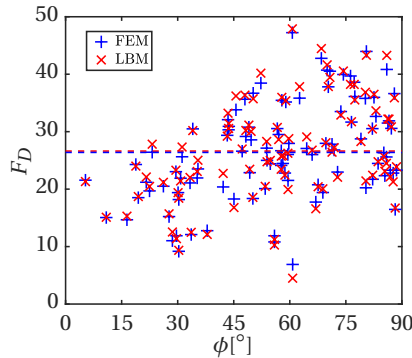$$T_3 \quad = \boldsymbol{T}_{norm} \cdot \hat{\boldsymbol{e}}_3. \tag{5.20}$$

Figure 5.7: F_D obtained for individual particles in a random configuration from the LBM solver against FEM solver for $Re = 100$ and $\epsilon_s = 0.3$. The dashed lines in respective colours indicate the domain averages from the respective solvers.

Here T_P is the pitching torque acting on a particle. We show the three different torques for a flow through a random particle configuration at $Re = 100$ and $\epsilon_s = 0.3$ in figure 5.6. It can be observed that T_1 and T_3, though having some non-zero values, are statistically zero on average due to symmetry. The non-zero values are primarily due to hydrodynamic interactions with other particles. Only the average pitching torque T_P (or T_2) remains non-zero for different ϕ and varies as $\sin\phi\cos\phi$. Though individual particles experience non-zero T_1 and T_3, they become zero at $\phi = 0°$ and $\phi = 90°$ respectively, where the axis of symmetry of the particle coincides with the measured axis for torque. This implies that the hydrodynamic interaction of particles does not induce a torque (or a spin) about the axis of symmetry of the particle.

5.2.5. VALIDATION

Sufficient validation has been done for our LBM code in the past for flow around isolated particles (Sanjeevi & Padding, 2017; Sanjeevi *et al.*, 2018*a*). For a multiparticle configuration, we have chosen flow around a random assembly of 100 particles at $Re = 100$ and $\epsilon_s = 0.3$ and measure the F_D experienced by the individual particles. The LBM results are compared with results from COMSOL Multiphysics, a body-fitted, unstructured mesh based FEM solver. The simulated LBM domain is of size 360^3. The volume equivalent sphere diameter is $d_{eq} = 64.4$ lattice cells. The superficial velocity u_s is 0.0414 and the kinematic viscosity ν is 0.08/3 in lattice units. The FEM solver domain is made of 2.1 million elements. The resulting drag forces are shown in figure 5.7. A good agreement between LBM and FEM results can be observed. The average F_D experienced by all parti-
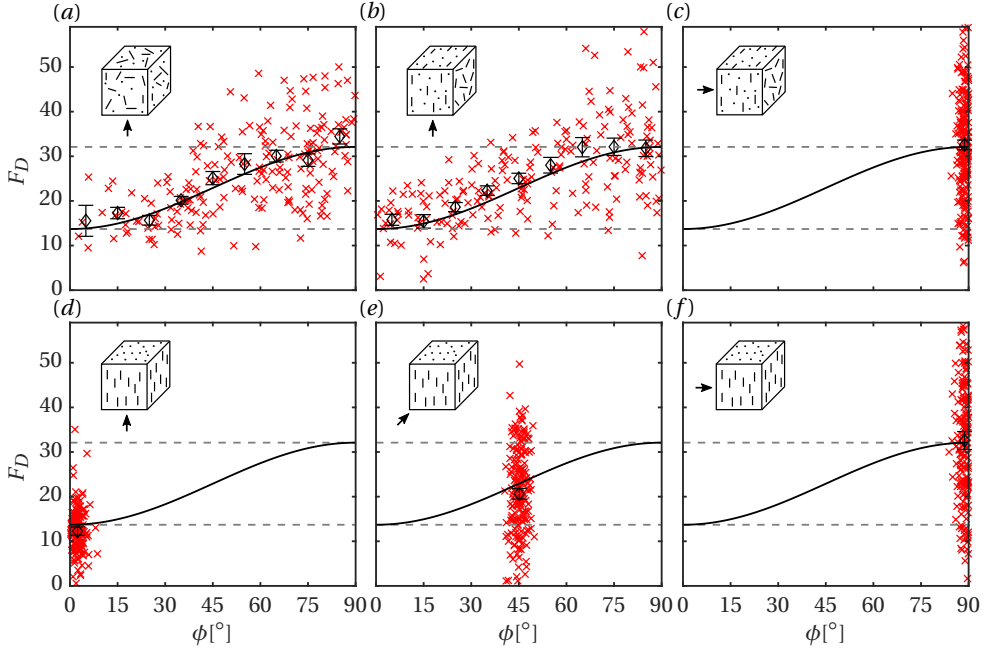
Figure 5.8: Configuration independence phenomenon at $Re = 100$ and $\epsilon_s = 0.3$ for different configurations with different flow directions (arrow indicated). F_D distribution for different particles (×) with averages at regular ϕ intervals (◇). (a) Random configuration, planar random configuration with flow (b) parallel and (c) perpendicular to the plane, unidirectional configuration with flow at (d) 0°, (e) 45°, and (f) 90° with respect to the principal configuration director. The solid black line indicates the *sine-squared* scaling.

cles in LBM and FEM solvers are 26.6 and 26.4 respectively. Also a good match in F_D values for individual particles at different ϕ can be observed.

5.3. TESTS OF CONFIGURATION INDEPENDENCE

Given a six-dimensional parameter space, exploring each dimension with approximately 5 simulations, results in a massive $5^6 = 15625$ simulations. Furthermore, closures must be created for drag, lift and torque as a function of this six-dimensional space. Before proceeding with these simulations, we tried to identify if there are any independent parameters specifically related to the mutual orientation of particles. In this section, we will show that the average hydrodynamic force on a non-spherical particle is independent of the mutual orienta-

tion of the particles themselves. This configuration independence removes the configuration parameters S_1, S_2 and flow angle parameters α and β from the parameter space to be explored. We find that, when averaged over a number of particles, the only dependence that the particles exhibit regarding orientation is the particle's incident angle ϕ as in flow around single particles. Effectively, we will show that the average force depends only on the Reynolds number Re, solids volume fraction ϵ_s and the incident angle ϕ of individual particles with respect to the flow direction.

In the extremely dilute regimes, i.e. $\epsilon_s \to 0$, it is already shown that there exists a sine-squared scaling of drag for elongated non-spherical particles (Sanjeevi & Padding, 2017; Sanjeevi *et al.*, 2018*a*). In this section, we discuss the results of flow around different configurations at an intermediate solids volume fraction of $\epsilon_s = 0.3$. Results of different configurations (in respective plot insets) at an intermediate $Re = 100$ are shown in figure 5.8 such as fully random, planar random with flows parallel and perpendicular to the planes and unidirectional configurations with principal directors at different angles. Though there exists scatter in the measured F_D on individual particles, it can be observed that the average F_D for different ϕ intervals scales similar to sine-squared scaling as in our earlier works of isolated particles. In other words, the average F_D at any ϕ can be computed as

$$F_{D,\phi} = F_{D,\phi=0°} + (F_{D,\phi=90°} - F_{D,\phi=0°})\sin^2\phi. \tag{5.21}$$

It is important to note that the *same* values for average $F_{D,\phi=0°}$ and $F_{D,\phi=90°}$ emerge for all configurations. Likewise, we also show that the scaling phenomenon extends to both Stokes and high Re regimes in figure 5.9. With the sine-squared scaling behaviour (or the configuration independence) identified at $\epsilon_s = 0$ and $\epsilon_s = 0.3$, it can be inferred that the scaling is safely applicable in the region $0 \leq \epsilon_s \leq 0.3$. We have verified the same at $\epsilon_s = 0.1$ and the results are not shown here for brevity. Though we observe the results are dependent on only 3 parameters, namely Re, ϵ_s and ϕ, the simulation needs to be set up for only two parameters, namely Re and ϵ_s. With a sufficiently random configuration, the system involves different particle orientations covering all ϕ. A caveat with a random configuration is that there are always very few particles near $\phi = 0°$, as shown in section 5.2.3. Therefore, biased random configurations with more particles at $\phi = 0°$ are created and at least two simulations are performed for better statistics.

We also observe the configuration independence phenomenon at $\epsilon_s = 0.4$. The criterion considered to declare configuration independence phenomena is that the average drag results in a given ϕ range of different configurations are within 10% deviation. In almost all cases, the deviations are within $\pm$ 5%. How-
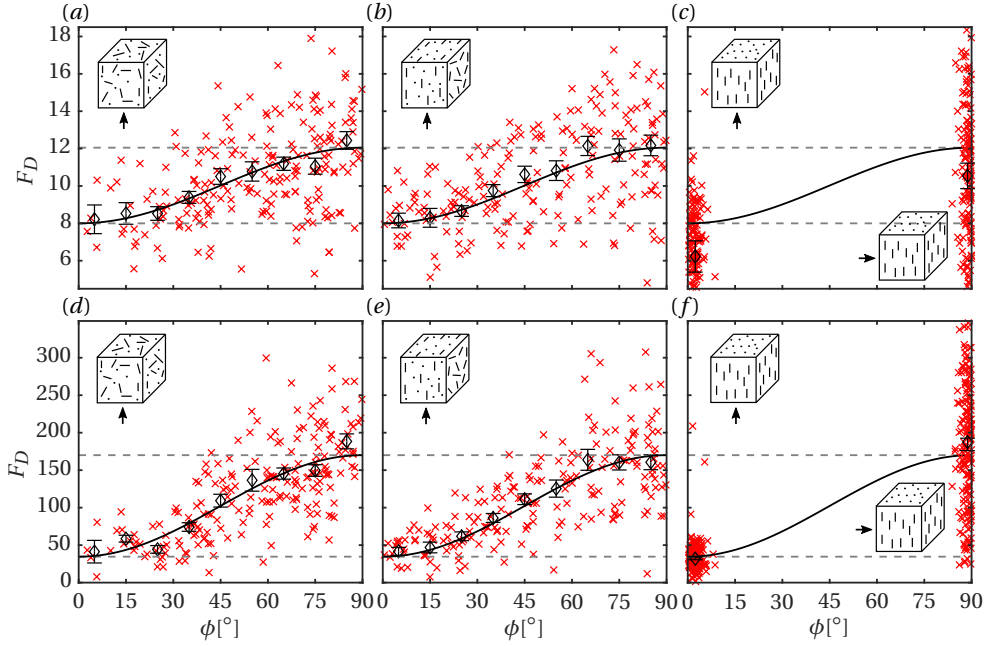
Figure 5.9: Configuration independence phenomenon at moderate solids fraction $\epsilon_s = 0.3$ for $(a - c)$ $Re = 0.1$ (low Re) and $(d - f)$ $Re = 1000$ (high Re) for different configurations and different flow directions (arrow indicated). F_D distribution for different particles ($\times$) with averages at regular ϕ intervals ($\diamond$). (a, d) Random configuration, (b, e) planar random configuration with flow parallel to the plane, (c, f) combined results of unidirectional configuration with flow 0° and 90° with respect to the principal configuration director. The solid black line indicates the respective *sine-squared* scaling.
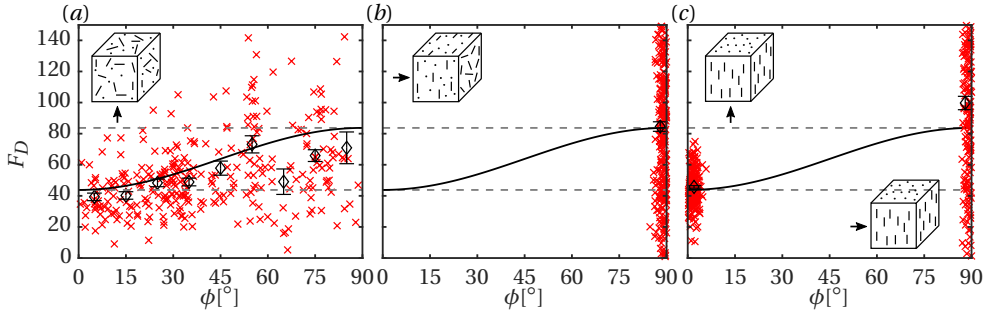
Figure 5.10: Configuration independence phenomenon at dense solids fraction $\epsilon_s = 0.5$ for $Re = 100$ for different configurations and different flow directions (arrow indicated). F_D distribution for different particles (×) with averages at regular ϕ intervals (◊).

ever in a dense case with $\epsilon_s = 0.5$, several more factors such as the mutual orientations, relative positions of particles, etc. influence the results. The F_D distribution for such dense configurations at $Re = 100$ and $\epsilon_s = 0.5$ are given in figure 5.10. Although these results can be predominantly parametrized by Re, ϵ_s, and ϕ, the influence of the additional parameters cannot be ignored. Therefore, specific cases of $\epsilon_s = 0.5$ are performed with more simulations for better statistics.

For a practical fluidization or other relevant gas-solid flow simulation, the densest configuration is most likely to occur when the particles are at bottom or at rest (e.g. before the start of fluidization). In such a dense condition, the particle configuration itself is dependent on the wall geometry. For a typical bed configuration with a flat wall at the bottom, the particles also roughly align in planes parallel to the bottom wall, i.e. a planar random configuration. Pournin *et al.* (2005) observed the same for particles poured freely from the top. Similarly, we also observe the same for a bed containing freely poured particles settled under gravity ($\epsilon_s = 0.54$), as shown in figure 5.11. The bed contains 30000 particles and it can be observed that roughly 2/3 of all particles are in the range $\phi = 70 - 90°$ confirming our hypothesis. Given such criteria, the most relevant regime would be to generate an accurate fit for average $F_{D,\phi=90°}$ at high ϵ_s.

It should also be noted that with increasing aspect ratio of elongated particles, the maximum ϵ_s decreases for a packed bed (Williams & Philipse, 2003). This is because the locking phenomenon is stronger with high aspect ratio particles. Unless the particles are packed with their orientations aligned, the decrease in peak ϵ_s for high aspect ratio elongated particles is unavoidable. Also, practical applications as shown in figure 5.11 do not allow such long range ordering. A decreasing peak ϵ_s implies that the configuration independence phenomenon
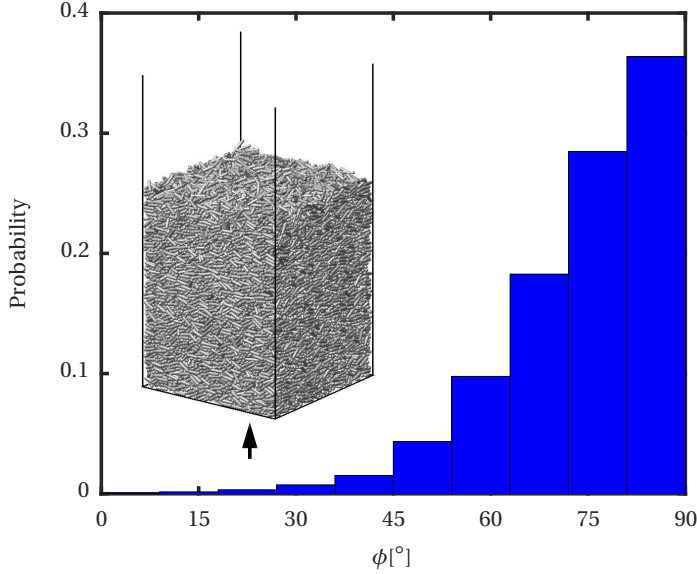
Figure 5.11: Histogram of incident angle ϕ for a packed bed with 30000 particles. The arrow indicates the flow direction.

will be very applicable. With the observed sine-squared drag scaling, the pressure drop across a packed bed can be determined with the knowledge of the ϕ distribution alone.

In the subsequent sections, we will show that in the dilute and intermediate ϵ_s regimes, the influence of ϵ_s is nearly shape independent. This implies that the drag on isolated non-spherical particles can be combined with sphere-based multiparticle correlations for the voidage effect to mimic flow around assemblies of non-spherical particles upto intermediate ϵ_s.

5.3.1. Explored regimes

In this section, we briefly explain the regimes explored in the current work and also explain the number of independent simulations performed per regime tested. An example of the flow stream lines for a random configuration at $Re = 100$ and $\epsilon_s = 0.3$ is shown in figure 5.12. Until solids volume fractions of $\epsilon_s = 0.35$, the generation of randomly orientation configurations is possible, as experienced by He & Tafti (2018) for prolate spheroids of aspect ratio 2.5. In our case, we are able to achieve random configurations upto $\epsilon_s = 0.4$. However for denser configurations, it is difficult to generate a truly random configuration. For

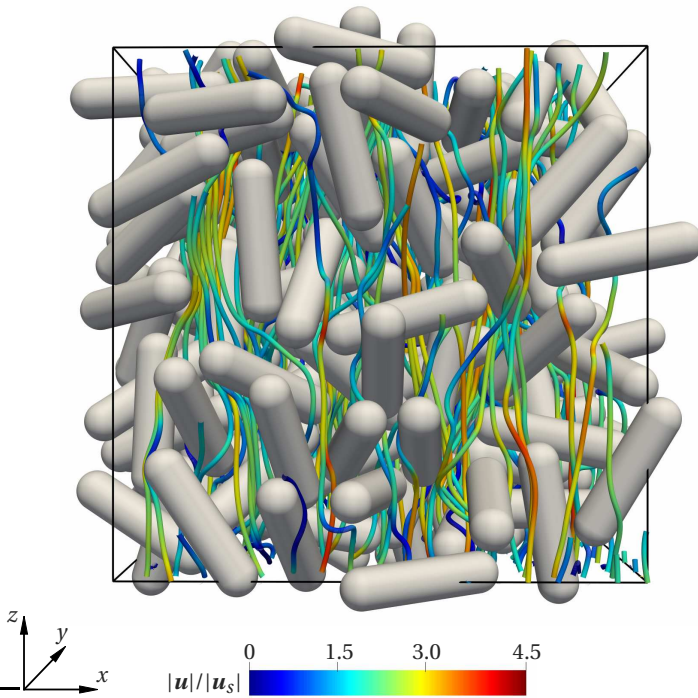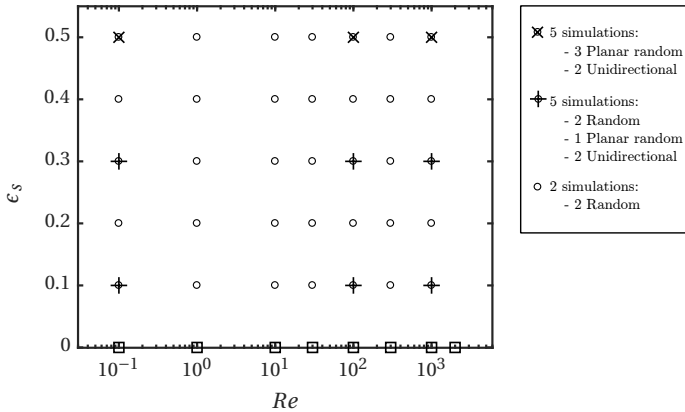Figure 5.12: Flow streamlines for a random configuration at $Re = 100$ and $\epsilon_s = 0.3$.

Figure 5.13: Regime map containing the explored parameter space in the current work (○) and our previous work Sanjeevi & Padding (2017) (□). +, × indicate the regimes with extra simulations and tested for configuration independence.

dense configurations of $\epsilon_s = 0.5$, the particles have a natural tendency to orient to planar random or unidirectional orientation configurations. A truly random configuration with a finite number of particles, at such solids volume fraction, is not possible. This is due to a strong orientation bias imposed by neighbouring particles due to lack of inter-particle space. The explored flow regimes are indicated in figure 5.13. Overall, at least two simulations are performed for the explored regimes. However for specific cases of dilute and intermediate ϵ_s, we performed 5 simulations with 2 random, 1 planar random with flow aligned to the plane and 2 unidirectional configurations with flow parallel and perpendicular to the principal director. For solids fraction $\epsilon_s = 0.5$, 3 planar random configurations with flows aligned to the plane and 2 unidirectional configurations with flows parallel and perpendicular to the principal director are performed. For cases with more simulations, the results are accordingly weighted while making the fits.

5.4. Results

5.4.1. Drag

With sine-squared scaling valid as shown in section 5.3, the average drag experienced by a particle in a multiparticle system can be explained by the equation 5.21 involving only the average drag experienced at $\phi = 0°$ and $\phi = 90°$. Therefore, we propose to generate fits for average $F_{D,\phi=0°}$ and $F_{D,\phi=90°}$ as a function of Re and ϵ_s as

$$F_D(Re, \epsilon_s) \quad = F_{d,isol} \cdot (1 - \epsilon_s)^2 + F_{\epsilon_s} + F_{Re,\epsilon_s}. \tag{5.22}$$

The corresponding terms are as follows:

$$F_{d,isol}(Re) \quad = C_{d,isol} \frac{Re}{24}, \tag{5.23}$$

$$F_{\epsilon_s}(\epsilon_s) \quad = a\sqrt{\epsilon_s}(1 - \epsilon_s)^2 + \frac{b\epsilon_s}{(1 - \epsilon_s)^2}, \text{ and} \tag{5.24}$$

$$F_{Re,\epsilon_s}(Re, \epsilon_s) \quad = Re^c \epsilon_s^d \left(e(1 - \epsilon_s) + \frac{f\epsilon_s^3}{(1 - \epsilon_s)} \right) + g\epsilon_s(1 - \epsilon_s)^2 Re. \tag{5.25}$$

Here, $C_{d,isol}$ is the isolated particle drag at given Re as detailed in Sanjeevi *et al.* (2018*a*) for the considered particle (fibre) for both $\phi = 0°$ and $\phi = 90°$. The coefficients in equations 5.24 and 5.25 for both average $F_{D,\phi=0°}$ and $F_{D,\phi=90°}$ are given in table 5.2. The average absolute deviation of the fits and simulation data are 3.5% and 2% for $F_{D,\phi=0°}$ and $F_{D,\phi=90°}$, respectively.

| Coefficients | F_D | | $F_{L,mag}$ |
	$\phi = 0°$	$\phi = 90°$	
a	2	3	0.85
b	11.3	17.2	5.4
c	0.69	0.79	0.97
d	0.77	3	0.75
e	0.42	11.12	-0.92
f	4.84	11.12	2.66
g	0	0.57	1.94

Table 5.2: Coefficients of the fits for average F_D and F_L
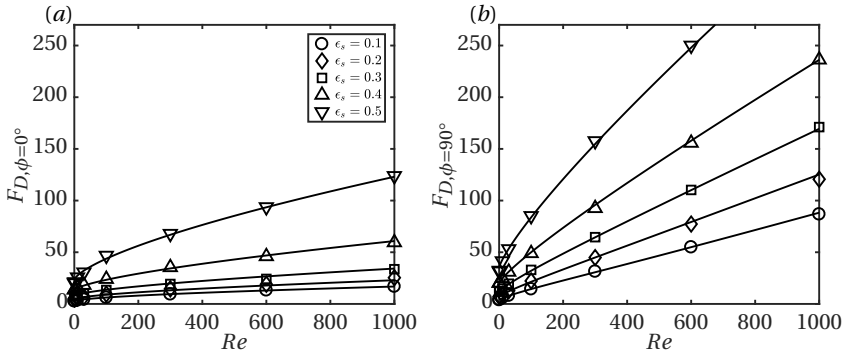
Figure 5.14: The averaged drag forces (*a*) $F_{D,\phi=0°}$ and (*b*) $F_{D,\phi=90°}$ at different Re and ϵ_s. The markers indicate simulation data and the solid lines are corresponding fits.
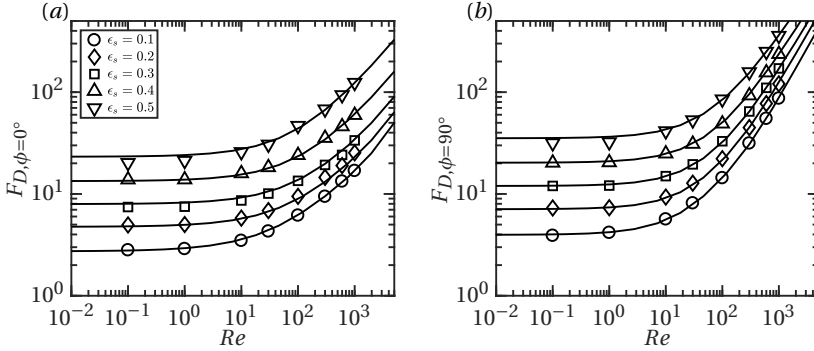
Figure 5.15: The fits for average (*a*) $F_{D,\phi=0°}$ and (*b*) $F_{D,\phi=90°}$ at different Re and ϵ_s beyond the simulated regimes of $0.1 \leq Re \leq 1000$. The markers indicate simulation data and the solid lines denote corresponding fits.
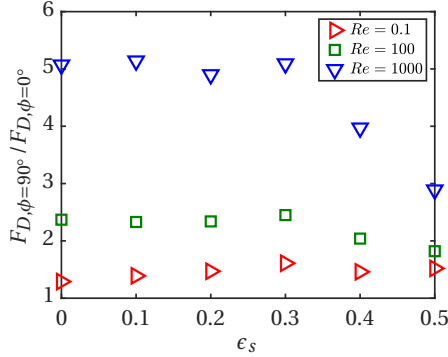

Figure 5.16: Ratio of average perpendicular to average parallel drag $F_{D,\phi=90°}/F_{D,\phi=0°}$ from simulations for different Re and ϵ_s.

The simulated data and corresponding fits are shown in figure 5.14. The fits follow the physical limits beyond the Re range simulated as shown in figure 5.15. In the Stokes flow limit, it can be observed that both $\phi = 0°$ and $\phi = 90°$ normalized drag becomes independent of Re. In the high Re limit, the normalized drag approaches a linear dependency on Re.

The ratio of average perpendicular to average parallel drag $F_{D,\phi=90°}/F_{D,\phi=0°}$ at different Re and ϵ_s is shown in figure 5.16. For low Re ($Re = 0.1$), the ratio remains constant at a value a little larger than 1 for all ϵ_s. The reason for this is that at low Re, the particles experience stronger viscous effects. The viscous drag reduces and pressure drag increases with increasing ϕ at low Re. The same has been confirmed for isolated particles (Sanjeevi & Padding, 2017) and for a
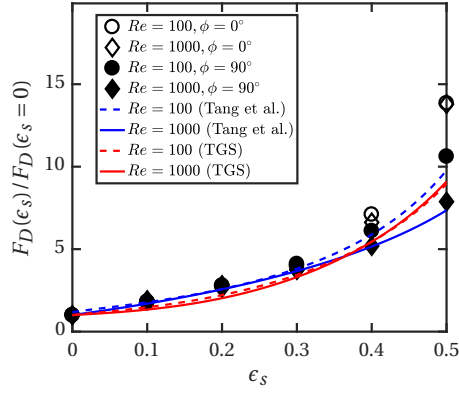
Figure 5.17: Voidage effect on average drag: $F_D(\epsilon_s)/F_D(\epsilon_s = 0)$ for $\phi = 0°$ and $\phi = 90°$ in the inertial regimes as a function of ϵ_s for spherocylinders (this work, symbols), compared with voidage effect for spheres from literature. TGS denotes Tenneti *et al.* (2011).
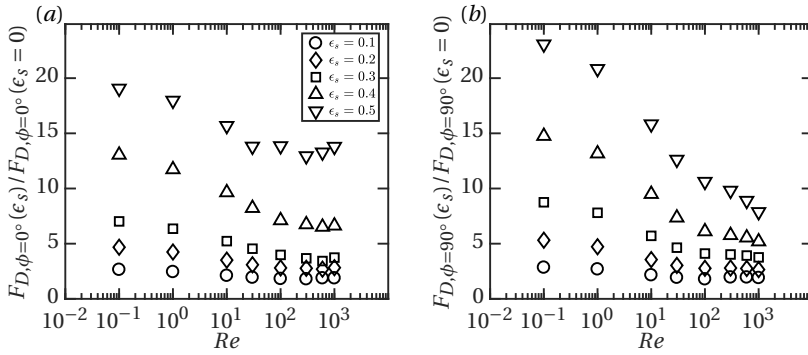

Figure 5.18: Voidage effect on average drag: $F_{D,\phi=0°}(\epsilon_s)/F_{D,\phi=0°}(\epsilon_s = 0)$ and $F_{D,\phi=90°}(\epsilon_s)/F_{D,\phi=90°}(\epsilon_s = 0)$ as a function of Re.

multiparticle system (He & Tafti, 2018). The combined viscous and pressure drag components result in a drag ratio close to 1 for the considered spherocylinders at low Re. Due to inertial dominance at moderate and large Re ($Re \geq 100$) we can observe a near constant drag ratio for solids volume fractions upto $\epsilon_s = 0.3$ and a decrease in the ratio for $\epsilon_s > 0.3$. Further, figure 5.16 gives an indication that for very dense crowding, i.e. at $\epsilon_s > 0.5$, there is a possibility that $F_{D,\phi=90°}/F_{D,\phi=0°}$ tends back to approximately 1. Up to moderate crowding, although the flow is disturbed due to the presence of neighbouring particles, there is sufficient inter-particle space for flow to achieve uniformity. However with increased particle crowding, there appear pronounced fluctuations in flow velocities (see also section 5.4.4), resulting in a reduced drag ratio at high ϵ_s. This is an important finding because the traditional approach of Euler-Lagrangian simulations involve combining isolated non-spherical particle drag with the voidage effects based on sphere assemblies. This would result in a constant drag ratio for all ϵ_s. This in turn could affect Euler-Lagrangian simulation results, especially in predicting the minimum fluidization velocity as there exists a dense packing of particles. This mandates the need for the current work.

Figure 5.17 shows a similar interesting observation: The scaling of the voidage effect $F_D(\epsilon_s)/F_D(\epsilon_s = 0)$ in the inertial regime (high Re limit) is shape and orientation independent for $\epsilon_s \leq 0.3$. Here, we have normalized the average drag with respective isolated particle drag for different Re and ϕ. It can be observed that all the normalized points fall on a same trend until $\epsilon_s = 0.3$. Similar normalized F_D for spheres from Tang *et al.* (2015) at $Re = 100$ and $Re = 1000$ also show the same trend until $\epsilon_s = 0.3$. Here, we use the isolated sphere drag correlation of Schiller & Naumann (1935) for the normalization. The predictions of Tenneti *et al.* (2011) for spheres do not follow the exact trend for the voidage effects as observed from figure 5.17. It should be noted that Tenneti *et al.* (2011) explored only until $Re = 300$ in their work and extrapolation to high Re may not apply. Therefore, the above discussion indicates that spherical drag correlations for the voidage effect, combined with isolated non-spherical particle drag correlations can be applied to dilute suspension simulations of non-spherical particles in the inertial regimes. For a given non-spherical particle, the effect of crowding (ϵ_s) on F_D is different for different Re and ϕ. Figure 5.18 shows the voidage effect (average F_D normalized by the corresponding isolated particle drag) as a function of Re. It can be seen at low Re, the increase in drag due to crowding is comparable for both $\phi = 0°$ and $\phi = 90°$ at different ϵ_s. At high Re, the increase in drag due to crowding with increasing ϵ_s is much stronger for $\phi = 0°$ compared to $\phi = 90°$. This also explains further the reason for the observed reduction in average perpendicular to average parallel drag ratios with increasing ϵ_s in figure 5.16.
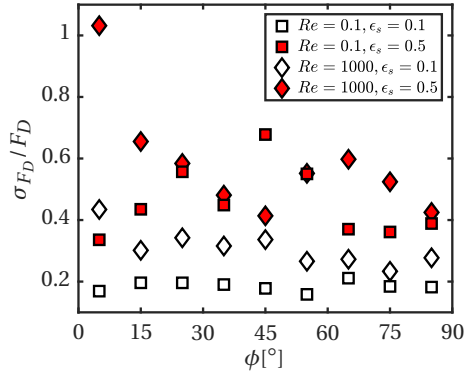
Figure 5.19: The standard deviations σ_{F_D} of the distribution of individual drag values, normalized by the corresponding average F_D in different intervals of incident angle ϕ. Open symbols correspond to dilute configurations and filled symbols correspond to dense configurations.

In the previous sections, we discussed the F_D averaged over all particles with similar ϕ. However, the distribution of F_D within a ϕ interval is itself also a function of both Re and ϵ_s. The standard deviations of the distribution of drag measurements, normalized by the average F_D in the corresponding ϕ interval, are plotted in figure 5.19. It is important that the standard deviations are normalized by the respective average F_D, rather than against a single value, say $F_{D,\phi=90°}$, for a given Re and ϵ_s. This is because with increasing Re, the ratio $F_{D,\phi=90°}/F_{D,\phi=0°}$ increases, as shown in figure 5.16 earlier. Therefore, using average $F_{D,\phi=90°}$ for normalization will make the standard deviations at $\phi = 0°$ appear insignificant at large Re.

For dilute configurations ($\epsilon_s = 0.1$), we clearly observe that increasing Re results in an increased σ_{F_D}/F_D at all ϕ. It should be noted that the absolute magnitudes of average F_D at $Re = 1000$ are much larger than at $Re = 0.1$. Despite the normalization by these larger values, we observe increased standard deviations for higher Re. This is because at low Re, the viscous effects dominate, resulting in long-range flow uniformity. Conversely, at high Re, the boundary layers are thinner and flow wakes are stronger. This results in high non-uniformity in the incoming flow on each particle, and thereby large fluctuations in the hydrodynamic forces. For dense particle configurations ($\epsilon_s = 0.5$), it can be observed that σ_{F_D}/F_D increases relative to dilute conditions, with a higher standard deviation for higher Re. The reason for higher spread in F_D is due to the fact the particles locally encounter highly non-uniform incoming flows when there is more crowding.
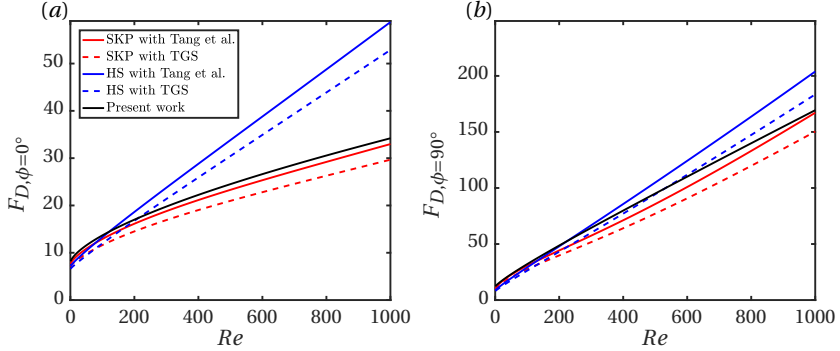
Figure 5.20: Comparison of average F_D for (*a*) $\phi = 0°$ and (*b*) $\phi = 90°$ for $\epsilon_s = 0.3$. SKP denotes Sanjeevi *et al.* (2018*a*), HS denotes Hölzer & Sommerfeld (2008), and TGS denotes Tenneti *et al.* (2011). The solid black line is equation 5.22.

COMPARISON WITH OTHER LITERATURE

Given the unavailability of multiparticle correlations for non-spherical particles, we combine the available literature results on isolated non-spherical particles with voidage effects based on spheres. For this, we normalize the multiparticle drag of spheres with the isolated sphere Schiller & Naumann (1935) correlation and multiply with the isolated non-spherical particle drag. The results are shown in figures 5.20 and 5.21 for $\epsilon_s = 0.3$ and $\epsilon_s = 0.5$, respectively. The isolated particles drag law used are SKP (Sanjeevi *et al.*, 2018*a*) and HS (Hölzer & Sommerfeld, 2008). They are accordingly combined with the multiparticle effects of TGS (Tenneti *et al.*, 2011) and Tang *et al.* (2015) for spheres. In the moderately crowded regime ($\epsilon_s = 0.3$), our earlier suggestion of combining isolated non-spherical particle drag with multiparticle effects from spheres works well. For example, the combination of SKP with Tang *et al.* (2015) follows nearly the same trend as that of the current work (equation 5.22). This can be observed for both $\phi = 0°$ and $\phi = 90°$. However for dense regimes ($\epsilon_s = 0.5$), it can be observed that the combination of SKP with Tang *et al.* (2015) does not agree well with the present work for $\phi = 0°$. At the same time, the combination with the HS (Hölzer & Sommerfeld, 2008) isolated drag law seem to be closer to the current work for $\epsilon_s = 0.5$. Such an agreement must be considered with care. The decent agreement occurs because HS possesses high drag values for $\phi = 0°$ (for $\epsilon_s = 0$), in combination with a weak voidage effect for spheres. On the other hand, SKP with TGS or Tang *et al.* (2015) show decent agreement with the present work for $\phi = 90°$.
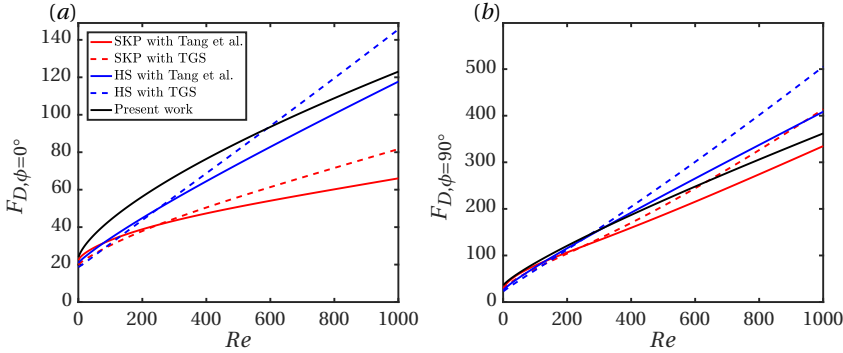
Figure 5.21: Comparison of average F_D for (a) $\phi = 0°$ and (b) $\phi = 90°$ for $\epsilon_s = 0.5$. SKP denotes Sanjeevi *et al.* (2018*a*), HS denotes Hölzer & Sommerfeld (2008), and TGS denotes Tenneti *et al.* (2011). The solid black line is equation 5.22.

5.4.2. LIFT

The normalized lift $F_{l,\phi}$ on a single elongated particle from Sanjeevi *et al.* (2018*a*) is given by

$$F_{l,\phi}(Re,\phi) \quad = F_{l,isol} \cdot S_{f,\phi}, \text{ with} \tag{5.26}$$

$$F_{l,isol}(Re) \quad = \left(\frac{b_1}{Re} + \frac{b_2}{Re^{b_3}} + \frac{b_4}{Re^{b_5}}\right)\frac{Re}{24}, \text{ and} \tag{5.27}$$

$$S_{f,\phi}(Re,\phi) \quad = \sin\phi^{(1+b_6 Re^{b_7})}\cos\phi^{(1+b_8 Re^{b_9})}. \tag{5.28}$$

Here, $S_{f,\phi}$ is the scaling function dependent on Re and ϕ. The coefficients b_i are accordingly listed in the mentioned literature. In particular, the coefficients b_6 to b_9 describe the amount of skewness of the lift coefficient on a single elongated particle around $\phi = 45°$. In the current work, we observe the same skewness for the multiparticle system at different Re. Therefore, we assume the term $S_{f,\phi}$ remains the same for the multiparticle system. The average lift F_L for a multiparticle system takes the following form:

$$F_{L,\phi}(Re,\epsilon_s,\phi) \quad = F_{L,mag}(Re,\epsilon_s) \cdot S_{f,\phi}(Re,\phi). \tag{5.29}$$

The functional form of $F_{L,mag}(Re,\epsilon_s)$ remains similar to that of the drag and is given by

$$F_{L,mag}(Re,\epsilon_s) \quad = F_{l,isol}(Re) \cdot (1-\epsilon_s)^2 + F_{\epsilon_s}(\epsilon_s) + F_{Re,\epsilon_s}(Re,\epsilon_s) \tag{5.30}$$
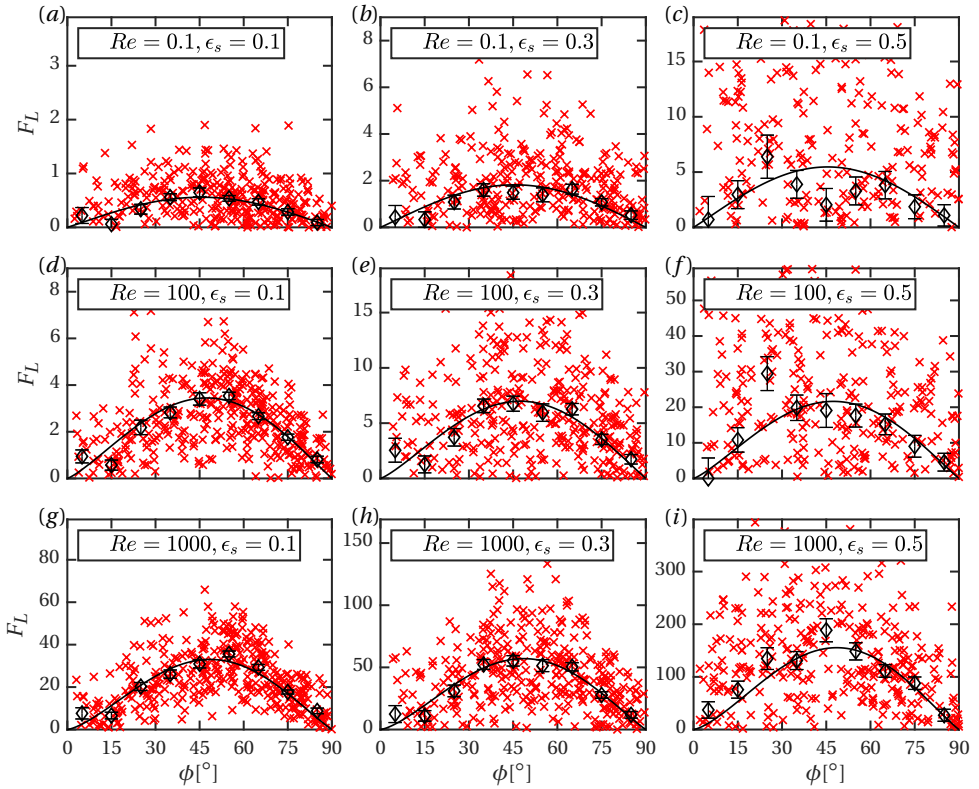
Figure 5.22: Distributions of lift forces F_L (×) with averages at regular ϕ intervals ($\Diamond$) for different Re and ϵ_s. The solid line denotes the $F_{L,\phi}$ fit (equation 5.29). Each plot includes data from two independent simulations with a total 400 data points. It should be noted that the scales are different for each plot.
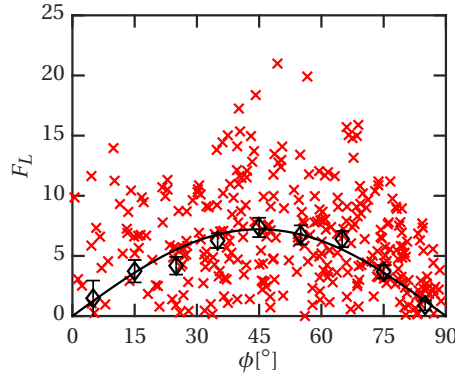
Figure 5.23: Distribution of F_L (×) for $Re = 100$ and $\epsilon_s = 0.3$ with averages ($\Diamond$) in regular ϕ intervals. The solid black line indicates the corresponding simple fit based on equation 5.34. The fit includes data from two different simulations totalling 400 data points.

with

$$F_{\epsilon_s}(\epsilon_s) \quad = a\sqrt{\epsilon_s}(1-\epsilon_s)^2 + \frac{b\epsilon_s}{(1-\epsilon_s)^2}, \text{ and} \tag{5.31}$$

$$F_{Re,\epsilon_s}(Re,\epsilon_s) \quad = Re^c \epsilon_s^d \left(e(1-\epsilon_s) + \frac{f\epsilon_s^3}{(1-\epsilon_s)} \right) + g\epsilon_s(1-\epsilon_s)^2 Re. \tag{5.32}$$

The corresponding coefficients are given in table 5.2. The proposed average lift correlation has around 5% average absolute deviation with respect to the averaged lift from simulations. The comparison of the average F_L from simulations and the proposed correlation is shown in figure 5.22.

A SIMPLIFIED LIFT FUNCTION

In our earlier works (Sanjeevi & Padding, 2017; Sanjeevi *et al.*, 2018*a*), we have shown successfully that for elongated particles, the relation between lift and drag in the Stokes flow regime can be successfully used for higher Re flows too. In other words, F_L at different ϕ can be computed as

$$F_{L,\phi} = (F_{D,\phi=90°} - F_{D,\phi=0°})\sin\phi\cos\phi. \tag{5.33}$$

In this section, we show that equation 5.33 is a reasonable approximation even for a multiparticle system. This implies that the scaling law is valid not only just for different Re but even for different ϵ_s. Given a measured average F_L distribution from simulations at a given Re and ϵ_s, the data can be fitted in a simple form
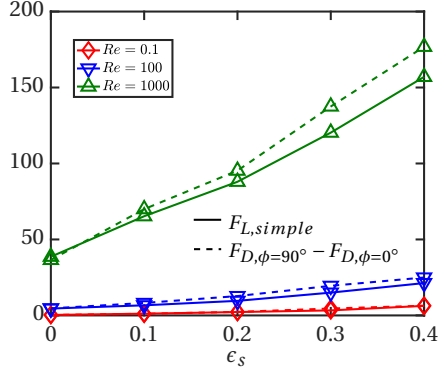
Figure 5.24: Comparison of $F_{D,\phi=90°} - F_{D,\phi=0°}$ with $F_{L,simple}$ at different Re and ϵ_s. The difference $F_{D,\phi=90°} - F_{D,\phi=0°}$ is based on averaged simulation data itself and not on the corresponding averaged F_D fits.

as

$$F_{L,\phi} = F_{L,simple} \sin\phi \cos\phi. \tag{5.34}$$

Here, $F_{L,simple}$ is a fit parameter that best describes the simulation data. An example for such a fit for $Re = 100$ and $\epsilon_s = 0.3$ is given in figure 5.23. The comparison of the Stokes regime lift law (equation 5.33) and our hypothesis (equation 5.34) is shown in figure 5.24 and it can be observed that there is a good agreement. The highest absolute deviation observed between the equations is still less than 20% and average absolute deviation is around 12%. Therefore in Euler-Lagrangian simulations, in the absence of explicit lift data, equation 5.33 can be applied to include the effects of lift with acceptable accuracy. This implies that in the often-used approach of using Hölzer & Sommerfeld (2008) type drag correlations, combined with sphere-based voidage effect correlations in Euler-Lagrangian simulations, one can also include lift effects based on equation 5.33. In the following section, we will show the importance of including lift, as it is often of comparable magnitude to drag at high Re.

IMPORTANCE OF LIFT COMPARED TO DRAG

In Euler-Lagrangian simulations, the effect of lift forces is often neglected. This is because there is not much literature on non-spherical particle lift correlations. In this section, we analyse the magnitudes of lift compared to the drag on individual non-spherical particles at different Re and ϵ_s. Figure 5.25 shows the distributions of the magnitude of the lift force relative to the drag force on each particle
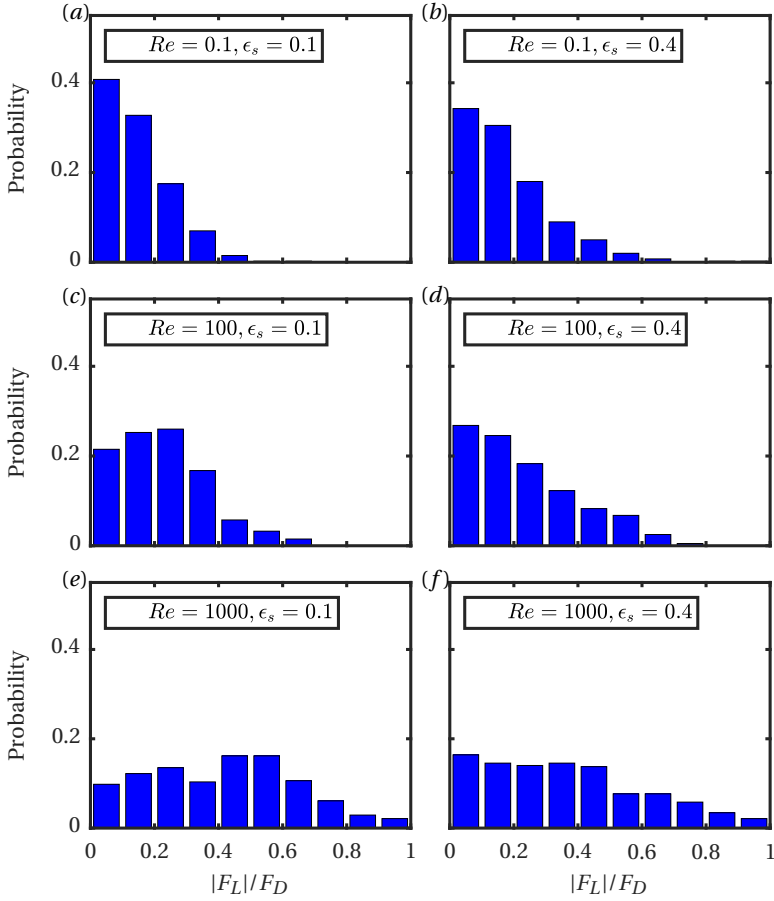
Figure 5.25: Distribution of lift force on individual particles normalized by corresponding drag force on each particle at different Re and ϵ_s.

Coefficients	$T_{P,mag}$
a	0.82
b	1.44
c	1.07
d	5.48
e	0.223

Table 5.3: Coefficients of the fits for $T_{P,mag}$

$|F_L|/F_D$. It can be observed that for Stokes flow ($Re = 0.1$), most particles experience lift which is about one order of magnitude smaller than the drag. However for high Re ($Re = 1000$), the distribution is much more wider spread and there are even some particles for which $|F_L|/F_D = 1$. This emphasizes the need for including lift in Euler-Lagrangian simulations, especially while handling Geldart D particles, where the encountered particle Re is high. With increasing ϵ_s, a different interesting observation can be made. In the low Re regime, increasing ϵ_s results in an increased probability of particles experiencing high lift magnitudes compared to the drag. On the contrary, at high Re ($Re = 1000$), increasing ϵ_s results in the $|F_L|/F_D$ distribution skewing to the left. It should be noted that the highest ϵ_s shown in figure 5.25 is $\epsilon_s = 0.4$ as opposed to $\epsilon_s = 0.5$, the highest ϵ_s explored. This is because random configurations are not possible for $\epsilon_s = 0.5$. To ensure consistency, all results shown in figure 5.25 are based on random configurations.

5.4.3. Torque

For an isolated non-spherical particle, the torque correlation (Sanjeevi *et al.*, 2018*a*) is given by:

$$T_{p,\phi}(Re,\phi) \quad = T_{p,isol}(Re) \cdot S_\phi(Re,\phi), \text{ with} \tag{5.35}$$

$$T_{p,isol}(Re) \quad = \left(\frac{c_1}{Re^{c_2}} + \frac{c_3}{Re^{c_4}} \right) \frac{Re}{32}, \text{ and} \tag{5.36}$$

$$S_\phi(Re,\phi) \quad = \sin\phi^{(1+c_5 Re^{c_6})} \cos\phi^{(1+c_7 Re^{c_8})}. \tag{5.37}$$

The Re dependent skewness terms c_5, c_6, c_7, c_8 equal zero for an isolated spherocylinder resulting in a symmetric distribution for ϕ around 45°. Likewise, we also observe a near symmetric distribution of average torque at different Re and ϵ_s for the multiparticle configuration (see figure 5.26). Unlike drag and lift,
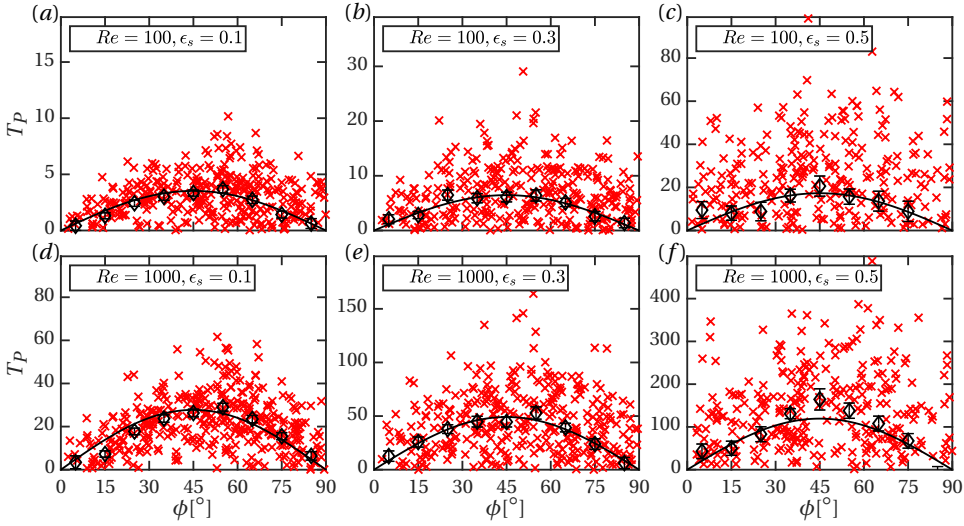
Figure 5.26: Distributions of T_P (×) with averages at regular ϕ intervals (◇) for different Re and ϵ_s. The solid black line denotes $T_{P,\phi}$ fit (equation 5.38). Each plot includes data from two independent simulations with each containing 400 data points. It should be noted that the scales are different for each plot.

for an isolated non-spherical particle, the pitching torque vanishes for all ϕ in the Stokes flow regime. We observe the same for the multiparticle configuration. Therefore, the proposed correlation for the average torque T_P is applicable only in the inertial regime ($10 < Re \leq 1000$) and is given by

$$T_{P,\phi}(Re,\epsilon_s,\phi) = T_{P,mag}(Re,\epsilon_s) \cdot \sin\phi \cos\phi, \text{ with} \tag{5.38}$$

$$T_{P,mag}(Re,\epsilon_s) = T_{p,isol}(Re) \cdot (1-\epsilon_s)^2 + T_{Re,\epsilon_s}(Re,\epsilon_s). \tag{5.39}$$

The corresponding terms in the scaling are as follows:

$$T_{Re,\epsilon_s}(Re,\epsilon_s) = Re^a \epsilon_s^b \left(c(1-\epsilon_s) + \frac{d\epsilon_s^3}{(1-\epsilon_s)} \right) + e\epsilon_s(1-\epsilon_s)^2 Re. \tag{5.40}$$

The average absolute deviation between equation 5.38 and corresponding simulation data is 3%. It should be noted that $T_{P,mag}$ in equation 5.39 maps only the magnitude of the torque for different Re and ϵ_s. The ϕ dependence is included separately with the *sine* and *cosine* terms. The comparison of $T_{P,mag}$ and the corresponding simulation data are given in figure 5.27. Given a symmetric form for $T_{P,\phi}$, the $T_{P,mag}$ is equal to twice the magnitude of $T_{P,\phi=45°}$ since $\sin\phi\cos\phi = 1/2$ at $\phi = 45°$. From figure 5.27, it can be observed that $T_{P,mag}$ roughly follows the same power law dependence on Re for different ϵ_s because
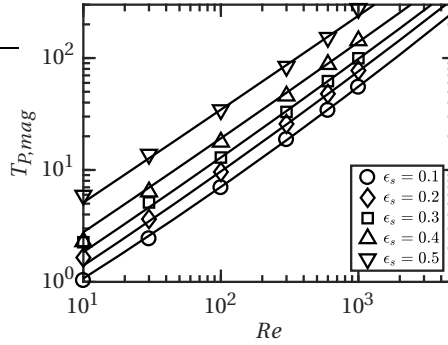
Figure 5.27: $T_{P,mag}$ at different Re and ϵ_s. The markers indicate simulation data and the solid line denotes fit at corresponding ϵ_s.

the slopes are similar. This is in contrast to the drag trends in figure 5.15, where the trend starts from zero slope at low Re to a constant slope at high Re. The reason is that the torque vanishes at low Re for all ϵ_s. The distributions of torque T_P for different Re, ϵ_s and ϕ are given in figure 5.26.

5.4.4. Flow histograms

In the previous sections, we discussed the influence of the flow on the hydrodynamic forces and torques on the particles. The flow around particulate assemblies can also be viewed as flow through a porous medium. In this section, we discuss the results of the influence of the particles on the flow distribution.

The probability distributions of the normalized axial flow velocities (u_{ax}/u_{avg}) at different Re and ϵ_s for random configurations are given in figure 5.28. Here, the normalization is done against the average axial velocity $u_{avg} = u_s/(1 - \epsilon_s)$ rather than the superficial velocity u_s to ensure a fair comparison for different ϵ_s. Only the velocities of fluid cells are shown here and the zero velocities in the solid cells are ignored. It can be observed that with increasing Re, the spread of the velocity distribution becomes narrower. This can be simply attributed to the increased inertial effects and thinner boundary layers for increasing Re. Interestingly, the high Re flows also demonstrate some negative velocities corresponding to wake effects. With increasing ϵ_s, the peaks of the distribution shift towards the left and the distribution itself spreads wider. This implies that the increased presence of particle surfaces at higher ϵ_s pulls the velocities of fluid cells towards zero (hence the left skewness). At the same time, the fluid accelerates in the bulk regions further removed from the particle surfaces resulting in increased velocities (and hence a wider distribution) to maintain the desired u_s.

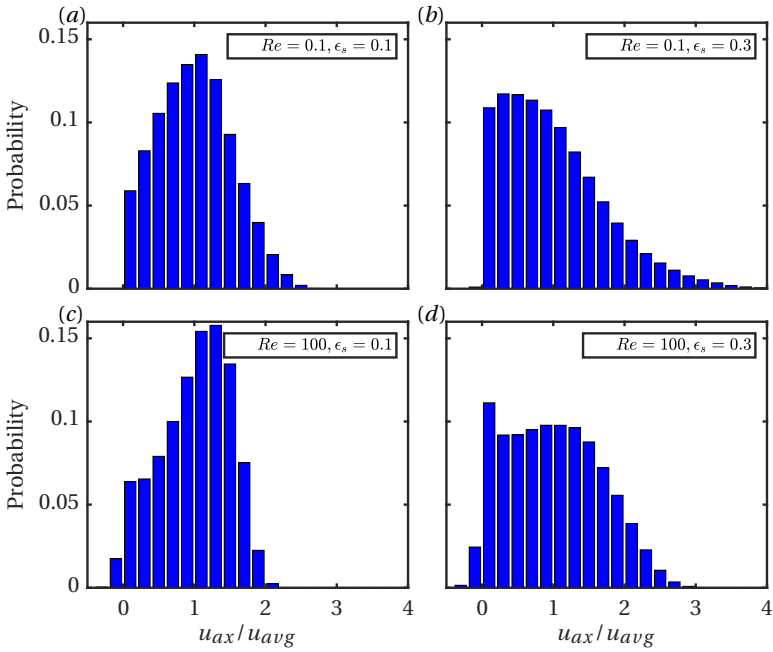eplacements

Figure 5.28: Axial velocity distributions at different Re and ϵ_s for a random configuration.
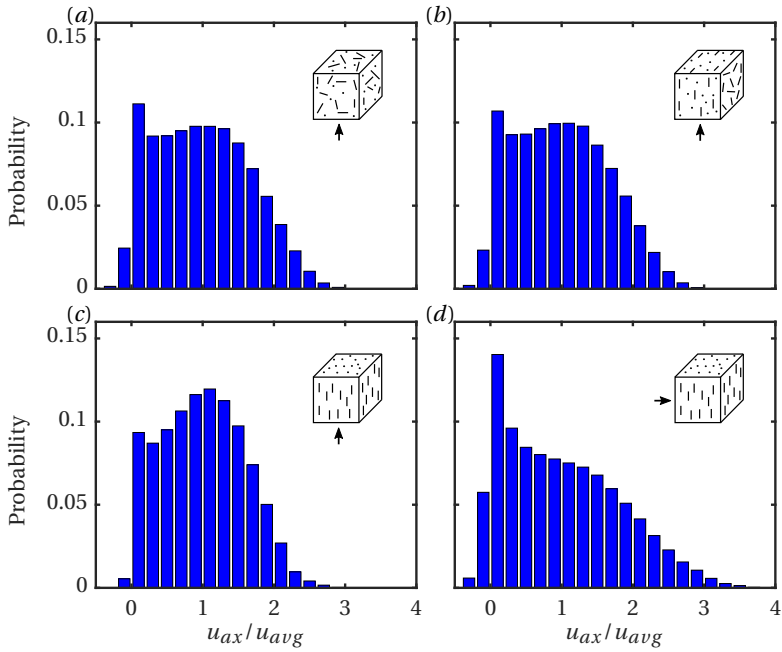
eplacements

Figure 5.29: Axial velocity distributions for different configurations at $Re = 100$ and $\epsilon_s = 0.3$.

It is also interesting to investigate the velocity distributions for different configurations for a given Re and ϵ_s. The distributions of u_{ax}/u_{avg} at $Re = 100$ and $\epsilon_s = 0.3$ for different configurations are plotted in figure 5.29. Given sufficient randomness of particles, as in random and planar random configurations (see figure 5.29 (a) and (b)), the velocity distributions are nearly identical. However, velocity distributions can be different for different configurations, as can be observed for the unidirectional configurations with flow parallel and perpendicular to the principal director (see figure 5.29 (c) and (d)). Among the different configurations shown, the unidirectional configuration with flow parallel to principal director has the least recirculation, as is evident from the least number of fluid cells with negative velocities ($u_{ax}/u_{avg} < 0$). At the same time, as expected, the unidirectional configuration with flow perpendicular to principal director has the highest amount of recirculation. Overall, we can infer that there is no dependency between the configuration independence phenomenon, explained in section 5.3, and the flow velocity distribution of different configurations. The variation in forces at different incident angles ϕ is mainly arising from the pressure forces. The same can also be confirmed from the multiparticle work of He & Tafti (2018), which is also in line with our finding for isolated non-spherical particles (Sanjeevi & Padding, 2017).

5.5. CONCLUSION

The flow around assemblies of axisymmetric, non-spherical particles has been studied extensively using the multi-relaxation-time lattice Boltzmann method. The performed simulations are from the Stokes flow regime to high Re ($0.1 \leq Re \leq 1000$) at different solids volume fraction ϵ_s ($\epsilon_s \leq 0.5$) and different mutual orientations of particles.

In general, forces on random assemblies of spheres are only dependent on Re and ϵ_s. Considering the non-spherical nature of the particles, we proposed four additional parameters to describe the flow problem: two to parametrize the mutual orientation of the non-spherical particles (S_1 and S_2) and two to represent the polar and azimuthal angles (α and β) of the averaged flow velocity with respect to the configuration. For this, we have developed different static particle configurations using Monte-Carlo simulations. In the process, the configurations are biased to the desired amount of nematic or bi-axial orientational order with the use of a Maier-Saupe potential. The flow simulations indicate that the average particle forces are configuration independent, at least for $\epsilon_s \leq 0.4$, implying that the four additional parameters do not influence the results. The only important parameter representing orientation dependence is the incident angle ϕ of individual particles with respect to the average flow direction.

The configuration independence greatly simplifies the parameter space to be explored from 6 to 3 dimensions, namely Re, ϵ_s, and ϕ. Of the three, the simulations are set up for only two parameters: Re and ϵ_s. Given a sufficiently random particle configuration, different incident angles ϕ are covered automatically. Another interesting result from the current work is that our previous finding of sine-squared scaling of drag for isolated non-spherical particles (Sanjeevi & Padding, 2017) applies also to multiparticle systems. In other words, given a Re and ϵ_s, the average drag on the subset of particles oriented at an incident angle ϕ with respect to the superficial flow velocity can be described with the knowledge of average drag at $\phi = 0°$ and $\phi = 90°$ alone. This information can be used in a packed bed to determine the pressure drop across the bed with the knowledge of ϕ distribution alone. In a multiparticle configuration, also the average lift on a particle at an incident angle ϕ can be computed with good accuracy using the average drag at $\phi = 0°$ and $\phi = 90°$, as in our previous work on isolated non-spherical particles. Having identified the dependent parameters, we proposed correlations for average drag, lift and torque for a multiparticle configuration. During the process, we used correlations for isolated non-spherical particles and extended them to the multiparticle systems.

We have also explored the validity of the conventional approach of combining known correlations for isolated non-spherical particle drag with correlations for voidage effects based on sphere packings. We observe that in the dilute and intermediate ϵ_s regimes ($\epsilon_s \leq 0.3$), the influence of ϵ_s is nearly shape independent. This implies that the above conventional approach can safely be used to mimic flow around assemblies of non-spherical particles upto intermediate ϵ_s. However for denser regimes, there is a need for multiparticle simulations and hence the need for this work. In the inertial regimes, the ratios of average drag at $\phi = 90°$ and $\phi = 0°$ ($F_{D,\phi=90°}/F_{D,\phi=0°}$) are nearly constant until $\epsilon \leq 0.3$ and then decrease with increasing ϵ_s. This further proves that the conventional approach is not valid for dense regimes. In the process, we have analysed the flow velocity distribution as function of Re and ϵ_s. Likewise, the influence of different particle configurations on the flow velocities have also been analysed.

Overall, this work provides a recipe to parametrize the drag, lift and torque experienced by non-spherical particles in multiparticle environment. To the best of the authors' knowledge, there exists no work which parametrizes the drag, lift and torque for non-spherical particles in a multiparticle environment. Generally, lift and torque are ignored in large scale Euler-Lagrangian simulations. The proposed accurate drag, lift and torque correlations enable future Euler-Lagrangian simulations to be performed with more realistic physics.

6

CONCLUSION & OUTLOOK

6.1. CONCLUSION

In the current work, fully resolved flows around different non-spherical particles, both isolated and assemblies, were performed using the multi-relaxation time lattice Boltzmann method. An interpolated bounce-back scheme was used to achieve high accuracy compared to the conventional staircase no-slip boundaries in LBM. The first part of this thesis focussed on the resulting mass leakage/gain issue due to the use of an interpolated bounce back scheme. Different boundary conditions were tested and accordingly different mass correction schemes were proposed through a systematic study. Subsequently, necessary recommendations were made regarding the mass correction schemes.

The second part of the work focussed on the flow around isolated axisymmetric non-spherical particles from the Stokes limit to relatively high Reynolds numbers (Re). Previous works were mainly limited to steady flows up to $Re = 300$. However in this work, we simulated even complex unsteady flows with Re upto 2000. Interesting scaling laws were observed during the process for the drag and lift of different axisymmetric non-spherical particles. We observed that the drag coefficient at any incident angle ϕ scaled as $C_{D,\phi} = C_{D,\phi=0°} + (C_{D,\phi=90°} - C_{D,\phi=0°})\sin^2\phi$. Similarly, we found that the lift coefficient at any incident angle ϕ scaled as $C_{L,\phi} = (C_{D,\phi=90°} - C_{D,\phi=0°})\sin\phi\cos\phi$. The reason for such scaling in high Re flows was found to be not due to the flow linearity, as in the creeping flows, but due to an interesting pattern of pressure distribution on particles. The pressure distribution contributing to the drag and lift shows a dependency on the surface normal's orientation with the incoming flow in a consistent pattern. Subsequently, drag, lift and torque correlations for different isolated non-spherical particles were proposed as a function of Re and ϕ. Known theoretical limits at low Re and different decay rates at high Re were considered while formulating these correlations. This implies that our correlations can be extended to regimes beyond our tested limits.

The later part of the work focussed on flow around assemblies of static, mono-disperse elongated particles. The performed simulations were from the Stokes flow regime to high Re with $Re \leq 1000$ at different solids volume fraction with $0 < \epsilon_s \leq 0.5$ and different mutual orientations of particles. The flow simulations indicated that the average forces and torques experienced by particles at a specific angle of inclination ϕ with the mean flow were configuration independent. This greatly simplified the parameter space to be explored to only 3 parameters namely Re, ϵ_s, and ϕ. Interestingly, the sine-squared scaling of drag and sine-cosine scaling of lift for isolated non-spherical particles (Sanjeevi & Padding, 2017) were found to apply to multiparticle systems also. In other words, given a Re and ϵ_s, the average drag and lift at an arbitrary ϕ can be

described with the knowledge of drag at $\phi = 0°$ and $\phi = 90°$ alone. With the identified the dependent parameters, the correlations for drag, lift and torque were accordingly proposed for a multiparticle configuration as a function of Re, ϵ_s and ϕ. During the process, we also have explored the validity of the conventional approach of combining isolated non-spherical particle drag with the voidage effects based on spheres.

Overall, this work provides interesting scaling laws and a recipe to parametrize the average drag, lift and torque experienced by non-spherical particles in a multiparticle environment. To the best of our knowledge, there exists no work which parametrizes the drag, lift and torque for non-spherical particles in a multiparticle environment. Generally, lift and torque are ignored in large scale Euler-Lagrangian simulations. The proposed accurate drag, lift and torque correlations enable future Euler-Lagrangian (CFD-DEM) simulations to be performed with more realistic physics.

6.2. OUTLOOK

6.2.1. FLOW HETEROGENEITIES

Even with the proposed accurate drag, lift and torque closures, there are few heterogeneities that prevent simulations in replicating experiments. One such important factor is the phenomenon of flow channelling that occurs in some fluidized beds before onset of fluidization. This often results in inaccurate prediction of the minimum fluidization velocity in Euler-Lagrangian simulations. In most cases, the simulations have a lower fluidization velocity due to inability to include the flow channelling phenomenon. It is not difficult to predict the net force exerted on particle assemblies with flow channels. However, the difficulty lies in understanding the mechanism to predict the onset of flow channelling. Without this knowledge, the flow channelling behaviour cannot be included in the Euler-Lagrangian simulations. Therefore, sufficient attention must be given to the understanding of onset of such channelling/heterogeneities.

6.2.2. MACHINE LEARNING

With recent advancements in machine learning, it can be used as a powerful tool for better understanding of flow physics. Moore *et al.* (2019) propose a hybrid model which combines both physics based and data-driven model for flow around static assemblies of spheres. With the proposed hybrid model, the dependencies of neighbouring particles on the particle drag, lift and torque are pre-

dicted with improved accuracy. In future, the hybrid model can be extended to non-spherical particles where drag, lift and torque of individual particles are not only dependent on the neighbour positions but also on their orientations. With this information, future CFD-DEM simulations can incorporate the physics of flow heterogeneities to a certain extent by knowing the position of particles in each fluid cell.

6.2.3. SHAPES, ASPECT RATIOS AND POLYDISPERSITY

In the present work, we have extensively focussed on monodisperse assemblies of non-spherical particles. However, practical applications involve particles with a wide range of shapes and aspect ratios. Great efforts have been undertaken to identify drag and lift scaling laws which can be widely applied to a wide range of particle shapes and aspect ratios. However, there are always some limitations where such scaling laws fail. Therefore in the future, sufficient attention should be given in two directions. One is to develop more shape independent scaling laws. Another is to test different shapes and create a database for different shapes of particles where a universal scaling law may not apply. Another area of attention is to also include polydispersity of non-spherical particles while creating the drag, lift and torque closures.

6.2.4. HEAT AND MASS TRANSFER WITH CHEMICAL REACTIONS

Apart from momentum transfer, practical fluidization problems, as in biomass which motivated our research, also often involve heat and mass transfer with chemical reactions. This implies the need for conjugate heat transfer studies to investigate the heat transfer coefficients (HTC) for particle assemblies. This can be used to create HTC and similarly mass transfer correlations, which are needed for coarse grained simulations. Similarly, a multiscale approach needs to be developed to study the reaction kinetics at a microscale and utilize the results for macro-scale simulations.

A

SCALING LAWS FOR DRAG AND LIFT ON A SINGLE AXISYMMETRIC PARTICLE IN STOKES FLOW

For a particle in Stokes regime, the force exerted by the fluid $\boldsymbol{F}_{f \to p}$ can be written as,

$$\boldsymbol{F}_{f \to p} = \overline{\overline{\Xi}} \cdot \boldsymbol{u} \tag{A.1}$$

where, $\overline{\overline{\Xi}}$ is the resistance tensor, symmetric due to linearity of Navier-Stokes equations for creeping flows (Happel & Brenner, 1983) and $\boldsymbol{u}$ is the incoming flow.
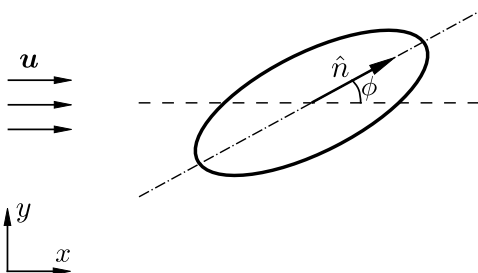

Figure A.1: An axisymmetric, non-spherical particle subjected to velocity $\boldsymbol{u}$ with orientation vector $\hat{n}$.

Given an axisymmetric particle, we define the orientation vector $\hat{n}$ which aligns with the axis of symmetry. Considering a particle with orientation vector $\hat{n}$, the resistance tensor $\overline{\overline{\Xi}}$ is

$$\overline{\overline{\Xi}} = \xi_\parallel (\hat{n} \otimes \hat{n}) + \xi_\perp (\mathbb{1} - \hat{n} \otimes \hat{n}) \tag{A.2}$$

where $\xi_\parallel$ and $\xi_\perp$ are the particle resistances for flow parallel and perpendicular to the axis of symmetry, respectively. Therefore

$$\boldsymbol{F}_{f \to p} = \xi_\parallel \hat{n}(\hat{n}.\boldsymbol{u}) + \xi_\perp (\boldsymbol{u} - \hat{n}(\hat{n}.\boldsymbol{u})). \tag{A.3}$$

Consider the non-spherical particle with orientation vector $\hat{n}$ making an angle ϕ (figure A.1) with respect to x-axis. Assuming the flow direction is parallel to x-axis, let $\hat{e}_x$ be the unit vector along x-axis and $\boldsymbol{u} = u\hat{e}_x$. The total force experienced by particle from equation A.3 can be written as,

$$\boldsymbol{F}_{f \to p} = \xi_\parallel \hat{n} u \cos\phi + \xi_\perp (u\hat{e}_x - \hat{n} u \cos\phi) \tag{A.4}$$

$$= \xi_\parallel \begin{bmatrix} \cos\phi \\ \sin\phi \end{bmatrix} u \cos\phi + \xi_\perp \left(u \begin{bmatrix} 1 \\ 0 \end{bmatrix} - \begin{bmatrix} \cos\phi \\ \sin\phi \end{bmatrix} u \cos\phi \right) \tag{A.5}$$

The drag force $\boldsymbol{F}_D$ can be given as,

$$\boldsymbol{F}_D = \boldsymbol{F}_{f \to p} \cdot \hat{e}_x \tag{A.6}$$

$$= \left(\xi_\parallel \cos^2\phi + \xi_\perp (1 - \cos^2\phi) \right) u \tag{A.7}$$

$$= \left(\xi_\parallel \cos^2\phi + \xi_\perp \sin^2\phi \right) u \tag{A.8}$$

$$= \left(\xi_\parallel + \left(\xi_\perp - \xi_\parallel \right) \sin^2\phi \right) u \tag{A.9}$$

The lift force $\boldsymbol{F}_L$ can be given by,

$$\boldsymbol{F}_L = \boldsymbol{F}_{f \to p} \cdot \hat{e}_y \tag{A.10}$$

$$= \xi_\parallel u \sin\phi \cos\phi - \xi_\perp u \sin\phi \cos\phi \tag{A.11}$$

$$= - \left(\xi_\perp - \xi_\parallel \right) u \sin\phi \cos\phi \tag{A.12}$$

The drag coefficient C_D for a particle at an incident angle ϕ based on equation A.9 can be given as,

$$C_{D,\phi} = C_{D,\phi=0°} + (C_{D,\phi=90°} - C_{D,\phi=0°}) \sin^2\phi \tag{A.13}$$

The lift coefficient C_L for a particle at an incident angle ϕ based on equation A.12 is,

$$C_{L,\phi} = -(C_{D,\phi=90°} - C_{D,\phi=0°}) \sin\phi \cos\phi \tag{A.14}$$

We assumed ϕ increases in counter-clockwise direction. For ϕ increasing in clockwise direction as in our simulation setup, equation A.14 becomes,

$$C_{L,\phi} = (C_{D,\phi=90°} - C_{D,\phi=0°}) \sin\phi \cos\phi. \tag{A.15}$$

B

THEORY OF LINEARITY

Ignoring the non-linear inertial term $\boldsymbol{u} \cdot \nabla \boldsymbol{u}$ arising at higher Re, the Stokes equations for creeping flow are

$$\nabla \cdot \boldsymbol{u} \quad = 0, \text{ and} \tag{B.1}$$

$$\mu \nabla^2 \boldsymbol{u} \quad = \nabla p. \tag{B.2}$$

For simplicity, we consider the flow to be two dimensional. The velocity field $\boldsymbol{u}_\phi$ and pressure field p_ϕ for an incoming flow with an arbitrary angle ϕ with respect to the particle can be written as a linear combination of the fields of $\phi = 0°$ and $\phi = 90°$ as

$$\boldsymbol{u}_\phi = a \cdot \boldsymbol{u}_{\phi=0°} + b \cdot \boldsymbol{u}_{\phi=90°} + \boldsymbol{c}, \tag{B.3}$$

$$p_\phi = d \cdot p_{\phi=0°} + e \cdot p_{\phi=90°} + f, \tag{B.4}$$

where, a, b, d, e, f are constants and $\boldsymbol{c}$ is the offset vector field. For a fixed particle as in our case, at the particle boundary, $\boldsymbol{u}_{\phi=0°} \to \boldsymbol{0}$, $\boldsymbol{u}_{\phi=90°} \to \boldsymbol{0}$, and $\boldsymbol{u}_\phi \to \boldsymbol{0}$. This
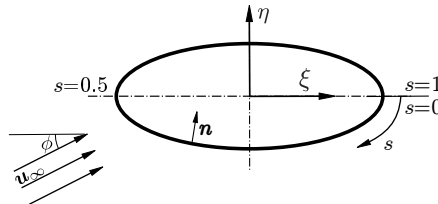

Figure B.1: Elliptical section with an incoming flow at an angle ϕ.

implies $c = 0$. Further, linearity means that the velocity $\boldsymbol{u}$ and pressure p scale proportionally such that equation B.2 is written as

$$\mu\nabla^2(a\cdot\boldsymbol{u}_{\phi=0°} + b\cdot\boldsymbol{u}_{\phi=90°}) = \nabla(a\cdot p_{\phi=0°} + b\cdot p_{\phi=90°}). \tag{B.5}$$

Therefore, the pressure linearity is inferred as

$$p_\phi = a\cdot p_{\phi=0°} + b\cdot p_{\phi=90°} + g, \tag{B.6}$$

with $\nabla g = \boldsymbol{0}$. Therefore from equations B.4 and B.6, $a = d$, $b = e$ and $f = g$.

At far field $|\boldsymbol{r}| \to \infty$, $\boldsymbol{u}_\phi = u_\infty(\cos\phi, \sin\phi)^T$, $\boldsymbol{u}_{\phi=0°} = u_\infty(1,0)^T$, and $\boldsymbol{u}_{\phi=90°} = u_\infty(0,1)^T$. Therefore, the coefficients of equation B.3 and B.4 are

$$a = d = \cos\phi, \text{ and} \tag{B.7}$$
$$b = e = \sin\phi. \tag{B.8}$$

At farfield $|\boldsymbol{r}| \to \infty$, $p_\phi = p_{\phi=0°} = p_{\phi=90°} = p_\infty$. From equation B.4,

$$p_\infty = p_\infty\cos\phi + p_\infty\sin\phi + f, \tag{B.9}$$

and therefore

$$f = p_\infty(1 - \cos\phi - \sin\phi). \tag{B.10}$$

Therefore because of flow linearity in the Stokes regime, the velocity field $\boldsymbol{u}$ and pressure p satisfy

$$\boldsymbol{u}_\phi \quad = \boldsymbol{u}_{\phi=0°}\cos\phi + \boldsymbol{u}_{\phi=90°}\sin\phi, \text{ and} \tag{B.11}$$
$$p_\phi - p_\infty \quad = (p_{\phi=0°} - p_\infty)\cos\phi + (p_{\phi=90°} - p_\infty)\sin\phi. \tag{B.12}$$

REFERENCES

AIDUN, C. K. & CLAUSEN, J. R. 2010 Lattice-Boltzmann method for complex flows. *Annu. Rev. Fluid Mech.* **42**, 439–472.

AIDUN, C. K., LU, Y., DING, E.-J. & OTHERS 1998 Direct analysis of particulate suspensions with inertia using the discrete Boltzmann equation. *J. Fluid Mech.* **373**, 287–311.

AKENINE-MÖLLER, T., HAINES, E. & HOFFMAN, N. 2008 *Real-time rendering*. CRC Press.

BAO, J., YUAN, P. & SCHAEFER, L. 2008 A mass conserving boundary condition for the lattice Boltzmann equation method. *J. Comput. Phys.* **227** (18), 8472–8487.

BEETSTRA, R., VAN DER HOEF, M. A. & KUIPERS, J. A. M. 2007 Drag force of intermediate Reynolds number flow past mono-and bidisperse arrays of spheres. *AIChE J.* **53** (2), 489–501.

BOUZIDI, M., FIRDAOUSS, M. & LALLEMAND, P. 2001 Momentum transfer of a Boltzmann-lattice fluid with boundaries. *Phys. Fluids* **13**, 3452–3459.

BROWN, P. P. & LAWLER, D. F. 2003 Sphere drag and settling velocity revisited. *J. Environ. Eng.* **129** (3), 222–231.

CHEN, H., TEIXEIRA, C. & MOLVIG, K. 1998 Realization of fluid boundary conditions via discrete Boltzmann dynamics. *Int. J. Mod. Phys. C* **9** (08), 1281–1292.

CHEN, S., MARTINEZ, D. & MEI, R. 1996 On boundary conditions in lattice Boltzmann methods. *Phys. Fluids* **8** (9), 2527–2536.

D'HUMIÈRES, D., GINZBURG, I., KRAFCZYK, M., LALLEMAND, P. & LUO, L.-S. 2002 Multiple–relaxation–time lattice Boltzmann models in three dimensions. *Phil. Trans. R. Soc. Lond. A* **360**, 437–451.

DI FELICE, R. 1994 The voidage function for fluid-particle interaction systems. *Int. J. Multiph. Flow* **20** (1), 153–159.

EITEL-AMOR, G., MEINKE, M. & SCHRÖDER, W. 2013 A lattice-Boltzmann method with hierarchically refined meshes. *Comput. Fluids* **75**, 127–139.

EL KHOURY, G. K., ANDERSSON, H. I. & PETTERSEN, B. 2010 Crossflow past a prolate spheroid at Reynolds number of 10000. *J. Fluid Mech.* **659**, 365–374.

EL KHOURY, G. K., ANDERSSON, H. I. & PETTERSEN, B. 2012 Wakes behind a prolate spheroid in crossflow. *J. Fluid Mech.* **701**, 98–136.

ERGUN, S. 1952 Fluid flow through packed columns. *Chem. Eng. Prog.* **48**, 89–94.

FENG, Z.-G. & MICHAELIDES, E. E. 2004 The immersed boundary-lattice Boltzmann method for solving fluid–particles interaction problems. *J. Comput. Phys.* **195** (2), 602–628.

FILIPPOVA, O. & HÄNEL, D. 1997 Lattice-Boltzmann simulation of gas-particle flow in filters. *Comput. Fluids* **26** (7), 697–712.

FILIPPOVA, O. & HÄNEL, D. 1998 Grid refinement for lattice-BGK models. *J. Comput. Phys.* **147** (1), 219–228.

GAN, J. Q., ZHOU, Z. Y. & YU, A. B. 2016 A GPU-based DEM approach for modelling of particulate systems. *Powder Technol.* **301**, 1172–1182.

GANSER, G. H. 1993 A rational approach to drag prediction of spherical and nonspherical particles. *Powder Technol.* **77** (2), 143–152.

GELDART, D. 1973 Types of gas fluidization. *Powder Technol.* **7** (5), 285–292.

GINZBURG, I. & D'HUMIÈRES, D. 2003 Multireflection boundary conditions for lattice Boltzmann models. *Phys. Rev. E* **68** (6), 066614.

GINZBURG, I., VERHAEGHE, F. & D'HUMIÈRES, D. 2008 Study of simple hydrodynamic solutions with the two-relaxation-times lattice Boltzmann scheme. *Commun. Comput. Phys.* **3** (3), 519–581.

GUO, Z., ZHENG, C. & SHI, B. 2002 An extrapolation method for boundary conditions in lattice Boltzmann method. *Phys. Fluids* **14** (6), 2007–2010.

HAIDER, A. & LEVENSPIEL, O. 1989 Drag coefficient and terminal velocity of spherical and nonspherical particles. *Powder Technol.* **58** (1), 63–70.

HAPPEL, J. & BRENNER, H. 1983 *Low Reynolds number hydrodynamics: with special applications to particulate media*, , vol. 1. Springer Science & Business Media.

HE, L. & TAFTI, D. 2018 Variation of drag, lift and torque in a suspension of ellipsoidal particles. *Powder Technol.* **335**, 409–426.

HE, X. & LUO, L.-S. 1997 Lattice Boltzmann model for the incompressible Navier–Stokes equation. *J. Stat. Phys.* **88** (3), 927–944.

HECHT, M. & HARTING, J. 2010 Implementation of on-site velocity boundary conditions for D3Q19 lattice Boltzmann simulations. *J. Stat. Mech. Theor. Exp.* **2010**, P01018.

HILL, R. J., KOCH, D. L. & LADD, A. J. C. 2001 Moderate-Reynolds-number flows in ordered and random arrays of spheres. *J. Fluid Mech.* **448**, 243–278.

HILTON, J. E., MASON, L. R. & CLEARY, P. W. 2010 Dynamics of gas–solid fluidised beds with non-spherical particle geometry. *Chem. Eng. Sci.* **65** (5), 1584–1596.

VAN DER HOEF, M. A., BEETSTRA, R. & KUIPERS, J. A. M. 2005 Lattice-Boltzmann simulations of low-Reynolds-number flow past mono-and bidisperse arrays of spheres: results for the permeability and drag force. *J. Fluid Mech.* **528**, 233–254.

HOLLOWAY, W., YIN, X. & SUNDARESAN, S. 2010 Fluid-particle drag in inertial polydisperse gas–solid suspensions. *AIChE J.* **56** (8), 1995–2004.

HÖLZER, A. & SOMMERFELD, M. 2008 New simple correlation formula for the drag coefficient of non-spherical particles. *Powder Technol.* **184** (3), 361–365.

HÖLZER, A. & SOMMERFELD, M. 2009 Lattice Boltzmann simulations to determine drag, lift and torque acting on non-spherical particles. *Comput. Fluids* **38**, 572–589.

HUANG, H., YANG, X., KRAFCZYK, M. & LU, X.-Y. 2012 Rotation of spheroidal particles in Couette flows. *J. Fluid Mech.* **692**, 369–394.

INAMURO, T., YOSHINO, M. & OGINO, F. 1995 A non-slip boundary condition for lattice Boltzmann simulations. *Phys. Fluids* **7** (12), 2928–2930.

JEFFERY, G. B. 1922 The motion of ellipsoidal particles immersed in a viscous fluid. In *Proceedings of the Royal Society of London A: Mathematical, Physical and Engineering Sciences*, , vol. 102, pp. 161–179. The Royal Society.

JIANG, F., GALLARDO, J. P. & ANDERSSON, H. I. 2014 The laminar wake behind a 6: 1 prolate spheroid at 45 incidence angle. *Phys. Fluids* **26** (11), 113602.

JIANG, F., GALLARDO, J. P., ANDERSSON, H. I. & ZHANG, Z. 2015 The transitional wake behind an inclined prolate spheroid. *Phys. Fluids* **27**, 093602.

KANDHAI, D., KOPONEN, A., HOEKSTRA, A., KATAJA, M., TIMONEN, J. & SLOOT, P. M. A. 1999 Implementation aspects of 3D lattice-BGK: boundaries, accuracy, and a new fast relaxation method. *J. Comput. Phys.* **150** (2), 482–501.

KAO, P.-H. & YANG, R.-J. 2008 An investigation into curved and moving boundary treatments in the lattice Boltzmann method. *J. Comput. Phys.* **227** (11), 5671–5690.

KRUGGEL-EMDEN, H., KRAVETS, B., SURYANARAYANA, M. K. & JASEVICIUS, R. 2016 Direct numerical simulation of coupled fluid flow and heat transfer for single particles and particle packings by a LBM-approach. *Powder Technol.* **294**, 236–251.

KUNII, D. & LEVENSPIEL, O. 2013 *Fluidization engineering*. Elsevier.

LADD, A. J. C. 1994*a* Numerical simulations of particulate suspensions via a discretized Boltzmann equation. Part 1. Theoretical foundation. *J. Fluid Mech.* **271** (1), 285–309.

LADD, A. J. C. 1994*b* Numerical simulations of particulate suspensions via a discretized Boltzmann equation. Part 2. Numerical results. *J. Fluid Mech.* **271**, 311–339.

LADD, A. J. C. & VERBERG, R. 2001 Lattice-Boltzmann simulations of particle-fluid suspensions. *J. Stat. Phys.* **104** (5-6), 1191–1251.

LALLEMAND, P. & LUO, L.-S. 2003 Lattice Boltzmann method for moving boundaries. *J. Comput. Phys.* **184** (2), 406–421.

LATT, J., CHOPARD, B., MALASPINAS, O., DEVILLE, M. & MICHLER, A. 2008 Straight velocity boundaries in the lattice Boltzmann method. *Phys. Rev. E* **77** (5), 056703.

LE COUPANEC, E. & VERSCHAEVE, J. C. G. 2011 A mass conserving boundary condition for the lattice Boltzmann method for tangentially moving walls. *Math. Comput. Simul.* **81** (12), 2632–2645.

LEITH, D. 1987 Drag on nonspherical objects. *Aerosol Sci. Technol.* **6** (2), 153–161.

LUO, L.-S. 1993 Lattice-gas automata and lattice Boltzmann equations for two-dimensional hydrodynamics. PhD thesis, Georgia Institute of Technology.

MAHAJAN, V. V., PADDING, J. T., NIJSSEN, T. M. J., BUIST, K. A. & KUIPERS, J. A. M. 2018 Nonspherical particles in a pseudo-2D fluidized bed: Experimental study. *AIChE J.* **64** (5), 1573–1590.

MAIER, W. & SAUPE, A. 1959 Eine einfache molekular-statistische Theorie der nematischen kristallinflüssigen Phase. Teil 1. *Z. Naturforsch. A* **14** (10), 882–889.

MEI, R., LUO, L.-S. & SHYY, W. 1999 An accurate curved boundary treatment in the lattice Boltzmann method. *J. Comput. Phys.* **155** (2), 307–330.

MEI, R., YU, D., SHYY, W. & LUO, L.-S. 2002 Force evaluation in the lattice Boltzmann method involving curved geometry. *Phys. Rev. E* **65** (4), 041203.

MOORE, W. C., BALACHANDAR, S. & AKIKI, G. 2019 A hybrid point-particle force model that combines physical and data-driven approaches. *J. Comput. Phys.* **385**, 187–208.

NASH, R. W., CARVER, H. B., BERNABEU, M. O., HETHERINGTON, J., GROEN, D., KRÜGER, T. & COVENEY, P. V. 2014 Choice of boundary condition for lattice-Boltzmann simulation of moderate-Reynolds-number flow in complex domains. *Phys. Rev. E* **89** (2), 023303.

NOBLE, D. R., CHEN, S., GEORGIADIS, J. G. & BUCKIUS, R. O. 1995 A consistent hydrodynamic boundary condition for the lattice Boltzmann method. *Phys. Fluids* **7** (1), 203–209.

OBERBECK, A. 1876 Über stationäre Flüssigkeitsbewegungen mit Berücksichtigung der inneren Reibung. *J. Reine Angew. Math.* **81**, 62–80.

OSCHMANN, T., HOLD, J. & KRUGGEL-EMDEN, H. 2014 Numerical investigation of mixing and orientation of non-spherical particles in a model type fluidized bed. *Powder Technol.* **258**, 304–323.

OUCHENE, R., KHALIJ, M., ARCEN, B. & TANIÈRE, A. 2016 A new set of correlations of drag, lift and torque coefficients for non-spherical particles and large Reynolds numbers. *Powder Technol.* **303**, 33–43.

OUCHENE, R., KHALIJ, M., TANIÈRE, A. & ARCEN, B. 2015 Drag, lift and torque coefficients for ellipsoidal particles: From low to moderate particle reynolds numbers. *Comput. Fluids* **113**, 53–64.

PAN, C., LUO, L.-S. & MILLER, C. T. 2006 An evaluation of lattice Boltzmann schemes for porous medium flow simulation. *Comput. Fluids* **35**, 898–909.

PLOUMHANS, P., WINCKELMANS, G. S., SALMON, J. K., LEONARD, A. & WARREN, M. S. 2002 Vortex methods for direct numerical simulation of three-dimensional bluff body flows: application to the sphere at Re= 300, 500, and 1000. *J. Comput. Phys.* **178**, 427–463.

POURNIN, L., WEBER, M., TSUKAHARA, M., FERREZ, J.-A., RAMAIOLI, M. & LIEBLING, T. M. 2005 Three-dimensional distinct element simulation of sphe-rocylinder crystallization. *Granul. Matter* **7** (2-3), 119–126.

POWELL, M. J. D. 1964 An efficient method for finding the minimum of a func-tion of several variables without calculating derivatives. *Comput. J.* **7** (2), 155–162.

RICHARDSON, J. F. & ZAKI, W. N. 1954 Sedimentation and fluidization: Part 1. *Trans. Inst. Chem. Eng* **32**, 35–53.

RICHTER, A. & NIKRITYUK, P. A. 2012 Drag forces and heat transfer coefficients for spherical, cuboidal and ellipsoidal particles in cross flow at sub-critical Reynolds numbers. *Int. J. Heat Mass Transf.* **55** (4), 1343–1354.

RICHTER, A. & NIKRITYUK, P. A. 2013 New correlations for heat and fluid flow past ellipsoidal and cubic particles at different angles of attack. *Powder Tech-nol.* **249**, 463–474.

ROHDE, M., DERKSEN, J. J. & VAN DEN AKKER, H. E. A. 2002 Volumetric method for calculating the flow around moving objects in lattice-Boltzmann schemes. *Phys. Rev. E* **65** (5), 056701.

RUBINSTEIN, G. J., OZEL, A., YIN, X., DERKSEN, J. J. & SUNDARESAN, S. 2017 Lattice Boltzmann simulations of low-Reynolds-number flows past fluidized spheres: effect of inhomogeneities on the drag force. *J. Fluid Mech.* **833**, 599–630.

SANJEEVI, S. K. P., KUIPERS, J. A. M. & PADDING, J. T. 2018*a* Drag, lift and torque correlations for non-spherical particles from Stokes limit to high Reynolds numbers. *Int. J. Multiph. Flow* **106**, 325–337.

SANJEEVI, S. K. P. & PADDING, J. T. 2017 On the orientational dependence of drag experienced by spheroids. *J. Fluid Mech.* **820**, R1.

SANJEEVI, S. K. P., ZARGHAMI, A. & PADDING, J. T. 2018*b* Choice of no-slip curved boundary condition for lattice Boltzmann simulations of high-Reynolds-number flows. *Phys. Rev. E* **97** (4), 043305.

SCHILLER, L. & NAUMANN, A. 1935 A drag coefficient correlation. *Z. Ver. Deutsch. Ing* **77**, 318–320.

SKORDOS, P. A. 1993 Initial and boundary conditions for the lattice Boltzmann method. *Phys. Rev. E* **48** (6), 4823.

SUCCI, S. 2001 *The lattice Boltzmann equation: for fluid dynamics and beyond.* Oxford university press.

SUKOP, M. C. & THORNE, D. T. 2006 *Lattice Boltzmann Modeling: An Introduction for Geoscientists and Engineers.* Springer.

SUZUKI, K. & INAMURO, T. 2011 Effect of internal mass in the simulation of a moving body by the immersed boundary method. *Comput. Fluids* **49** (1), 173–187.

TANG, Y., PETERS, E. A. J. F., KUIPERS, J. A. M., KRIEBITZSCH, S. H. L. & VAN DER HOEF, M. A. 2015 A new drag correlation from fully resolved simulations of flow past monodisperse static arrays of spheres. *AIChE J.* **61** (2), 688–698.

TENNETI, S., GARG, R. & SUBRAMANIAM, S. 2011 Drag law for monodisperse gas–solid systems using particle-resolved direct numerical simulation of flow past fixed assemblies of spheres. *Int. J. Multiph. Flow* **37** (9), 1072–1092.

TIWARI, A. & VANKA, S. P. 2012 A ghost fluid Lattice Boltzmann method for complex geometries. *Int. J. Numer. Methods Fluids* **69** (2), 481–498.

VAKARELSKI, I. U., BERRY, J. D., CHAN, D. Y. C. & THORODDSEN, S. T. 2016 Leidenfrost vapor layers reduce drag without the crisis in high viscosity liquids. *Phys. Rev. Lett.* **117**, 114503.

VEGA, C. & LAGO, S. 1994 A fast algorithm to evaluate the shortest distance between rods. *Comput. Chem. (Oxford)* **18** (1), 55–59.

WILLIAMS, S. R. & PHILIPSE, A. P. 2003 Random packings of spheres and spherocylinders simulated by mechanical contraction. *Phys. Rev. E* **67** (5), 051301.

WOLF-GLADROW, D. A. 2004 *Lattice-gas cellular automata and lattice Boltzmann models: an introduction.* Springer.

YIN, X., LE, G. & ZHANG, J. 2012 Mass and momentum transfer across solid-fluid boundaries in the lattice-Boltzmann method. *Phys. Rev. E* **86** (2), 026701.

YIN, X. & ZHANG, J. 2012 An improved bounce-back scheme for complex boundary conditions in lattice Boltzmann method. *J. Comput. Phys.* **231** (11), 4295–4303.

YU, D., MEI, R., LUO, L.-S. & SHYY, W. 2003*a* Viscous flow computations with the method of lattice Boltzmann equation. *Prog. Aerosp. Sci.* **39** (5), 329–367.

YU, D., MEI, R. & SHYY, W. 2003*b* A unified boundary treatment in lattice boltzmann method. In *41st Aerospace Sciences Meeting and Exhibit*, p. 953.

ZARGHAMI, A., FALCUCCI, G., JANNELLI, E., SUCCI, S., PORFIRI, M. & UBERTINI, S. 2014 Lattice Boltzmann modeling of water entry problems. *Int. J. Mod. Phys. C* **25** (12), 1441012.

ZARGHAMI, A., LOOIJE, N. & VAN DEN AKKER, H. 2015 Assessment of interaction potential in simulating nonisothermal multiphase systems by means of lattice Boltzmann modeling. *Phys. Rev. E* **92** (2), 023307.

ZASTAWNY, M., MALLOUPPAS, G., ZHAO, F. & VAN WACHEM, B. 2012 Derivation of drag and lift force and torque coefficients for non-spherical particles in flows. *Int. J. Multiph. Flow* **39**, 227–239.

ZIEGLER, D. P. 1993 Boundary conditions for lattice Boltzmann simulations. *J. Stat. Phys.* **71** (5-6), 1171–1177.

ZOU, Q. & HE, X. 1997 On pressure and velocity boundary conditions for the lattice Boltzmann BGK model. *Phys. Fluids* **9** (6), 1591–1598.

List of Publications

Journal publications

1. Sanjeevi S. K. P. & Padding J. T. (2017). "On the orientational dependence of drag experienced by spheroids". *J. Fluid Mech.* **820**, R1.

2. Sanjeevi S. K. P., Zarghami A. & Padding J. T. (2018). "Choice of no-slip curved boundary condition for lattice Boltzmann simulations of high Reynolds number flows". *Phys. Rev. E* **97**, 043305.

3. Sanjeevi S. K. P., Kuipers J. A. M. & Padding J. T. (2018). "Drag, lift and torque correlations for non-spherical particles from Stokes limit to high Reynolds numbers". *Int. J. Multiph. Flow* **106**, 325-337.

4. Sanjeevi S. K. P. & Padding J. T. "Hydrodynamic forces on assemblies of non-spherical particles: orientation and voidage effects". *Submitted to AIChE J. (2019).*

5. Vila A., Sanjeevi S. K. P., Padding J. T. & Pirker S. (2019). "Gas flow through static particle arrangements with a channel: Resolved simulations and analytic considerations". *Chem. Eng. Sci. X* **2**, 100015.

6. Fitzgerald B. W., Zarghami A., Mahajan V. V., Sanjeevi S. K. P., Mema I., Verma V., El Hasadi Y. M. F. & Padding J. T. (2019). "Multiscale simulation of elongated particles in fluidised beds". *Chem. Eng. Sci. X* **2**, 100019.

Conference publications and presentations

1. Sanjeevi S. K. P., Padding J. T. & Kuipers J. A. M. "Direct numerical simulations of fluid drag forces of non-spherical particle". CFD2015, Melbourne, Australia, 2015.

2. Sanjeevi S. K. P., Padding J. T. & Kuipers J. A. M. "Direct numerical simulations of flow around a non-spherical particle", ICMF 2016, Florence, Italy, 2016.

3. Sanjeevi S. K. P. & Padding J. T. "The dependence of the drag and lift of non-spherical particles", CFD2017, Trondheim, Norway, 2017.

4. Sanjeevi S. K. P., Zarghami A. & Padding J. T. "Choice of no-slip curved boundary condition for lattice Boltzmann simulation of high Reynolds flows". ICMMES 2017, Nantes, France, 2017.

5. Sanjeevi S. K. P. & Padding J. T. "Sine-Squared Scaling of Drag Coefficient for Different Non-Spherical Particles", 2017 American Institute of Chemical Engineers (AIChE) Annual Meeting, Minneapolis, USA, 2017.

6. Sanjeevi S. K. P. & Padding J. T. "The drag and lift of different non-spherical particles from low to high *Re*", 70th Annual Meeting of the American Physical Society Division of Fluid Dynamics (APS DFD), Denver, USA, 2017.

7. Sanjeevi S. K. P. & Padding J. T. "Direct numerical simulations of flow around assemblies of non-spherical particles and the investigation of voidage effects", 2018 American Institute of Chemical Engineers (AIChE) Annual Meeting, Pittsburgh, USA, 2018.

ACKNOWLEDGEMENTS

The last four years has been a exciting journey and I would like to thank here my colleagues, friends and family for supporting my journey. First, I would like to thank Prof. Johan Padding and Prof. Hans Kuipers for giving me the opportunity to pursue this doctoral research. Especially, Hans has been very supportive and motivating during the progress meetings, despite his busy schedule. His guidance has been valuable and also has taught me the importance of presenting research output in a time-bound fashion.

Johan has been a ideal supervisor that any doctoral student would wish for. His belief of providing a high degree of research freedom during the PhD study is very much appreciated, considering the time limits of the doctoral program. In fact, this freedom has resulted in a nice publication in JFM. His attention to details, enthusiasm, promptness in responding, open-door policy for discussions are highly appreciated. I am truly amazed by his by smartness and thank you for pointing out many times that things are not as obvious as they may appear.

I am also very thankful to Wim-Paul, who has kindly accepted to act as my second promotor despite the late stage of my PhD. I take this opportunity to thank Wim-Paul for graciously going through my thesis and providing valuable suggestions.

While in Eindhoven, I had the privilege to have great colleagues and friends. I very much enjoyed the witty conversations in the coffee and lunch breaks. I would like to thank Rohit, Vinay, Hong, Aditya, Aniruddha, Harshil, Hitesh, Monali, Alessandro, Ramon, Luuk, Maxim, Milan, Adnan, Satish, Saurish, Shauvik, Solomon, and Vishak for their help and support. Thanks also to my officemates of STW 0.49 for interesting discussions and help. I would like to thank Deepak, Krushna, Martin, Sushil and Yali in this regard. My sincere thanks to the group secretaries, Ada and Judith, for their help in administrative issues. I also would like to thank Prof. Jens Harting and his group for the lb3d code. Special mention to Qingguang for his patience and help in the beginning days of working with the code. The grants for funds from the ERC, compute time from NWO and also the technical support from SURFSARA are highly acknowledged.

During the second-half of my PhD in Delft, I had the privilege of having great people around me, both in the office and outside. I would like to thank Vikrant, Ivan, Youssef, Rumen, Simone, Ahad, Stephan, Rong and Barry. I very much enjoyed having our lunch together and also the yearly group outings. Leslie and

CURRICULUM VITÆ

Sathish Krishnan PACHA SANJEEVI

Sathish K. P. Sanjeevi was born in Arakkonam, India on 1st November 1988. After finishing his schooling in Thiruvallur, he enrolled for bachelors in Mechanical Engineering at Amrita University, Coimbatore. He completed his four year undergraduate program in 2009 and was awarded Bachelor of Technology in Mechanical Engineering with first class with distinction. After graduation, he worked for two years in India's leading engineering company, Larsen & Toubro. There he worked on the design and construction of supercritical thermal power plants. During the process, he also spent a year on site at Krishnapatnam, supervising the construction process of a supercritical thermal power plant.

In 2011, Sathish decided to enhance his knowledge on computational engineering and enrolled for masters in Simulation Sciences at RWTH Aachen University, Germany. During the masters, Sathish worked also as student assistant, assisting the doctoral students with programming and simulations in various departments. His master thesis was titled *A novel adaptive mesh refinement strategy on hierarchical Cartesian grids for lattice Boltzmann and finite volume solvers*, and was carried out in the Chair of Fluid Mechanics and Institute of Aerodynamics Aachen, known for its history in fluid dynamics.

In 2014, Sathish began his doctoral research under Prof. Hans Kuipers and Prof. Johan Padding at Eindhoven University of Technology, the Netherlands. After the initial two years, he moved to Delft University of Technology as his doctoral supervisor Prof. Johan Padding accepted a new position there. During his doctoral research, Sathish studied the detailed flow around isolated and assemblies of non-spherical particles. He presented his results at several international conferences and published articles in various reputed journals. The results of his research are presented in this thesis. After his doctoral research, he started working as a researcher at National Energy Technology Laboratory, USA.